STELLAR VARIABILITY NEAR THE GALACTIC MID-PLANE

A THESIS

SUBMITTED TO THE GRADUATE SCHOOL

IN PARTIAL FULFILLMENT OF THE REQUIREMENTS

FOR THE DEGREE

MASTER OF SCIENCE

BY

DYLAN E. GRIFFITH

DR. GUILLERMO GONZALEZ – ADVISOR

BALL STATE UNIVERSITY

MUNCIE, INDIANA

DECEMBER 2017

TABLE OF CONTENTS

ABSTRACT i
LIST OF FIGURES ii
LIST OF TABLES..... iv

1. Introduction

1.1 Background 1

1.2 Radial Metallicity Gradient 1

1.3 Stellar Metallicity and Planet Incidence 2

1.4 Interstellar Extinction 3

1.5 M-dwarf Stars 5

1.6 Transit Detection Method 5

1.7 Galactic Plane Studies and Similar Research 7

1.8 Differential Photometry 8

2. Data Acquisition

2.1 Introduction 9

2.2 Observations 16

3. Data Reduction

3.1 IRAF Setup and Installation 20

3.2 Bias Correction 21

3.3 Dark Correction 23

3.4 Flat Correction 25

3.5 Running ccdproc 27

4. VaST

4.1 Setup and Installation 29

4.2 PSF Photometry 29

4.3 Input 30

4.4 Output 31

5. UPSILON

5.1 Installation of UPSILON 36

5.2 Variable Star Results from UPSILON 38

6. VARTOOLS

6.1 Setup and Installation 44

6.2 Usage 44

6.3 Extra Solar Planet Results 45

7. Results 56

8. Conclusion 59

References 60

Appendix A 63

Appendix B 65

Appendix C 66

Appendix D 67

Appendix E 68

Appendix F 69

Appendix G 70

Appendix H.....71

Appendix I..... 73

ABSTRACT

THESIS: Stellar Variability Near the Galactic Mid-Plane

STUDENT: Dylan E. Griffith

DEGREE: Master of Science

COLLEGE: Science and Humanities

DATE: December 2017

PAGES: 99

Using Ball State University's on-campus 20-inch telescope and a differential photometric data pipeline, we have observed two fields near the galactic mid-plane. We have collected photometric data in the near-infrared over the course of two years to look for variability. In the process we have discovered new variable stars as well as exoplanet candidates via the photometric transit method.

LIST OF FIGURES

Figure 1-1 Stellar metallicity, expressed in "dex" or decimal exponent, is plotted versus galactocentric radius, expressed in kiloparsec (Frinchaboy et al., 2013). 2

Figure 1-2 Histogram of the percentage of stars with planets according to stellar metallicity. A bin size of 0.1 dex is used (Gonzalez, 2014). 3

Figure 1-3 The effect of interstellar extinction is notably lessened at wavelengths close to the near infrared (Li 2006). 4

Figure 2-1 The northern field has RA, DEC coordinates of 22^h 14^m 24^s and +56° 21' 49.5", respectively..... 10

Figure 2-2 The southern field has RA, DEC coordinates of 19^h 26^m 40^s and +27° 11' 15". 11

Figure 2-3 The Parallax 20-inch F/8 telescope was used for data acquisition. It is located on the rooftop of the Cooper Science building on the campus of Ball State University. 12

Figure 2-4 The FLI 16 MPixel CCD camera attached to the telescope. 13

Figure 3-1 A master bias image was created using **zerocombine**. 23

Figure 3-2 A master dark image was created using **darkcombine**. 24

Figure 3-3 Background stars can be observed in a single flat image. 26

Figure 3-4 Background stars are no longer visible in the median combined master flat. 26

Figure 3-5 A side by side comparison of a raw image (a) and a completely reduced image (b) shows the effectiveness of the reduction process. 28

Figure 4-1 Standard Deviation versus Instrumental Magnitude (southern field). 33

Figure 4-2 GUI of an individual variable star candidate obtained through VaST interface. 33

Figure 4-3 GUI of a star with pixel coordinates obtained by clicking on a single data point of a light curve. 34

Figure 4-4 Stetson's L Index versus Instrumental Magnitude. 34

Figure 4-5 Weighted Standard Deviation versus Instrumental Magnitude. 35

Figure 5-1 Histogram made to determine the best statistical cutoff (shown in red) for analysis of variability 37

Figure 5-2 Graph of three nights of observations for a Delta Scuti candidate in the southern field. 39

Figure 5-3 Folded light curve of a Delta Scuti candidate from the southen field. 40

Figure 5-4 Display of four nights of observations for a RR Lyrae candidate. 41

Figure 5-5 Folded light curve of a RR Lyrae candidate from the northern field. 41

Figure 6-1 Southern potential exoplanet candidate with 4 transits..... 46

Figure 6-2 Southern potential exoplanet candidate with 4 transits. 47

Figure 6-3 Southern potential exoplanet candidate with 3 transits. 48

Figure 6-4 Northern exoplanet candidate with 4 transits. 49

Figure 6-5 Northern exoplanet candidate with 3 transits. 50

Figure 6-6 Northern exoplanet candidate with 2 transits. 51

Figure 6-7 Northern exoplanet candidate with 2 transits. 52

Figure 6-8 Northern exoplanet candidate with 2 transits. 53

LIST OF TABLES

Table 2-1 Lunar phase during all observation dates. 15

Table 2-2 Statistical measurements were obtained to calculate telescope gain and saturation. 19

Table 5-1 Statistical Analysis of the Delta Scuti candidate from the southern field. 40

Table 5-2 Statistical Analysis of the RR Lyrae candidate from the northern field. 42

Table 5-3 All statistically significant variable star categorizations from UPSILON. 43

Table 6-1 All statistically significant BLS categorizations from VARTOOLS. 54

Table 6-2 Statistically significant exoplanet candidates from VARTOOLS. 55

Chapter 1

Introduction

1.1 Background

The purpose of this project is to implement a data acquisition and analysis pipeline, originally designed by Joseph Kindt in his master's thesis, in order to study potential extra solar planet incidence near the galactic midplane. Using the Ball State Observatory Parallax 20-inch rooftop telescope, many nights of data were obtained over the course of two years. The data were then processed with specialized reduction and analysis software. By observing two different fields at different galactocentric distances, this project initially set out to provide experimental results supporting a connection between two other correlations. This connection between the radial metallicity gradient of the Milky Way Galaxy and the relationship between metallicity and exoplanet incidence will be explained in further detail.

1.2 Radial Metallicity Gradient

In the Milky Way Galaxy, the metallicity of stars decreases as a function of the galactocentric radius (Kindt 2015). The metallicity of a star is defined as the ratio of percentage of non-hydrogen and non-helium abundance to hydrogen abundance. This is often expressed as a logarithm of the ratio of iron to hydrogen abundance [Fe/H]. The galactocentric radius is simply defined as the distance to an object from the center of the Milky Way Galaxy (expressed as kiloparsecs – kpc). Several studies have shown the trend that as the galactocentric distance increases, the metallicity decreases at a rate between -0.01 to -0.09 dex/kpc (Cheng et al. 2012). Another study by Frinchaboy et al. (2013) supports this relation, stating a fit of -0.09 dex/kpc for a data set of approximately 25 Classical Cepheid stars. Figure 1-1 shows this relationship.

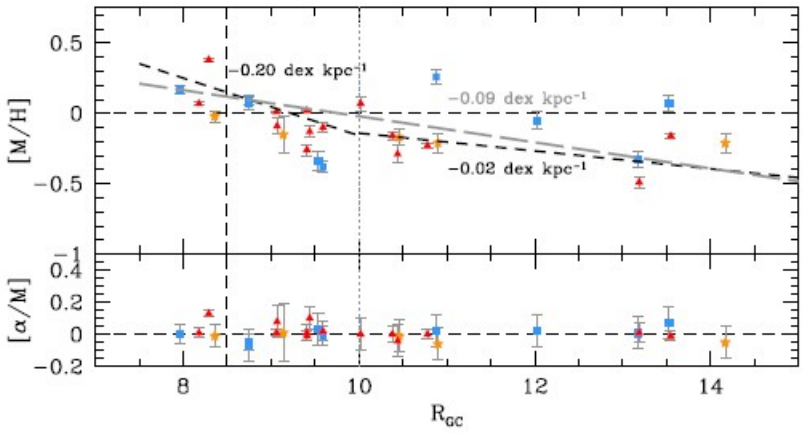

Figure 1-1 Stellar metallicity, expressed in "dex" or decimal exponent, is plotted versus galactocentric radius, expressed in kiloparsecs (Frinchaboy et al., 2013).

1.3 Stellar Metallicity and Planet Incidence

The probability of detecting an exoplanet correlates with the metallicity of a star (Kindt 2015). The higher the metallicity of the star, the more likely it hosts a giant planet. This makes detections of exoplanets via the transit method more probable. The correlation was originally proposed by Gonzalez (1997). Fischer and Valenti (2005) then modeled the relationship. Gonzalez (2014) then constrained the model by fitting the function from Fischer and Valenti (2005) to a plot of the fraction of stars with planets versus [Ref]. This can be seen in Figure 1-2, which uses the "refractory" index, [Ref], which compares iron, magnesium, and silicon abundances to hydrogen abundance.

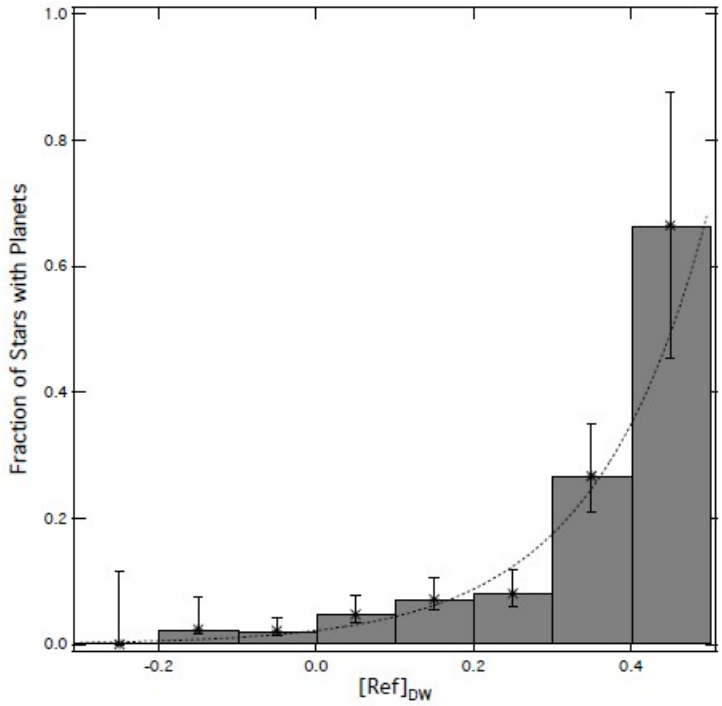

Figure 1-2 Histogram of the percentage of stars with planets according to stellar metallicity. A bin size of 0.1 dex is used (Gonzalez, 2014).

Due to these two trends, a relationship between exoplanet incidence and galactocentric radius should be observable. Since the average metallicity of stars is higher closer to the galactic center and higher metallicity stars are more likely to have easily observable exoplanets, more exoplanets should be observable at smaller galactocentric distances compared to larger galactocentric distances.

1.4 Interstellar Extinction

The absorption and scattering of photons by gas and dust in interstellar space is referred to as interstellar extinction. This phenomenon is most pronounced along the galactic midplane, where stars and dust are more densely concentrated. The scattering strength depends on

wavelength. Short wavelengths are the most strongly affected. Figure 1-3 shows the wavelength dependent extinction, which is normalized by the extinction in the "V" band. The inverse of wavelength is plotted on the bottom axis; therefore the left side of the figure corresponds to longer wavelengths. The near-infrared wavelengths near 9000 Å are the least distorted wavelengths that are still easily detectable with CCDs from the ground. For this reason, it is easier to detect exoplanets around stars that have a peak wavelength in the near-infrared.

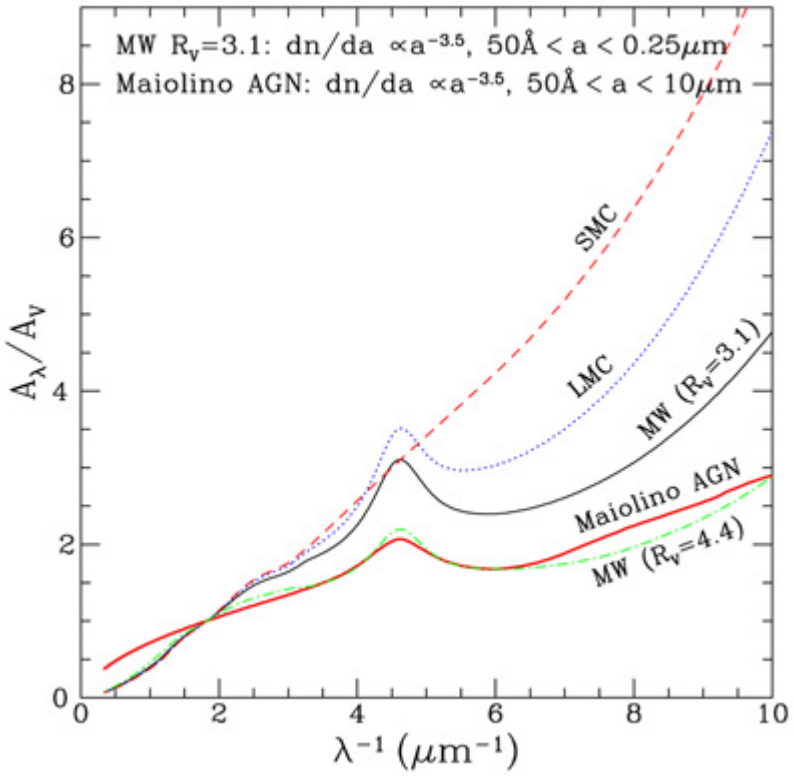

Figure 1-3 The effect of interstellar extinction is notably lessened at wavelengths close to the near infrared (Li 2006).

1.5 M-dwarf Stars

M-dwarf stars are small stars that have cool surface temperatures and are on the main sequence. Due to their low surface temperatures, their typical peak wavelength, according to Wien's Law, is located in the near-infrared. This will allow observation of these types of stars near the galactic midplane to be more practical. These stars also have some of the smaller radii compared to the rest of the stars on the HR diagram. Due to the star's smaller radius, an exoplanet transiting the star will have a more noticeable change in the apparent brightness, proportional to the squared radius of the exoplanet.

1.6 Transit Detection Method

An exoplanet is most easily detected by observing the brightness of an individual star over an extended period and searching for periodic eclipses. The signature signal from a transit is a shallow square-shaped drop in brightness. This is due to the exoplanet passing between the star and the observer on the earth. The small radius of the exoplanet means that it only blocks a small amount of the observable light from the star, but it takes a few hours to cross the star. The apparent brightness of the star is approximately constant during the duration of the transit, only returning to the unobstructed apparent brightness once the exoplanet has passed the edge of the star. The small radius of the planet and almost unchanging apparent brightness during transit makes the light curve signal a very distinct and easily recognizable boxed shape.

Unfortunately, there are a few phenomena that have similar or identical light curves to exoplanet transits; one of these being the existence of starspots. These portions of cooled solar exterior matter are opaque and mostly stationary on the surface of the star. Therefore, the period of these light curves due to starspots are exactly the same as the star's rotational period, which is

significantly longer than the orbital period of an exoplanet that we would be able to detect. The duration of the time the starspot is visible on the surface of the star is significantly longer than the duration of an exoplanet transit. A starspot could be easily discerned from an exoplanet candidate by comparing the transit duration of the signal to the usual transit duration of an exoplanet.

Another potential false exoplanet signal could be an eclipsing binary with a brown dwarf star. This is theoretically easy to distinguish, as most transit depths for exoplanets are less than a 0.05 magnitude difference. Any transit depth larger than this would indicate a transiting object that would be larger than an exoplanet. This could potentially be a brown dwarf. The best way to confirm this would be to gather spectroscopic data and determine the mass of the companion.

Bad columns of pixels on the CCD detector have also been observed to have light curve characteristics similar to that of exoplanets and small eclipsing binary signals (R. Kaichuck, personal communication, September 5, 2017). The existence of a column of bad pixels can distort the light from a star as it crosses the bad column, due to imperfect telescope tracking. This is able to be ameliorated by creating a bad pixel mask in the data reduction process, which is explained in more depth in Chapter 3.

The most commonly observed false positives for exoplanet transits are blended eclipsing binary stars. If a bright single star is optically close to a dimmer eclipsing binary star, the resultant light curve will appear similar to an exoplanet transit. In order to confirm that an exoplanet candidate is not a blended eclipsing binary, observations higher signal-to-noise ratio could be used to look for secondary eclipses (Cameron, A. 2016).

1.7 Galactic Plane Studies and Similar Research

Previous to this study, there were multiple large-scale surveys operating to detect exoplanets, with two prominent ones being SUperWASP and Kepler K2. Neither of these two surveys include regions near the Galactic mid-plane. This is due to large crowding in the fields (Kindt 2015).

Another survey recently started early in 2017, which is the All-Sky Automated Survey for Supernovae (ASAS-SN). The survey images the entire sky once every night to a depth of V~17 mag. The ASAS_SN survey could potentially find long period exoplanets, but will be unable to detect exoplanets with short periods effectively. The survey also uses only aperture photometry, and therefore observations near the galactic mid-plane will have significantly more error due to crowding (Kochanek et al. 2017).

There are several other smaller scale surveys observing stellar variability, but few of them are focusing on exoplanets. One of these that searches for exoplanets near the galactic mid-plane is the Kourovka Planet Search (KPS), located at the observatory at the Ural Federal University in Russia. One distinction between our project and the KPS survey is the exposure time. All of the data collected by the KPS survey have exposure times of fifty seconds while our project has one hundred and eighty second exposure times, which should allow the detection of variability for fainter stars. Through three years of observations, from 2012 to 2015, the Russian group was able to identify four exoplanet candidates. The group has published that it is most probable that three of the four candidates are astrophysical false positives, mainly blended eclipsing binaries (Burandov 2016).

1.8 Differential Photometry

Differential photometry employs the technique of comparing the brightness of a target star with one or more comparison stars. For each image in a data series, an average brightness of multiple comparison stars is compared to the brightness of the target star. The resultant relative brightness is a differential measure. This can be plotted against time and analyzed for variability. In this project, Point-Spread Function (PSF) fitting photometry was implemented, which will be explained in more detail in Chapter 4. The software used in this project employs an analytic PSF modeled by an ellipsoidal Gaussian function that accurately fits the profile of a star (Sokolovsky, K. & Lebedev A. 2017). The star profile is a three-dimensional model of the counts of photons per pixel across the two pixel dimensions of a star.

Differential photometry is very useful for surveys due to the possibility to process objects quickly and simply, and it is insensitive to atmospheric transparency variations. This allows very large data sets to be processed in an automated way.

Chapter 2

Data Acquisition

2.1 Introduction

For this study, two different star fields were observed, both near the galactic mid-plane but containing stars at different galactocentric distances. The northern field has right ascension (RA) and declination (DEC) epoch 2000.0 coordinates of 22^h 14^m 24^s and +56° 21' 49.5" and galactic coordinates (*l*, *b*) of 102.4117° and -0.1186°, respectively. This field is within the Cepheus constellation and has approximately 50,000 individual stars observable in the near infrared. The southern field has RA and DEC coordinates of 19^h 26^m 40^s and +27° 11' 15" and galactic coordinates *l, b* of 61.0007° and 4.9985° (Duffett-Smith 1992). This field is located on the edge of the Vulpecula and Cygnus constellations and contains more stars (at a smaller average galactocentric distance, Roman 1987). The number of detectable stars in the near infrared is also higher, estimated at around 70,000 stars. Figure 2-1 and 2-2 are reduced images of the northern and southern fields respectively. The size of each field is thirty arc-minutes and the on-chip pixel binning is 1x1.

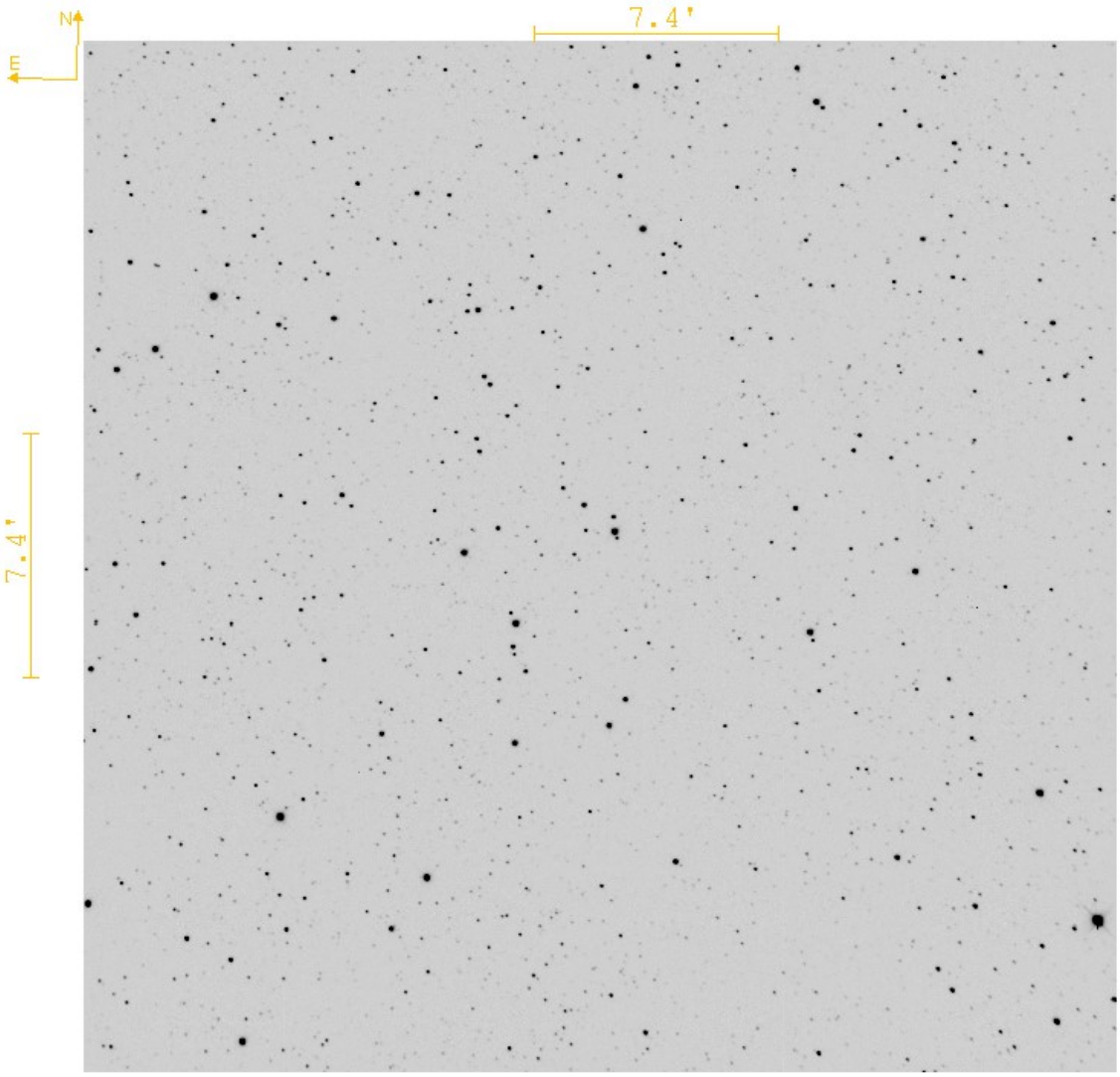

Figure 2-1 The northern field has RA, DEC coordinates of 22^{h} 14^{m} 24^{s} and +56° 21’ 49.5”, respectively.

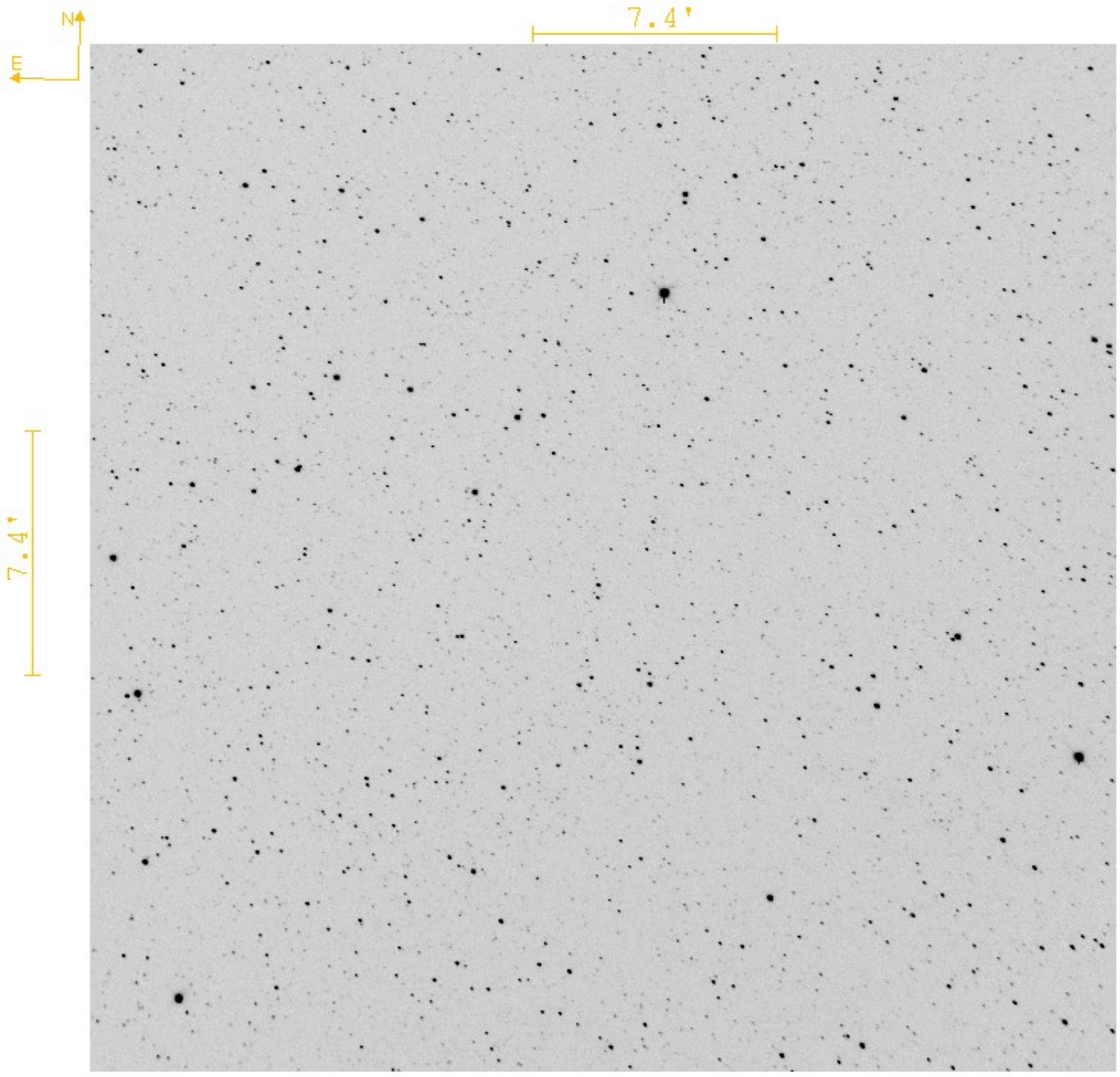

Figure 2-2 The southern field has RA, DEC coordinates of 19^h 26^m 40^s and +27° 11’ 15”.

All raw data images and calibration images were taken at the Ball State Observatory, located on the roof of the Cooper Physical Science building, using the Parallax 20-inch F/8 telescope. This telescope is equipped with a Finger Lakes Instruments (FLI) 4096x4096 pixel (16 million pixels total) CCD camera; we utilize only a near-infrared (NIR) filter in this project. The filter wheel has two slots for filters, so the second slot was empty. Figure 2-3 and 2-4 are pictures of the telescope and camera used for data acquisition.

Figure 2-3 The Parallax 20-inch F/8 telescope was used for data acquisition. It is located on the rooftop of the Cooper Science building on the campus of Ball State University.

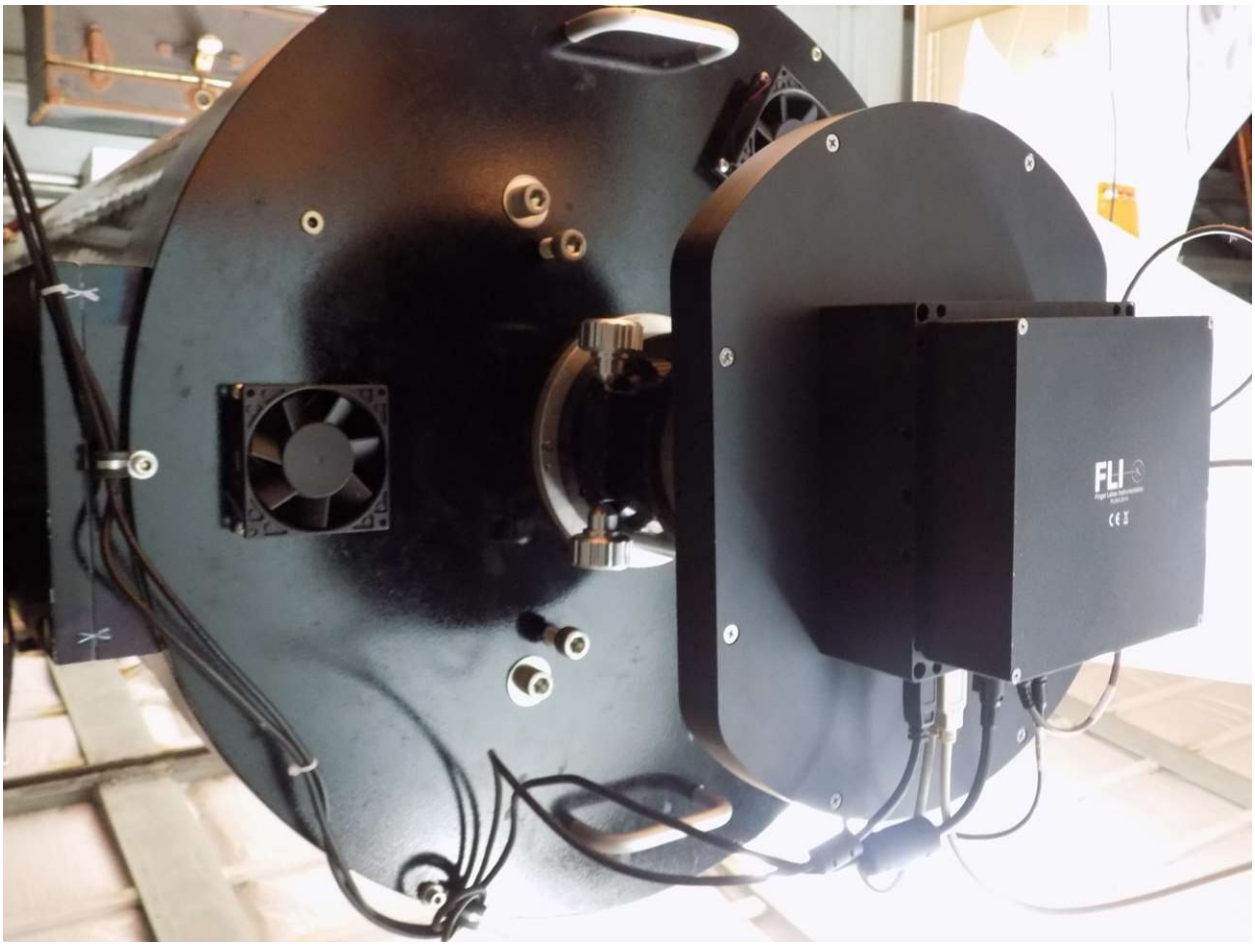

Figure 2-4 The FLI 16 MPixel CCD camera attached to the telescope.

Data were obtained initially during the summer and fall of 2015 until the star fields were too close to the horizon during the nighttime hours, which was approximately 35 degrees. Observations restarted in the summer of 2016 and ended in November 2016. Each field had around 2,000 images taken over the course of the two observable seasons. Slightly more images were taken of the southern field due to a change in exposure time. Approximately 405 initial images were taken at an exposure time of 120 seconds, but eventually a finalized time of 180 seconds was used in order to maximize accuracy without over exposing brighter stars; longer exposures were not possible due to tracking errors. In order to maintain that both fields have the

same amount of observed time, a few more images were taken of the southern field to account for the exposure time alteration. This was done in order to allow a more direct statistical analysis of the two fields if any exoplanets were discovered.

There were several limitations that constrained observing time. Dew point and humidity constrained the amount of observing time due to potential condensation on the mirror of the telescope, mainly occurring at the end of the night. Cloudy nights would diminish seeing capabilities, which would render observations useless. Gusts of winds could perturb the telescope, which would cause smearing and blurring of the images. Nights where the moon was above the horizon and more than a crescent phase would provide too much background light, also rendering the images useless. Table 2-1 shows the observations dates and lunar phase. The moon was below the horizon during observations on the nights that have gibbous phases.

Date	Phase	Date	Phase
8/20/2015	Waxing Cresent	6/24/2016	Waning Gibbous
8/21/2015	Waxing Cresent	6/25/2016	Waning Gibbous
8/22/2015	First Quarter	6/27/2026	Third Quarter
8/24/2015	Waxing Gibbous	6/28/2016	Waning Cresent
9/10/2015	Waning Cresent	6/29/2016	Waning Cresent
9/12/2015	Waning Cresent	7/8/2016	Waxing Cresent
9/13/2015	New	8/1/2016	New
9/14/2015	Waxing Cresent	8/8/2016	Waxing Cresent
9/15/2015	Waxing Cresent	8/22/2016	Waning Gibbous
9/16/2015	Waxing Cresent	9/1/2016	New
9/17/2015	Waxing Cresent	9/2/2016	Waxing Cresent
9/20/2015	First Quarter	9/3/2016	Waxing Cresent
10/4/2015	Third Quarter	9/4/2016	Waxing Cresent
10/7/2015	Waning Cresent	9/22/2016	Third Quarter
10/10/2015	Waning Cresent	10/4/2016	Waxing Cresent
10/11/2015	Waning Cresent	10/13/2016	Waxing Gibbous
10/12/2015	New	10/14/2016	Waxing Gibbous
10/13/2015	Waxing Cresent	10/24/2016	Waning Cresent
10/14/2015	Waxing Cresent	11/3/2016	Waxing Cresent
10/17/2015	Waxing Cresent	11/5/2016	Waxing Cresent
10/18/2015	Waxing Cresent	11/6/2016	Waxing Cresent
10/19/2015	First Quarter		
11/2/2015	Third Quarter		
11/3/2015	Waning Cresent		
11/7/2015	Waning Cresent		
11/8/2015	Waning Cresent		
11/10/2015	New		
11/13/2015	Waxing Cresent		
11/14/2015	Waxing Cresent		
11/15/2015	Waxing Cresent		

Table 2-1 Lunar phase during all observation dates

Three different software programs were used to run the telescope from the observatory's computer. ACP[1], MaxIm DL[2], and FocusMax[3] controlled the physical motion of the telescope, as well as the pointing, the CCD camera, the filter wheels, and the data acquisition scheduling. The computer controlling the telescope utilizes the Windows 10 operating system.

[1] http://acp.dc3.com/index2.html
[2] http://diffractionlimited.com/product/maxim-dl/
[3] http://www.ccdware.com/products/focusmax/

2.2 Observations

The observational process consists of turning on the telescope, preparing the computer, writing a script, executing the script, shutting down the observatory, and transferring data. About an hour and a half before sunset, the observer would enter the observatory. The computer in the control room was turned on. While the computer started, the roof was rolled open through two different buttons and eventually locked once entirely open. At this point, three chords attached to the telescope were plugged into an outlet and a switch was turned on followed by the sound of the camera fans. The computer programs that control the telescope were then started. Using ACP, the temperature of the CCD camera temperature was set to as low as achievable, preferably around -40 degrees Celsius. While the CCD camera cooled through the use of thermoelectric coolers and fans, the nightly script was written for the software to run in an automated way. An example script has been included in Appendix A.

An initial script, which obtains calibration images followed by science images, was generated using ACP Planner 4.2.6. Semicolons are used within the script as comments, which the software ignores when running. The script is initially set up to take flat calibration images at dusk by referencing an automatic flat acquisition script. The “twilight sky flats” script automatically calculated exposure time based on the amount of light. Seven flat images were taken each night. The “twilight sky flats” script also automatically chooses observation locations based on the position of the sun and varies the pointing in order to be able to remove background stars when combining the individual flat images. This “flat script” is included in Appendix B. After the flat acquisition script has run, the next command begins. The code informs the computer to take dark calibration images with on-chip pixel binning of 1x1. The exposure time was set to 180 seconds and the count of images to be taken was set to ten. Occasionally,

depending on the amount of time available for observation, more darks would be taken in order to better characterize the dark current. Once the dark images had been acquired, bias calibration images were scripted to be obtained. Bias exposure times are zero seconds, the binning was set to one, and count was set to ten.

The script then commanded the telescope to perform autofocus and pointing calibrations. These procedures involve exposing the CCD to fields of stars at various positions and matching bright stars to known stars through an online database in order to guarantee the telescope is properly focused and points accurately.

Once these procedures were completed, the acquisition of science images began. This is scripted similarly to the acquisition of dark and bias images, except the filter is specified as NIR_Empty and the output files are given name indexes and coordinates of the target fields are set. Due to tracking errors that prevented the telescope from maintaining the exact coordinates, the coordinates were shifted a tenth of an arc-second every ten images in the script. This "trick" forced the telescope to reposition and perform a quick pointing recalibration, which includes re-centering. This appeared to correct the errors effectively, resulting in images that were centered on the intended location. Once all of the images were obtained, a shutdown script was called that slowly warmed up the CCD and parked the telescope.

Once the script was running and gathering calibration images, the observatory would occasionally be left to run overnight. The weather was watched closely to make sure the humidity did not rise past a point that would lead to condensation. Once the script had finished, an observer would return to the observatory and shut down the rest of the software and hardware. The nightly data was then backed up onto a single terabyte external hard drive. Data would then

be reduced by using the Image Reduction and Analysis Facility[4] (IRAF) software in preparation for usage in differential photometry software.

In order to properly use the differential photometry software required for analyzing the data, the CCD's gain and readnoise had to be measured. Two wall flat images and two bias images were taken to calculate these parameters. The values for the averages over all pixels and variances between each set of images were obtained and equation 2.1 and equation 2.2 (from Birney, Gonzalez, Oesper 2006, pgs 178, 179) were used to calculate gain. Then equation 2.3 was used to calculate the readnoise.

$$g^2\sigma^2{}_{F1-F2} = g^2\sigma^2{}_{Poiss} + g^2\sigma^2{}_{B1-B2} \qquad \text{(Equation 2.1)}$$

$$g^2\sigma^2{}_{Poiss} = g(\overline{F2} + \overline{F1}) - (\overline{B1} + \overline{B2}) \qquad \text{(Equation 2.2)}$$

$$g^2\sigma^2{}_{B2-B1} = g^2(\sigma^2{}_{B1} + \sigma^2{}_{B1}) = 2\sigma^2{}_R \qquad \text{(Equation 2.3)}$$

Table 2-2 contains the corresponding values used to determine gain. The value for gain was calculated to be 1.69 electrons/count and the readnoise was calculated to be 16.78e$^-$ R.M.S.

[4] http://iraf.noao.edu/

Statistical Variable	Measured Value
$\boldsymbol{\sigma^2_{F1-F2}}$ Variance from flat difference image	$188.3^2 = 35456.89$
$\boldsymbol{\sigma^2_{B1-B2}}$ Variance from bias difference image	$13.96^2 = 194.8816$
$\boldsymbol{\sigma^2_{B1}}$ Variance from bias image 1	$9.933^2 = 98.66$
$\boldsymbol{\sigma^2_{B2}}$ Variance from bias image 2	$9.928^2 = 98.57$
$\boldsymbol{\overline{F1}}$ Average over all pixels of flat image 1	*30690*
$\boldsymbol{\overline{F2}}$ Average over all pixels of flat image 2	*30920*
$\boldsymbol{\overline{B1}}$ Average over all pixels of bias image 1	*1004*
$\boldsymbol{\overline{B2}}$ Average over all pixels of bias image 2	*1003*

Table 2-2 Statistical measurements were obtained to calculate telescope gain and saturation.

Chapter 3

Data Reduction

3.1 IRAF Setup and Installation

Once the data have been acquired, it must be processed in order to remove systematic noise. Manual installations of IRAF can be done on Macintosh operating systems as well as Linux operating systems. For this study, a compiled operating system package based on the Debian distribution called "distroastro" was used.[5] The system was 32-bit, and bash was used as the command language. This specific distribution included pre-installed astronomy software, such as IRAF and ds9 (a program for displaying images).

Once IRAF was properly installed, a few settings were adjusted. Within the IRAF directory, the file "login.cl" was edited using the bash command "gedit". The setting for image dimension was set so "stdimage" is equal to "imt4096". This line informs IRAF of the pixel dimensions that are to be expected for the data reduction process. The setting for extension type was also changed such that "imtype" is equal to "fits". This line instructs IRAF to expect image files with the ".fits" extension (Tody & Fitzpartick 1995).

Another step for setting up IRAF is creating a bad pixel mask. This is a collection of coordinates of pixels that are not functioning correctly. Dead pixels can be observed easily in flat images as they are completely dark with zero counts after an exposure. After loading a flat image into the ds9 window within IRAF using the display command, the cursor can be used to determine the coordinates of the bad pixel. The same process can be administered with dark images in order to find "hot" pixels that have too many counts. Removing these two sources of error is needed to avoid false detections of stellar variability.

[5] http://www.distroastro.org/

Once the coordinates of the bad pixels have been identified, they are entered into a text file. IRAF reads the file line by line and determines the pixel coordinates though a specific formatting. The first values, an initial x and y component, are separated by a space. The second coordinates are separated by the first with another space. IRAF then interpolates over all pixels between the initial and final pixel coordinates for each line. The pixel mask used for this project is included in Appendix C.

The next setup step is to set several parameters in the **ccdproc** file. Once in the correct directory, the **ccdproc** file can be altered by using IRAF's built in text editing command, **epar**. The first parameter is "images," which will be set to the name of a list of image files to be processed. The output setting is left blank so that the images are overwritten. Backups of these images files and calibration files were stored on an external terabyte hard drive. The "ccdtype" parameter was left blank in order to allow all image types for processing. The "fixpix" parameter should be set to "yes" in order to inform IRAF to look for a bad pixel mask file. The "fixfile" parameter would then be set to the name of the file. For this project, a master pixel mask was named "pixelmask.txt." The "overscan" parameter was set to "yes" which applies the first bias correction that will be discussed in Chapter 3.2. The "trim" parameter was also set to "yes". The "trimsec" parameter was set to a value that trimmed off the edges of the picture and set the total size as 4066 pixels by 4066 pixels which is formatted within **ccdproc** as "[60:4125,52:4117]". An example of the **ccdproc** settings are included in Appendix D. Once these parameters were set, the bias corrections were found (Kindt 2015).

3.2 Bias Correction

Applying bias corrections was the first step in the reduction process. Each image from a

CCD chip inherently has a count offset due to the internal bias setting. This offset can vary somewhat in time and location on the chip. In order to correct for these effects, the value of the bias for each pixel must be determined and subtracted (Birney, Gonzalez, & Oesper 2006, pg 171).

The first of two types of bias corrections applied in this study was the implementation of the overscan region correction. The overscan region can be seen on the side of each raw image. The dark columns include information about the row's bias offset during the chip readout step. The size of the overscan region for this study was 83 pixels wide. The IRAF command **implot** was used to identify the overscan region coordinates that were later entered into **ccdproc**. The "overscan" parameter in **ccdproc** was set to "yes" and the "biassec" parameter was set to "[4150:4232,52:4117]". The first few overscan corrections functions were interactively fit for confirmation that a Legendre fit of order 5 was sufficient.

Initially, a new image was created during each correction step throughout the reduction process. With the amount of images used in this study, this practice became very storage intensive. Therefore, once the process had been proven effective, only raw data files and completely reduced images were saved.

The second bias correction step was applied by creating a master bias image using the IRAF command **zerocombine** and setting the **ccdproc** parameter "zerocor" to "yes". The master bias was easily created using **zerocombine** by first creating a simple text file that contained the names of the bias images for the observation night. The **zerocombine** parameters were edited within IRAF using the **epa**r command. The "reject" parameter was set to "minmax" and the "combine" parameter was set to "median". This informs the command to ignore minimum and maximum pixel values before combining the bias images by using the median pixel values. The

zerocombine command also allows the user to name the resultant master bias image. This name is used in **ccdproc** contained in quotation marks as the zero parameter. A sample of the **zerocombine** parameters is included in Appendix E. A sample of a resultant master bias can be seen in Figure 3-1.

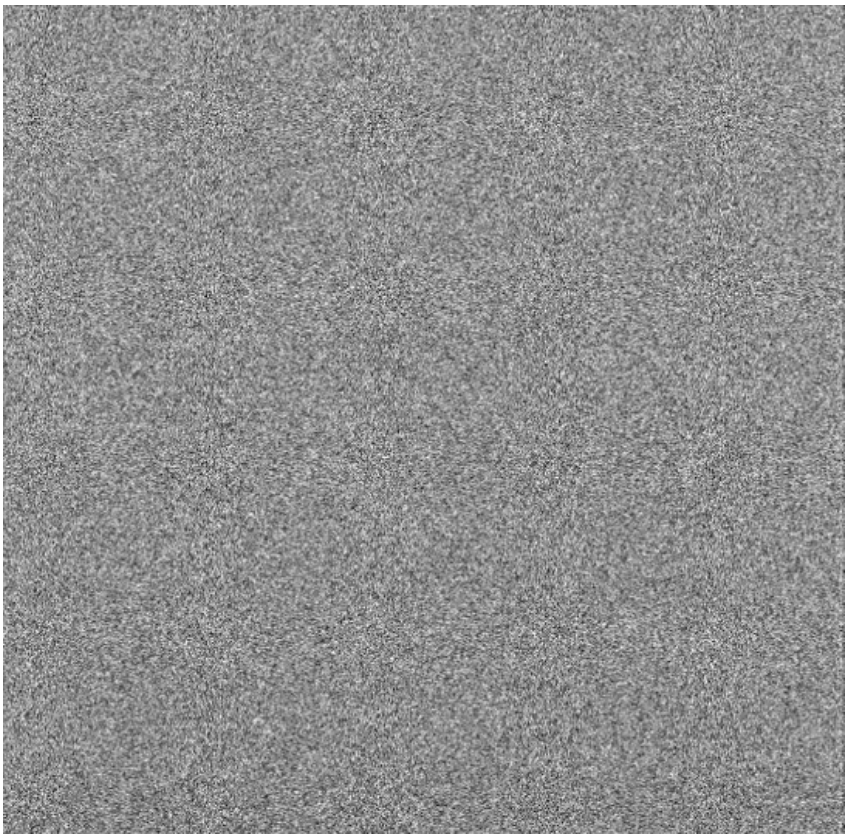

Figure 3-1 A master bias image was created using **zerocombine**.

3.3 Dark Correction

The next step in the data reduction process is applying the dark correction. This was accomplished by creating a master dark using **darkcombine** and setting the **ccdproc** parameter "darkcor" to "yes". Within **darkcombine**, the "combine" parameter was set to "average" and the "reject" parameter was set to "minmax". This ensures that the master dark is created in a way

that best captures the effects of the dark current from the CCD chip. In this study, multiple dark images were acquired during observations. All darks had the same exposure time of the data images. Another way to create an accurate dark image is to simply expose for a long duration and scale that image automatically within **ccdproc**. A sample of the **darkcombine** parameters is included in Appendix F. An example of a master dark can be observed in Figure 3-2.

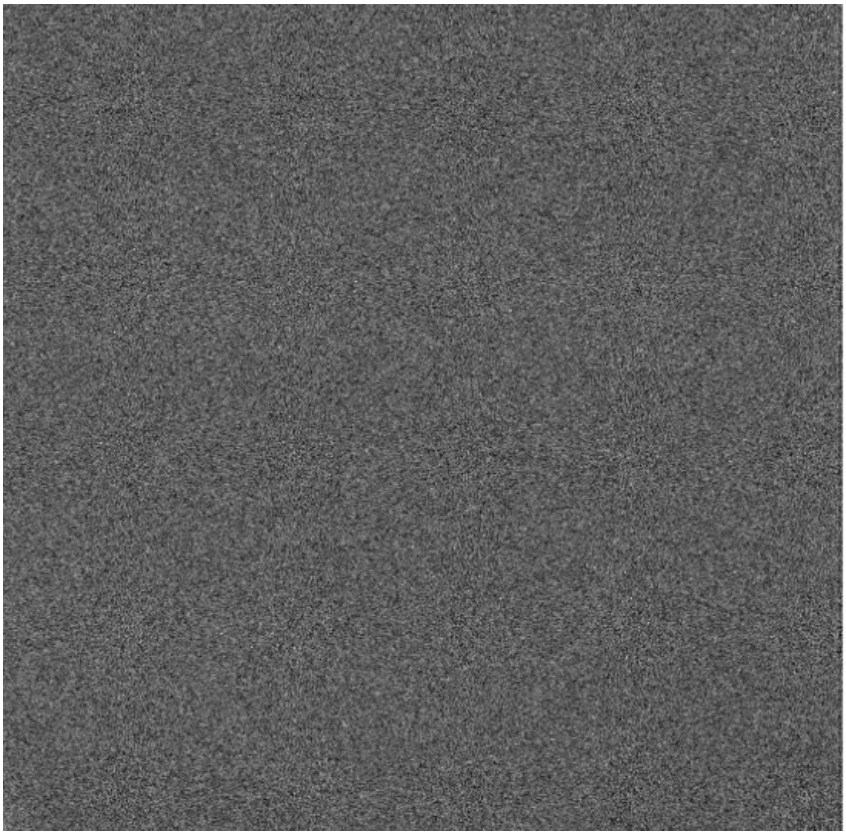

Figure 3-2 A master dark image was created using **darkcombine**.

3.4 Flat Correction

The last correction image created for the data reduction process was the master twilight sky flat. Applying the flat correction rectifies the variations in pixel gains as well as the multiplicative noise caused by dust particles in addition to lens, mirror, and filter imperfections (Kindt 2015).

In order to make a master flat image, **flatcombine** was used. A list of each night's flat field images was created and set as the "input" parameter within **flatcombine**. The "combine" parameter was set to "median" in order to eliminate the effects of background stars and potential cosmic ray hits. This can be seen by comparing Figure 3-3 to Figure 3-4. Once the master flat had been created, **imstat** was used to determine the mode of the image. In order to normalize the master flat, each pixel within the image was divided by the mode. This was applied using **imarith**. To confirm that the master flat had been prepared correctly, **imstat** was then employed again. The final images had a median value equal to one, which confirms they were prepared correctly. In order to apply the flat correction, the "flatcor" parameter in **ccdproc** was set to "yes" and the file name of the master flat image was set as the "flat" parameter. A sample of the **flatcombine** parameters is included in Appendix G.

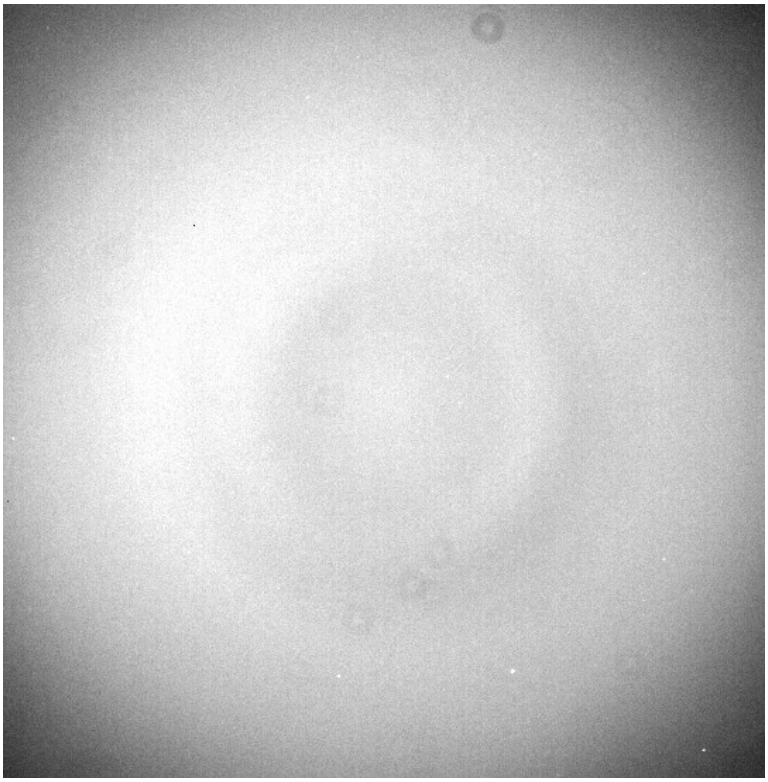

Figure 3-3 Background stars can be observed in a single flat image.

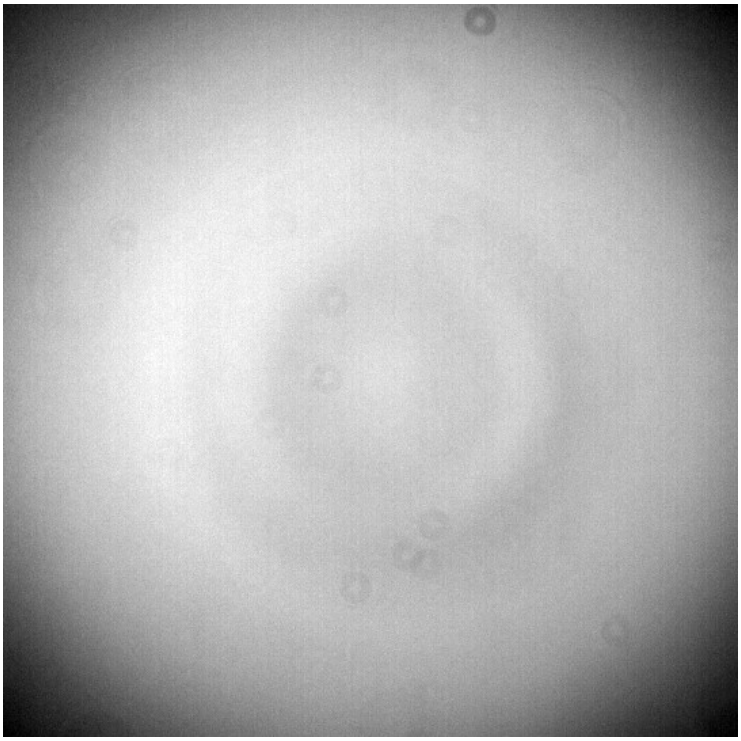

Figure 3-4 Background stars are no longer visible in the median combined master flat.

3.5 Running ccdproc

Utilizing **ccdproc**, reducing an entire night of data became a streamlined and easily repeatable process. Within the nightly directory, four lists were made based on file names. These lists were separated into bias images, dark images, flat images, and science images. The bad pixel mask was then copied into the directory. The “dark”, “zero”, and “flat” parameters of **ccdproc** were all set to “no” utilizing **epar** and the “input” parameter was set to empty quotation marks. The **zerocombine** command was then run. The “output” parameter was previously set as “Zero1.fts” so that for each nightly directory, the master flat had the same name. This allowed fewer steps to be taken between each reduction process for each night. The **darkcombine** command was then run with the resultant master dark being named “Dark1.fts”. The master flat was then created with the name “Flat1.fts” which was then inspected with **imstat**. The master flat was then divided by the mode using the command **imarith** which created a normalize master flat named “Flat2.fts”. The “dark”, “zero”, and “flat” parameters of **ccdproc** were then all set to “yes” and the “input” parameter was set to the name of science image list. The **ccdproc** command was then run, which implemented all of the corrections. A few reduced images were then plotted next to the raw image in order to confirm the reduction process was successful. An example of this is shown in Figure 3-5. Once all of the reduced images were created, all files within the directory were given a suffix that identified the nightly directory they originated from. The completed directory was then backed up onto the external hard drive.

a) b)

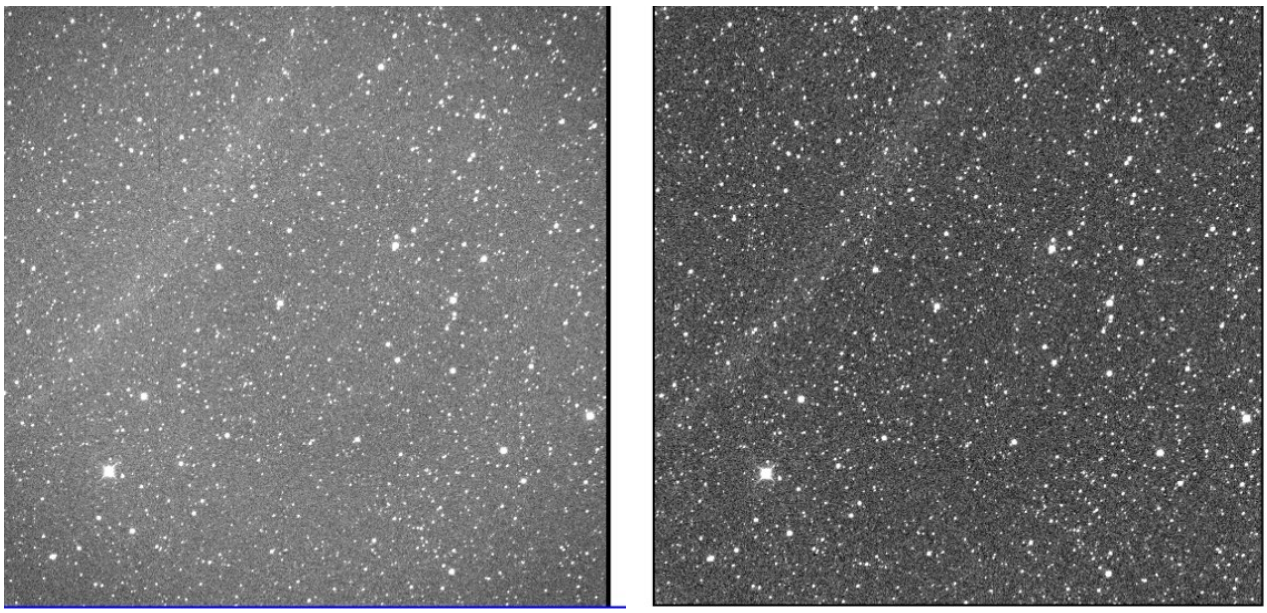

Figure 3-5 A side-by-side comparison of a raw image (a) and a completely reduced image (b) shows the effectiveness of the reduction process.

Chapter 4

VaST

4.1 Setup and Installation

The Variable Search Toolkit (VaST)[6] is a Unix-based software package that utilizes aperture or PSF-fitting differential photometry in order to determine variability of multiple stars within a field simultaneously. Installation is dependent on multiple software requirements, most of which are included in Linux distributions. In order to use PSF-fitting, two other programs are required, Source Extractor (SExtractor) and PSF Exractor (PSFEx). A detailed installation process of these software packages can be found in Kindt (2015).

The PSF-photometry software is dependent on the characteristics of the camera used for data acquisition. The gain and readnoise calculated in Chapter 2 were then entered into a parameter file, "default.sex", which is contained in the VaST installation directory. Since the CCD has a 16 bit A/D converter, the saturation was set just below the value of 2^{16} at the exact value of 65,000 (Birney, Gonzalez, Oesper, pg 177, 2006). Non-linearity sets in below this value, but VaST only uses this number to filter sources with SExtractor. This filtering process parses through each image and identifies outliers of a size versus instrumental magnitude plot. Outlying sources that are blended or saturated will be flagged by SExtractor with a specific number ranging from 0 to 7. VaST only uses non-blended and non-saturated stars that have a flag value of 0 or 1(Sokolovsky, K. & Lebedev A. 2017).

4.2 PSF Photometry

Point-spread function (PSF) photometry was used in this project due to the crowded

[6] http://scan.sai.msu.ru/vast/

fields that were observed. According to Heasley (1999), every point source that is imaged by a telescope can be represented as a point-spread function. As long as the source does not move spatially, then its PSF can be modeled. An entire image can then be modeled by making several passes of PSF fitting. The brightest stars are modeled first and then subtracted from the image. Sky levels are then determined from the residual and fainter stars are identified. This is repeated until all stars are modeled. The resultant PSF image can then be used in differential photometry. This is very useful for crowded fields where aperture photometry would most likely have multiple other stars within the stellar annuli. This causes significant errors for aperture photometry.

During the initial observations of the southern field, an exposure time of 120 seconds was used. Once the observers became accustomed to the telescope and the data were inspected, the exposure time was increased to 180 seconds. This change should not have an effect on the quality of the PSF though.

4.3 Input

Running VaST is simply done by entering a one-line command that includes optional parameters and directions to the directory containing the images. The parameters used in this study are indicated by "P" for PSF photometry and "y" for systematic trend removal with ten iterations. The placement of these characters can be seen in the one-line command below.

```
./vast –Py 10 ~/image_directory/*.fts
```

In Kindt (2015), various numbers of iterations were tested in order to minimize the number of

stars that were similarly variable in a systematic way. If all stars from a few nights are all equally brighter or dimmer compared to the majority of the other nights, their brightness can be adjusted. This would qualify as a removal of a systematic trend. Values from one to thirty iterations of systematic trend removal were tested and the number of stars affected decreased with every iteration. The number eventually stabilized to a constant value around ten iterations. Therefore, a value of ten was used for this study. A test trial was run with twenty iterations on the southern field, but no change was noticeable in the standard errors of the resultant light curves.

4.4 Output

While running, VaST checks each image for pier-flips[7] and matches stars in the current image with stars in the previous image in order to align objects. If an image is too distorted or no stars can be matched, the image is automatically flagged and rejected by the software. When an object is identified, it is given a number and specific details about the object are appended to a data file. These details include Julian day, instrumental magnitude, error, pixel coordinates, and image file name.

The initial output from VaST is shown on a GUI that displays standard deviation versus instrumental magnitude, see Figure 4-1. This displays stars that are measured to be variable. Highly variable stars will be shown above the majority of the stars plotted. Exoplanet candidates have smaller variability, and therefore they would be located in the middle of the large grouping of stars, close to the red dotted line. A star's variability is determined in VaST by calculating variability indices such as the brightness scattering, light curve smoothness, and strength of periodic signal (Sokolovsky & Lebedev 2017). If the standard deviation is large, the variability

[7] A pier-flip is a repositioning of a telescope that maintains balance on the telescope's base and allows the prevention of potential collisions of the counter weights and the base.

will be more noticeable. A few long period variable stars were initially identified through this GUI. By left-clicking on a data point in the initial window, a second window appears displaying instrumental magnitude versus Julian day. This can be seen in Figure 4-2. Once a star has been inspected, the data point associated with that star turns green for the user's benefit.

Once an individual light curve has been inspected, a user may left-click on a specific data point within the light curve that then pops up another window displaying the coordinates of that specific star as well as the file name as seen in Figure 4-3. This was very useful for determining the Right Ascension and Declination of a star.

In order to navigate VaST effectively requires knowledge of some controls. Right-clicking on any window will close that window. Zooming is achieved by pressing the "z" button on the keyboard with your mouse at one corner of the desired new display and then left-clicking at the other corner of the desired new display. Pressing the "z" button twice in a row will reset the zoom to default. In the initial window, pressing the "m" or "n" button on the keyboard will cycle through potentially useful displays of the entire data set, such as Figure 4-4 or Figure 4-5. Entering the following command will reload a data set.

```
./find_candidates
```

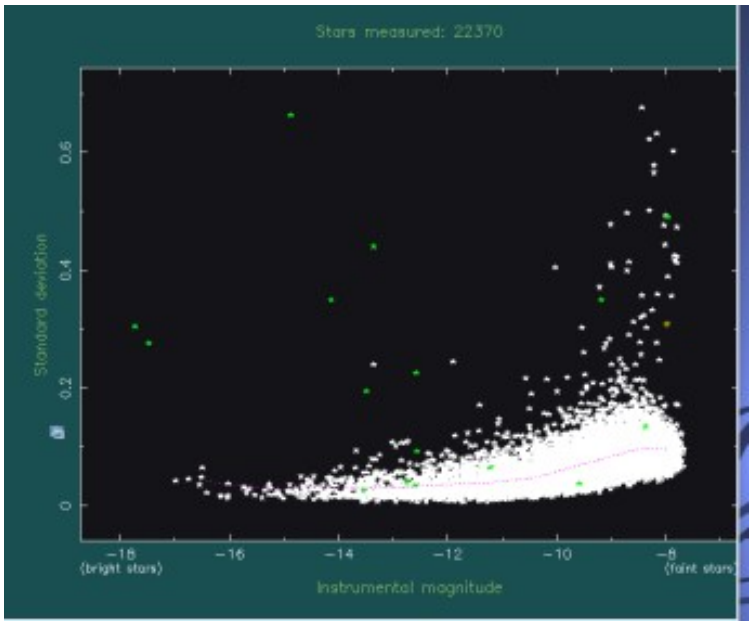

Figure 4-1 Standard Deviation versus Instrumental Magnitude (southern field)

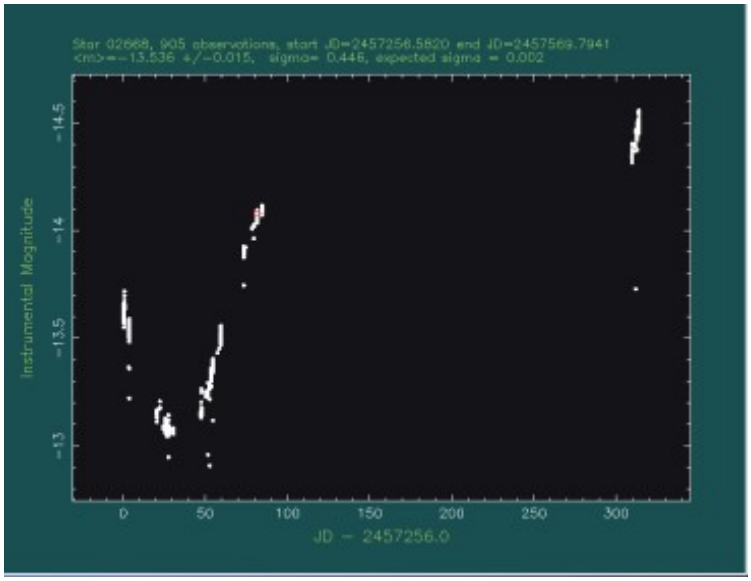

Figure 4-2 GUI of an individual variable star candidate obtained through VaST interface

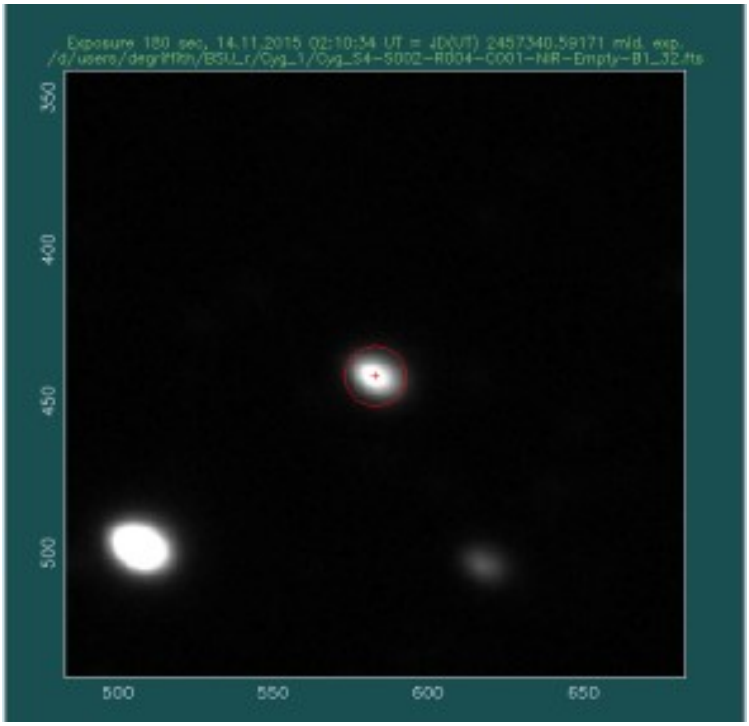

Figure 4-3 GUI of a star with pixel coordinates obtained by clicking on a single data point of a light curve

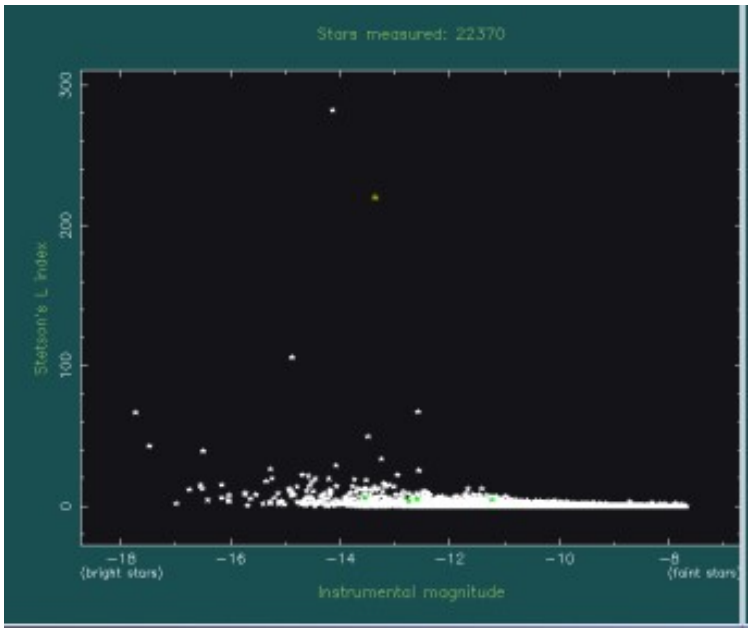

Figure 4-4 Stetson's L Index versus Instrumental Magnitude

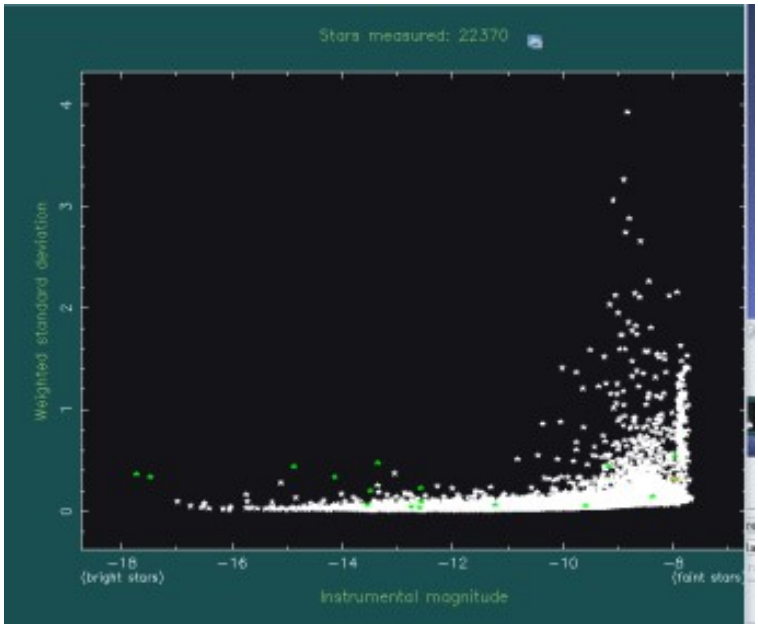

Figure 4-5 Weighted Standard Deviation versus Instrumental Magnitude

Chapter 5

UPSILON

5.1 Installation and Usage of UPSILON

The Automated Classification of Periodic Variable Stars using Machine Learning (UPSILON) software was implemented in this project in order to classify newly discovered variable stars. The software installation depends on python 2.7 or 3.5, numpy 1.11.2, scipy 0.18.1, and scikit-learn 0.18.1. The pip installation of UPSILON will automatically install these dependencies if the user does not already have them.

In order to minimize the amount of computational time and maximize the amount of useful data processed, a histogram was made of the number of light curves versus the number of data points per light curve. As noticeable in Figure 5-1, there were several light curves created by VaST that only had ten or fewer data points. This figure only displays light curves that have 250 or fewer data points in order to show the features of the histogram more effectively. The most data points contained in a single light curve was 1442. An initial minimum cutoff was decided as fifteen points in order to remove a large bulk of non-useful light curves.

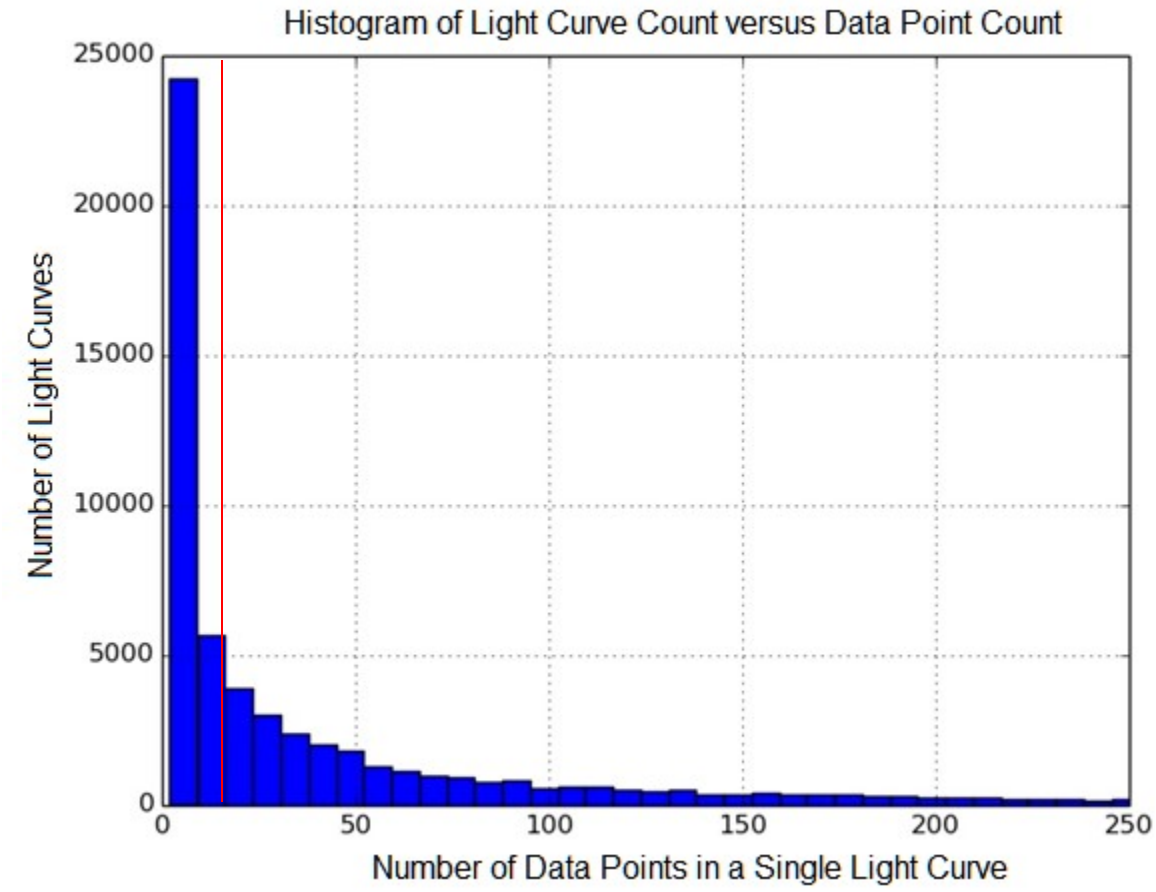

Figure 5-1 Histogram made to determine the best statistical cutoff (shown in red) for analysis of variability.

UPSILON extracts features from an inputted light curve and compares them to known features of well-sampled variable stars in order to classify the inputted light curve. Sixteen different variability features are used in order to constrain the classification. This list of features includes period derived by the Lomb-Scargle algorithm, amplitude ratios, phase differences, skewness, normality, and Stetson K index. The software also provides a probability of correct classification and a flagging number that identifies potentially aliased classifications. A flagging number of "zero" corresponds to a classification that has eighty or more data points and does not

a have a period of variability that matches an observational harmonic. A flagging number of "one" indicates that there is insufficient data for a statistically significant classification, or that the classification may be compromised by aliased periodicity.

In order to prepare light curves for UPSILON, a simple Python script was written to make copies of the original light curves and to trim off unneeded columns of data. The columns of the data files for the light curves were Julian date, magnitude, and standard error. Another Python script was written to use UPSILON on the light curves. The output was a list of names of light curves with classifications, probabilities, periods of variability, and a flagging number. These text files for both fields were then reviewed in order to identify potential new variable stars. All flagged light curves were ignored, many of which had aliased periods close to one day (Kim 2015).

5.2 Variable Star Results from UPSILON

Once several variable star candidates had been classified by UPSILON, the light curves were visually examined using the *Peranso*[8] software. *Peranso* is a light curve and period analysis software package created by Tonny Vanmunster from the CBA Belgium Observatory. *Peranso* is used for analysis by first importing light curve data from a text file and then running the periodicity search tool. For this study, *Peranso* was used primarily to confirm the periods determined by UPSILON. Using the ANOVA period determining method within *Peranso*, the periods of multiple light curves were confirmed within 0.1811 average percent difference.

Two light curves were chosen for a more careful statistical analysis, one from the southern field and one from the northern field. This was done to ensure that the variability was statistically believable. A Legendre best-fit line of order 5 was graphed with the folded light

[8] http://www.peranso.com/

curve and a standard error was calculated from the sum of the residuals for each star. The standard error was then compared to the difference of the minimum and maximum of the best-fit line to confirm the quality of the variability.

The first analyzed light curve was from the southern field, shown in Figures 5-2 and 5-3, and was categorized by UPSILON as a Delta Scuti with a probability of 31%. This categorization was due to the change in magnitude of about 0.4 magnitudes and a period of 0.1961 days. These data are associated with the VaST reference number of out20496. Comparing the standard error to the difference in the minimum and maximum of the best-fit line from Table 5-1 shows that the categorization from UPSILON is believable.

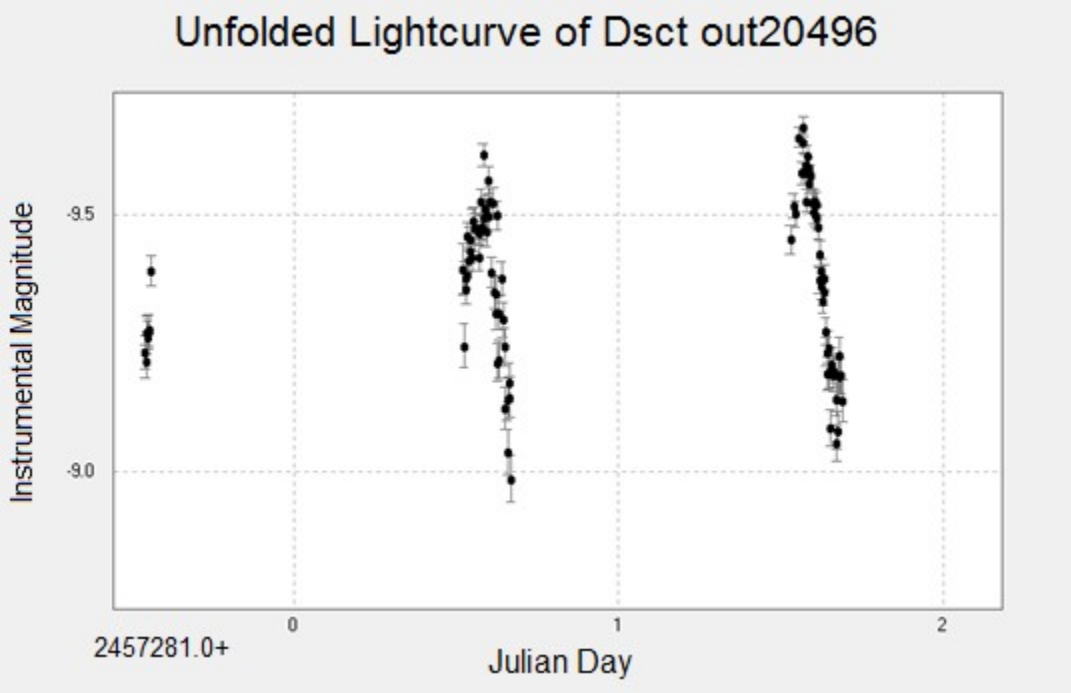

Figure 5-2 Graph of three nights of observations for a Delta Scuti candidate in the southern field.

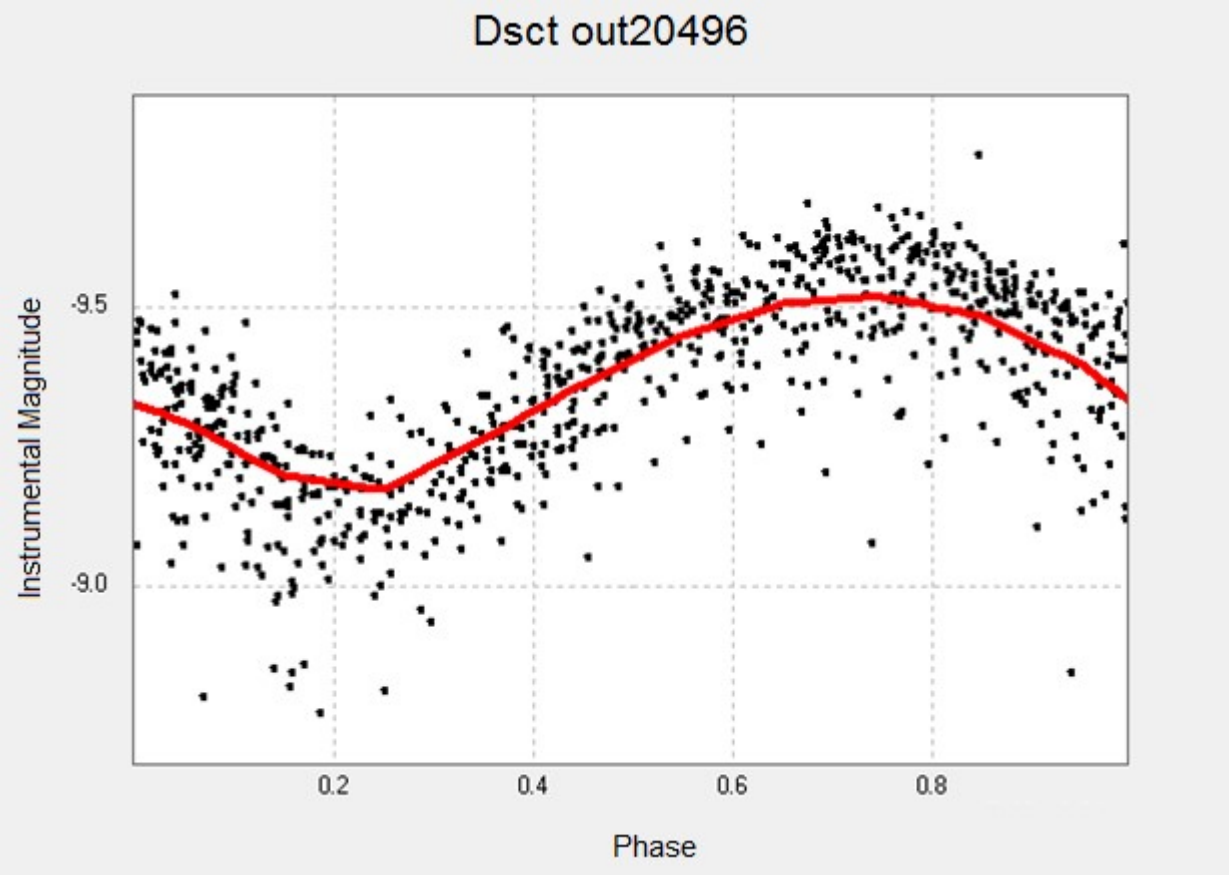

Figure 5-3 Folded light curve of a Delta Scuti candidate from the southen field.

Sum of residuals	N	Standard Error	Minimum of best fit line	Maximum of best fit line	Difference of minimum and maximum	Difference / Standard Error
8.11	771	0.11	-9.54	-9.14	0.40	3.88

Table 5-1 Statistical Analysis of the Delta Scuti candidate from the southen field.

The second analyzed light curve was from the northern field and was categorized by UPSILON as a RR Lyrae with a probability of 61%. This categorization was due to the change in magnitude of about 0.35 magnitudes and a period of 0.311 days. These data are associated with the VaST reference number of out06023. From the summary of the analysis shown in Table 5-2, the categorization from UPSILON is determined to be believable.

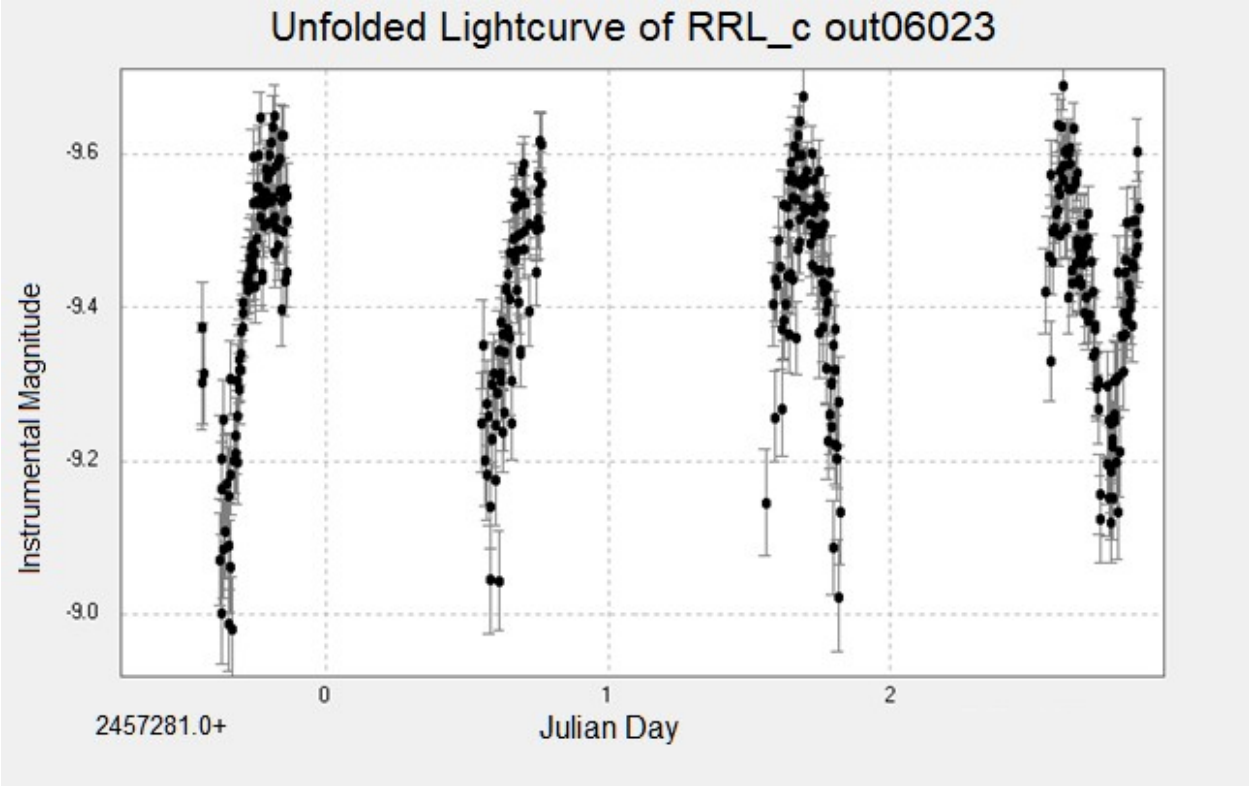

Figure 5-4 Display of four nights of observations for a RR Lyrae candidate.

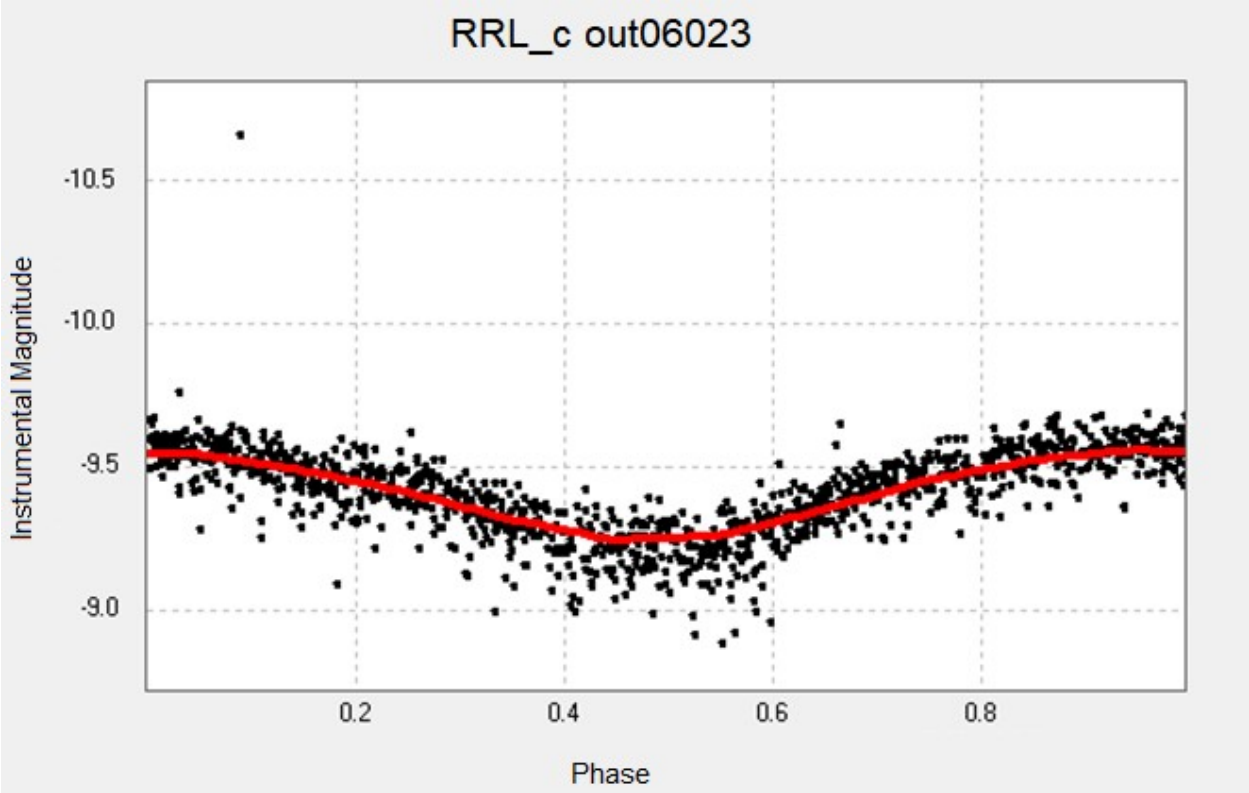

Figure 5-5 Folded light curve of a RR Lyrae candidate from the northern field.

Sum of residuals	N	Standard Error	Minimum of best fit line	Maximum of best fit line	Difference of minimum and maximum	Difference / Standard Error
7.73	1207	0.08	-9.58	-9.24	0.35	4.31

Table 5-2 Statistical Analysis of the RR Lyrae candidate from the northern field

The next step was converting the instrumental near-infrared magnitudes into standard "I" magnitudes. Unfortunately, there was only one reference star in each field in the "I" band. Due to this, all magnitudes for light curves are calibrated from one reference star. Therefore, the estimate magnitude is shown because there is a decent amount of uncertainty with only one calibration star in each field. The star LSPM J 1926+ 2726 has a magnitude in the "I" band of 12.3 and can be found within the southern field. The star G 232-63 has a magnitude in the "I" band of 11.2 and can be found within the northern field. Because these individual stars are not variables, they could not be identified by VaST and therefore were not given a VaST magnitude. For this reason, the software MaxIm DL was used for magnitude calibration using aperture photometry. Multiple variable stars with VaST magnitudes were plotted against an instrumental magnitude from MaxIM DL. The calibration star was included in this plot and the equivalent VaST magnitude was calculated. From this offset, the estimated magnitudes were calculated. All statistically significant variable star categorizations from UPSILON are included in Table 5-3. The classification acronyms are (DSCT) δ Scuti star, (RRL) RR Lyrae, (CEPH) Cepheid, (T2CEPH) Type II Cepheid, (EB) Eclipsing binary, and (LPV) Long-period variable. Subclasses are also included. For eclipsing binaries, the subclasses are: (EC) contact, (ED) detached (ESD) semi-detached (Kim 2015).

Table 5-3 All statistically significant variable star categorizations from UPSILON.

Northern Variable Stars:	Right Ascension Declination	VaST Magnitude	Estimate Magnitude	Average Standard Error	Period (days)	Probability	Classification
out01114	22:13:52.842 +56:36:58.42	-11.990	11.168	0.010	0.195	0.750	EB_EC
out01737	22:13:52.770 +56:34:13.24	-10.600	13.134	0.016	0.099	0.990	DSCT
out02210	22:14:13.195 +56:31:37.54	-13.800	8.607	0.002	0.484	0.410	EB_ESD
out03005	22:13:28.373 +56:27:53.30	-11.900	11.295	0.006	0.574	0.910	EB_ED
out03342	22:13:54.250 +56:25:55.94	-14.270	7.943	0.001	0.167	0.400	EB_ED
out03651 TYC 3990-1519-1	22:13:43.051 +56:24:02.99	-15.270	6.528	0.001	0.107	0.520	EB_ED
out03653	22:14:32.354 +56:24:12.99	-11.300	12.144	0.010	6.125	0.650	EB_ESD
out04066	22:15:33.958 +56:21:38.29	-12.300	10.729	0.005	0.277	0.390	EB_ESD
out04692	22:14:29.966 +56:12:21.24	-10.140	13.784	0.003	0.164	0.620	DSCT
out06023	22:14:10.232 +56:17:56.65	-9.450	14.760	0.046	0.311	0.610	RRL_c
Northern Long Period Variables:	Right Ascension Declination	VaST Magnitude	Estimate Magnitude	Average Standard Error	Period (days)	Probability	Classification
out04749	22:16:01.171 +56:12:13.86	-12.300	10.729	0.011	297.083	0.480	LPV_Mira_AGB_O
out04255	22:15:30.063 +56:20:36.15	-14.000	8.325	0.001	1188.330	0.280	LPV_Mira_AGB_O
out20142	22:16:08.173 +56:05:50.80	-12.000	11.153	0.006	132.037	0.391	LPV_SRV_AGB_O
out22093	22:12:57.581 +56:10:16.02	-12.580	10.333	0.004	1188.330	0.190	LPV_Mira_AGB_C

Southern Variables:	Right Ascension Declination	VaST Magnitude	Estimate Magnitude	Average Standard Error	Period (days)	Probability	Classification
out00223	19:27:11.567 +26:57:33.02	-10.5	13.28	0.0219	0.2685	0.81	RRL_e c
out00419	19:26:32.527 +26:59:30.67	-10.1	13.84	0.0314	0.1594	0.88	DSCT
out01013	19:26:09.301 +27:04:56.98	-9.58	14.58	0.0418	0.9578	0.73	EB_ESD
out02399	19:25:52.100 +27:17:03.98	-10.1	13.84	0.0251	0.1354	0.88	DSCT
out20496	16:26:49.471 +27:15:50.74	-9.57	14.59	0.047	0.1957	0.31	DSCT
Southern Long Period Variables:	Right Ascension Declination	VaST Magnitude	Estimate Magnitude	Average Standard Error	Period (days)	Probability	Classification
out00282	19:26:22.086 +26:58:26.81	-12.64	10.25	0.0023	93.96	0.23	LPV_SRV_AGB_O
out01706	19:25:37.881 +27:11:18.52	-13	9.74	0.0024	469.8	0.2999	LPV_Mira_AGB_O
out02175	19:27:06.455 +27:14:56.76	-11.3	12.14	0.0078	49.45	0.25	LPV_OSARG_AGB
out01666.dat	19:25:35.687 +27:10:59.89	-13.4	9.17	0.0017	93.96	0.27	LPV_SRV_AGB_O
out03077.dat	19:26:11.057 +27:19:55.78	-13.8	8.61	0.0013	134.2		LPV_SRV_AGB_O
out02668.dat	19:27:28.798 +27:22:46.59	-14.51	7.60	0.0015	50.68		LPV_SRV_AGB_O

Chapter 6

VARTOOLS

6.1 Setup and Installation

The program VARTOOLS is an open source command line software designed to analyze light curves and other astronomical data. VARTOOLS includes several commands for modeling, filtering, manipulating, and simulating light curves. The program also includes several batch analysis routines that process multiple light curves at a time and run commands simultaneously (Hartman 2016)[9]. In this project, the Boxed-Least Squares (BLS) routine was used in order to identify potential exoplanet transit candidates.

The installation of VARTOOLS requires the installation of a few dependencies. Python 2.6+, numpy, CFITSIO, PTHRED, GSL, DYNAMIC LIBRARY SUPPORT, and JPL NAIF CSPICE are all required. Once the VARTOOLS file has been downloaded, the user can configure the installation file by typing "./configure" while in the installation directory. The program can then be compiled by typing "make".

6.2 Usage

The BLS method examines a light curve and attempts to fit a periodic square-shaped dip to the data (Kovács et al. 2002). The user is allowed to control and constrain several parameters within the BLS command including transit duration, transit period, number of trial frequencies, number of phase-bins, and number of BLS peaks to print. For this study, potential exoplanet transit durations would be between .041 days and .208 days, and periods would be between one

[9] http://www.astro.princeton.edu/~jhartman/vartools.html

day and ten days (Gonzalez, personal communication June 21, 2017). The five best BLS fits were printed for each light curve. This file displays the determined period, signal to noise ratio, transit depth, transit duration, the number of points in a transit, the number of transits, and the signal to pink noise. All of these results are printed for each potential BLS fit for each light curve.

6.3 Extra Solar Planet Results

The several outputs from the BLS method of VARTOOLS were analyzed for statistical significance. A sample output file is included in Appendix H. A Python script was then written to print out the name of the star, the best period, the associated signal-to-noise ratio, and the signal-to-pink-noise ratio. The resultant list was then filtered by signal-to-pink noise descending in value in order to identify the best candidates (Nardiello 2016). This is done because the signal-to-pink-noise ratio takes into consideration the number of transits detected (N_t) as well as the number of data points within a transit (η_t). The transit depth (δ_m) and "white noise" r.m.s. (σ_w) and "red noise" r.m.s. (σ_r) are also used in the calculation. Red noise is time correlated noise while white noise is uncorrelated noise. Red noise is calculated by subtracting the r.m.s. of the binned light curve if the noise was uncorrelated with time from the r.m.s. of the residual light curve after binning. White noise is obtained from the r.m.s. of the light curve once the transit model has been subtracted (Hartman 2016).

$$\frac{S}{N_{Pink}} = \frac{{\delta_m}^2}{\left(\frac{{\sigma_w}^2}{\eta_t}\right)+\left(\frac{{\sigma_r}^2}{N_t}\right)} \qquad \text{(Equation 6.1)}$$

The best potential exoplanet candidates were then plotted by folding their light curves based on their period from the BLS data file. The model from VARTOOLS was also plotted on top of the folded light curve for visual inspection. Three potential exoplanet candidates from the southern

field had signal-to-pink-noise ratios that indicated statistically significant variability. All three are shown in Figures 6-1 through 6-3. Twenty-eight potential exoplanet candidates from the northern field showed statistically significant variability. The five best are shown in Figures 6-4 through 6-8. All of the statistically significant variable stars from the BLS method from VARTOOLS are included in Table 6-1 in a catalog formatting. Finding charts are included in Appendix I. The five best exoplanet candidates are included in Table 6-2. VARTOOLS calculates the time of mid-transit and outputs the first calculated time based off of the earliest observations. The three southern potential exoplanet candidates shown in Figures 6-1 through 6-3 were determined to not be candidates due to their large transit depth. This is described on more detail in Chapter 7.

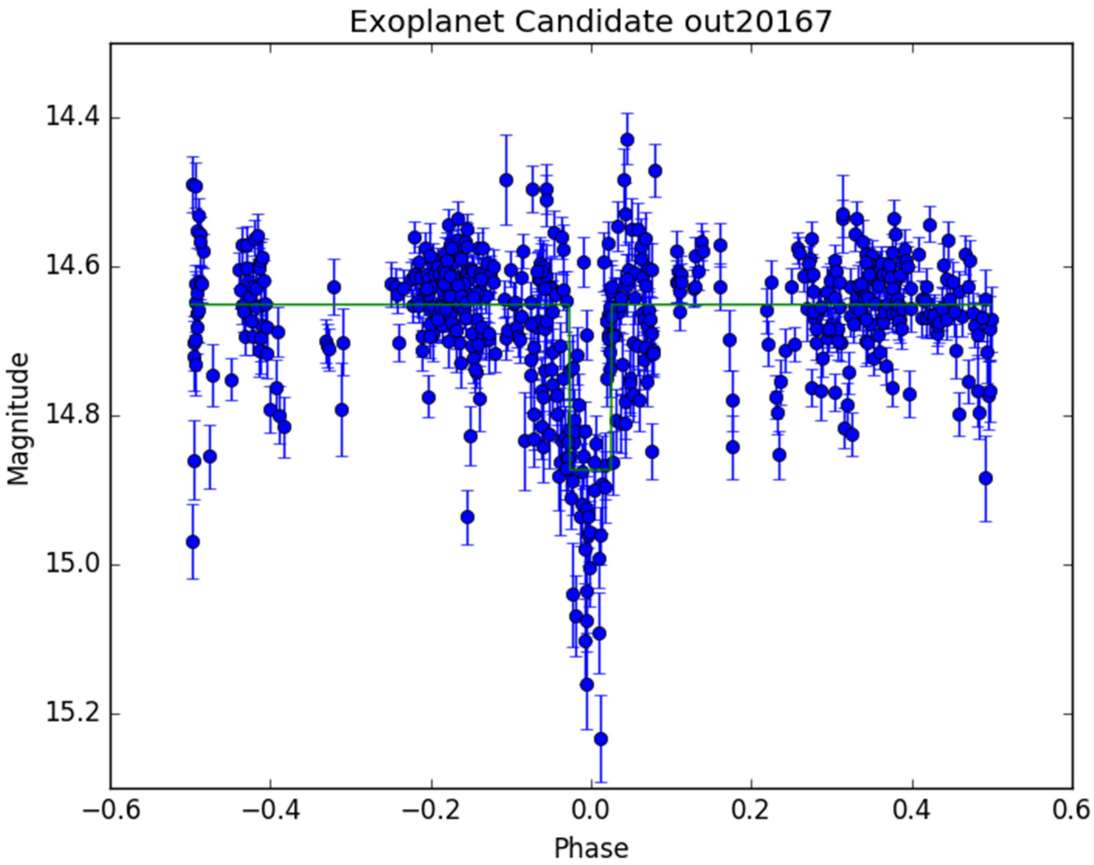

Figure 6-1 Southern exoplanet candidate with 4 transits.

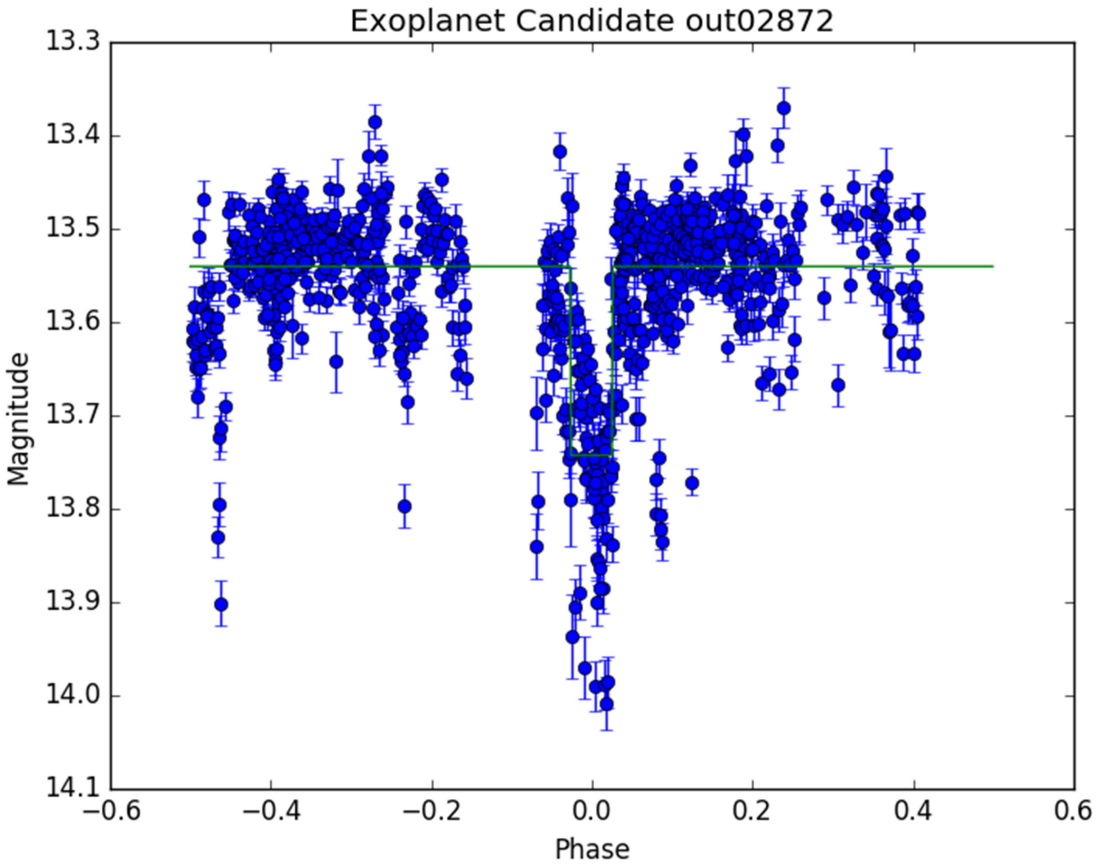

Figure 6-2 Southern exoplanet candidate with 4 transits.

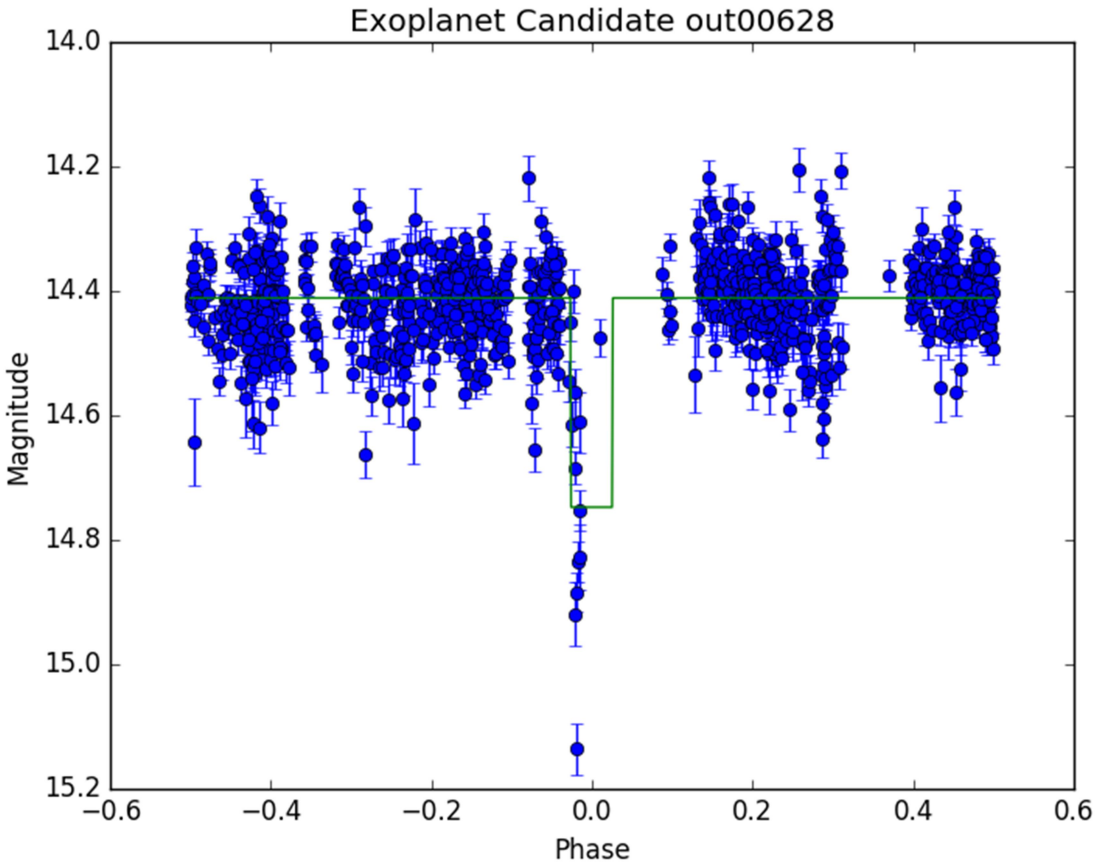

Figure 6-3 Southern exoplanet candidate with 3 transits.

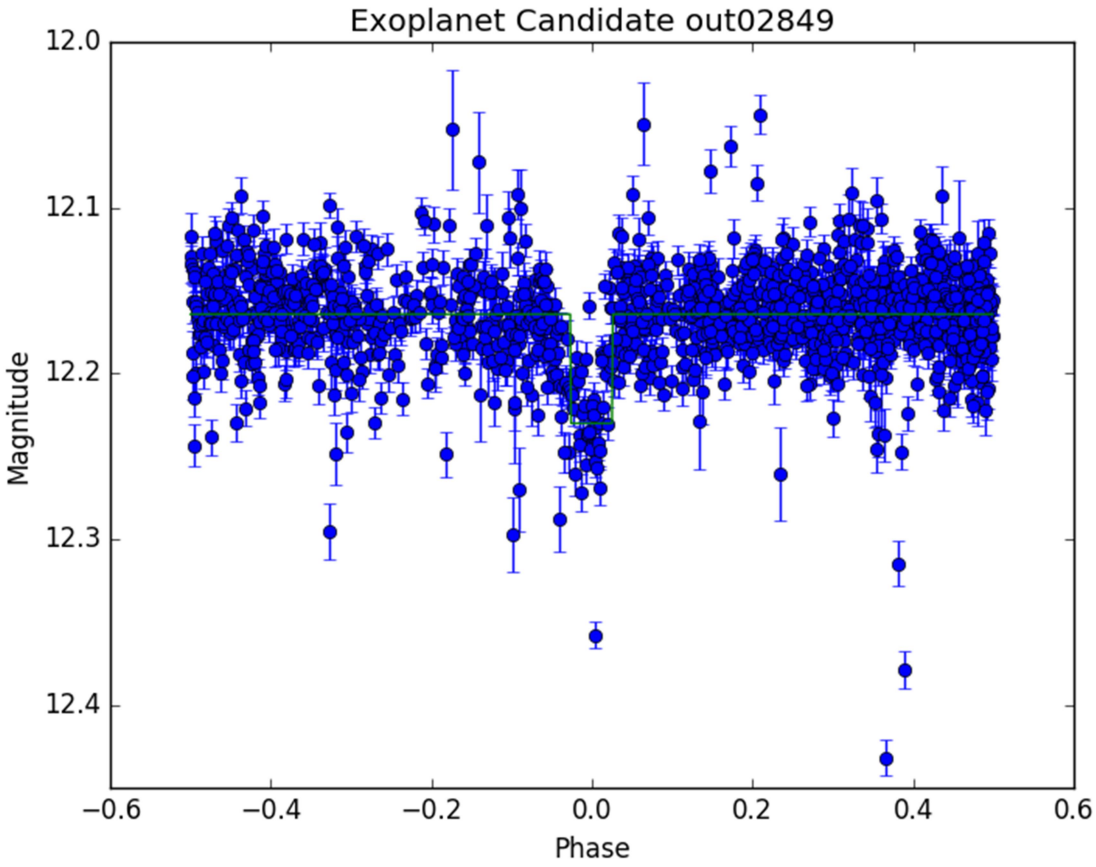

Figure 6-4 Northern exoplanet candidate with 4 transits.

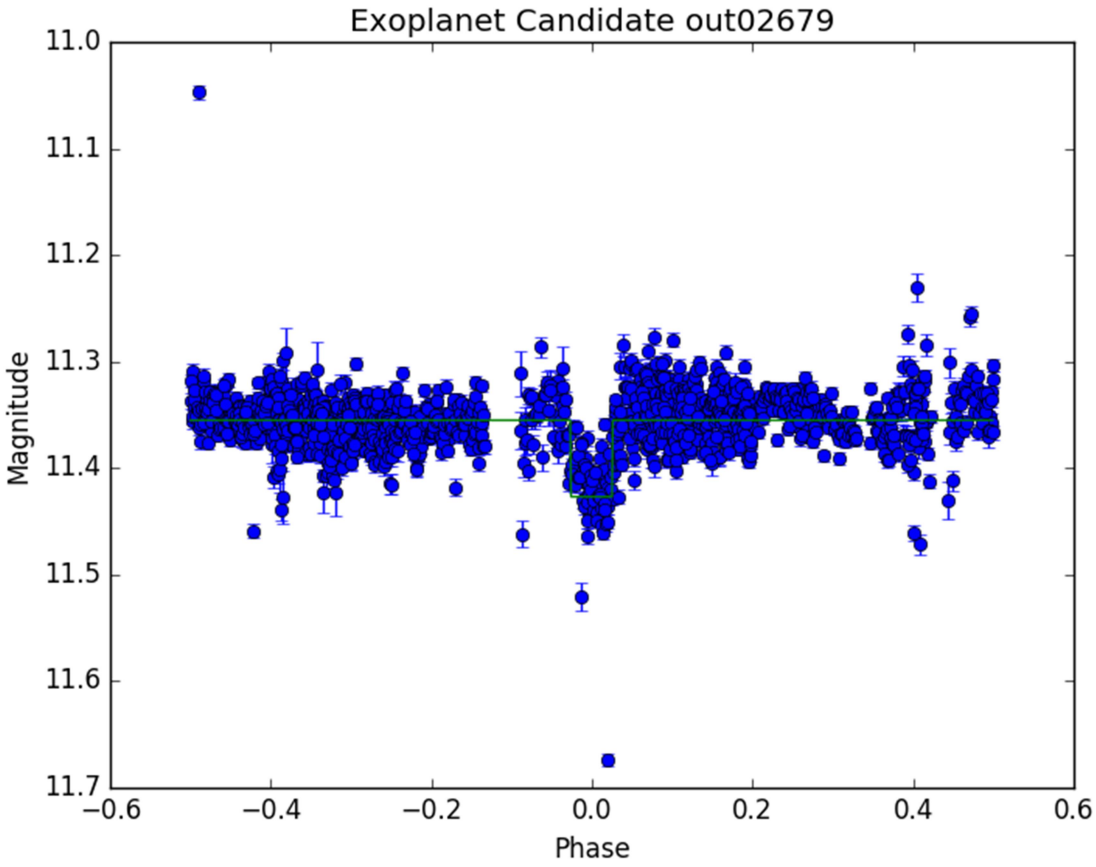

Figure 6-5 Northern exoplanet candidate with 3 transits.

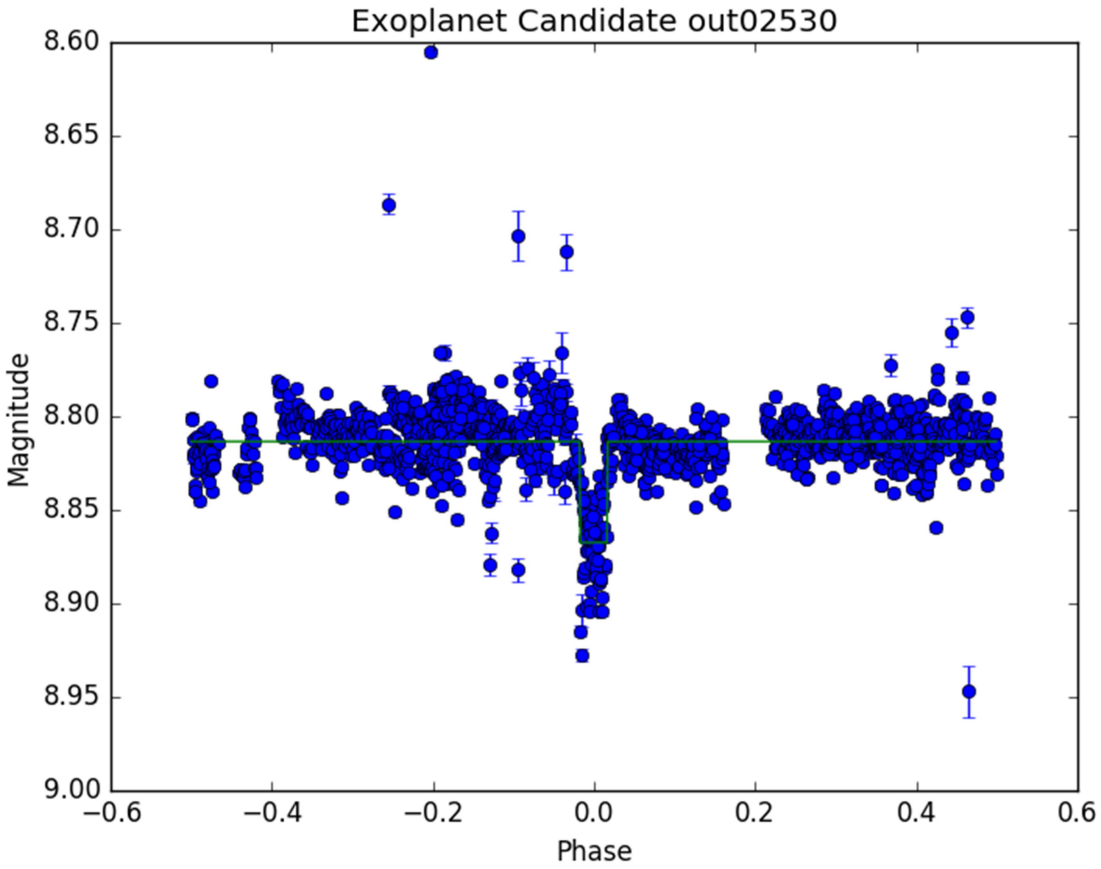

Figure 6-6 Northern exoplanet candidate with 2 transits.

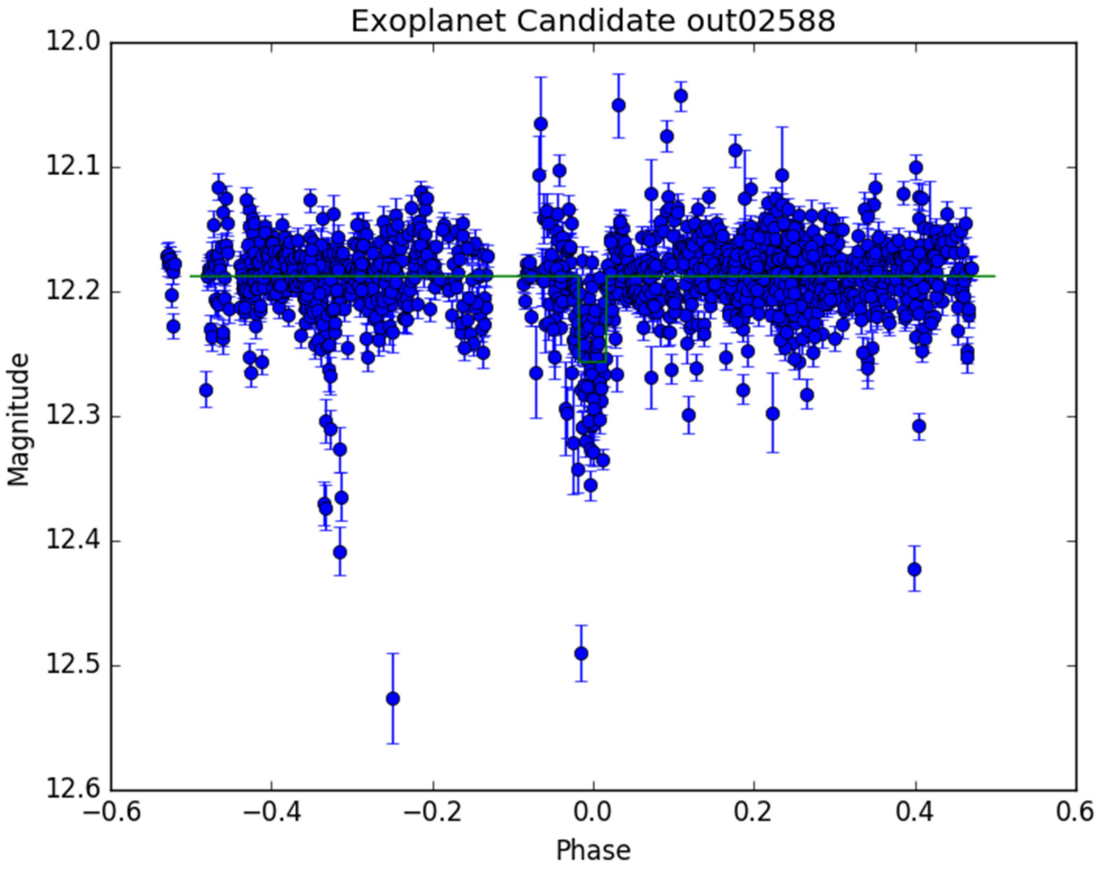

Figure 6-7 Northern exoplanet candidate with 3 transits.

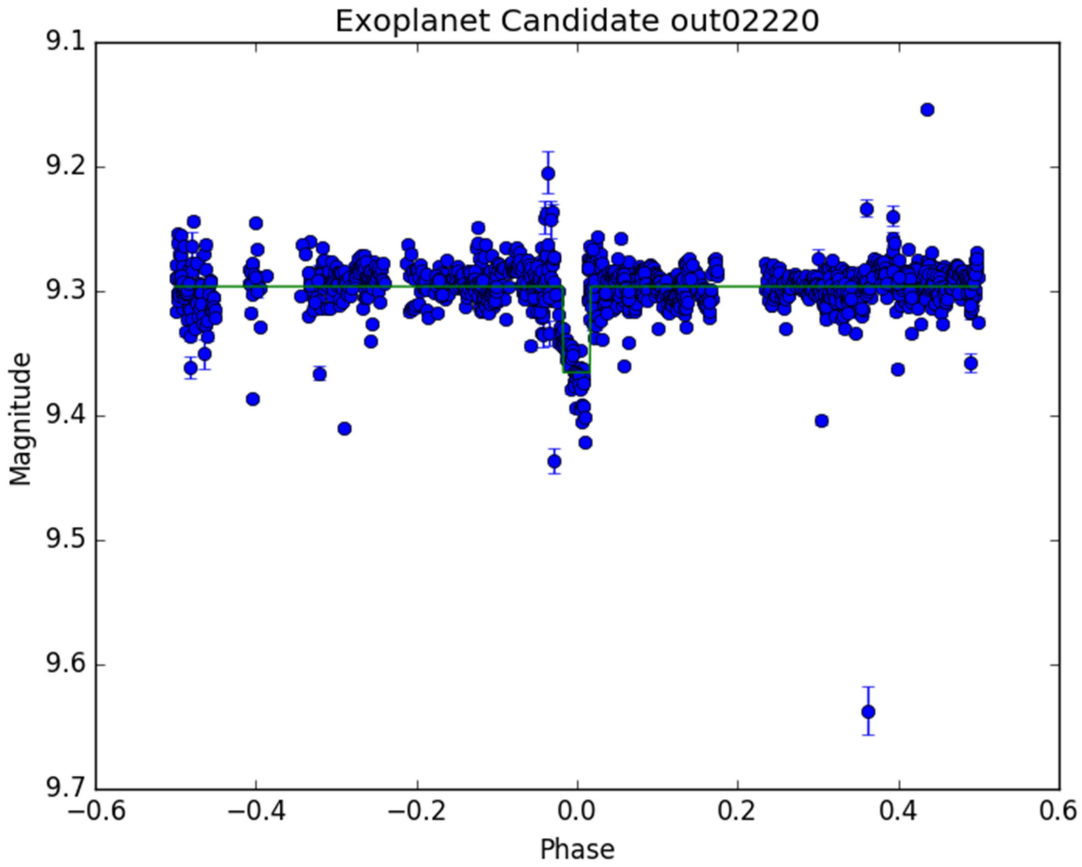

Figure 6-8 Northern exoplanet candidate with 2 transits.

Table 6-1 All statistically significant BLS categorizations from VARTOOLS

Southern Variables from VARTOOLS	Right Ascension Declination	VaST Magnitude	Estimated Magnitude	Average Standard Error	Period (days)	Transit Depth (Magnitude)
sout02872	19:26:24.701 +27:23:54:64	-10.3	13.56	0.0203	1.914	0.143
sout00628	19:26:37.877 +27:0.:33.02	-9.722	14.38	0.0255	2.767	0.238
sout20167	19:26:24.074 +23:23:49.81	-9.5	14.69	0.033	1.911	0.157
Northern Variables from VARTOOLS	Right Ascension Declination	VaST Magnitude	Estimated Magnitude	Average Standard Error	Period (days)	Transit Depth (Magnitude)
out00726	*22:13:09.989 +56:38:33.09	-13.080	9.626	0.003	0.711	0.126
out01576	22:14:35.964 +56:34:35.48	-12.940	9.824	0.003	2.246	0.063
out02184	22:13:52.176 +56:32:09.57	-10.000	13.982	0.026	1.494	0.095
out02188	22:15:06.247 +56:31:42.76	-11.510	11.847	0.009	2.811	0.121
out02335	22:15:26.309 +56:30:45.84	-13.600	8.890	0.002	2.810	0.122
out02336	22:15:19.941 +56:30:56.69	-10.700	12.992	0.012	2.810	0.159
out02365	22:15:31.136 +56:30:34.93	-13.190	9.470	0.003	2.810	0.132
out02368	22:14:59.781 +56:30:42.56	-12.070	11.054	0.006	2.800	0.058
out02400	22:15:06.631 +56:30:45.37	-10.500	13.275	0.019	2.810	0.132
out02661	22:15:45.927 +56:29:19.86	-9.600	14.548	0.036	1.900	0.314
out03038	22:15:43.720 +56:27:10.36	-12.500	10.446	0.004	2.233	0.117
out03120	22:14:20.154 +:56:27:20.09	-9.520	14.661	0.046	1.440	0.101
out03145	22:15:37.023 +56:26:46.39	-11.800	11.436	0.007	1.850	0.110
out03225	22:15:29.731 +56:26:22.64	-11.970	11.196	0.006	5.150	0.088
out03277	22:15:22.833 +56:26:05.87	-12.000	11.153	0.006	3.860	0.075
out03365	22:15:25.103 +56:25:40.43	-10.600	13.134	0.017	2.380	0.091
out03433	22:15:24.797 +56:25:20.40	-10.880	12.738	0.014	3.860	0.074
out04128	22:12:42.556 +56:22:11.04	-9.530	14.647	0.035	1.330	0.231
out04181	22:14:24.903 +56:21:32.17	-10.410	13.402	0.021	2.840	0.121
out04182	22:15:53.623 +56:21:06.33	-11.300	12.144	0.010	2.970	0.166
out04273	22:13:54.230 +56:21:12.69	-10.250	13.629	0.023	3.060	0.102
out04706	22:13:26.664 +56:12:35.59	-10.300	13.558	0.023	3.080	0.130
out05030	22:14:53.144 +56:16:38.23	-9.480	14.718	0.048	2.250	0.447

Table 6-2 Statistically significant exoplanet candidates from VARTOOLS

Northern Exoplanet Candidates:	Right Ascension Declination	VaST Magnitude	Estimated Magnitude	Average Standard Error	Period (days)	Transit Depth (Magnitude)	Time of Mid-Transit (2457300) JD
out02220	22:14:41.808 +56:31:27.96	-13.300	9.315	0.002	2.810	0.049	4.81924381
out02530	22:14:45.848 +56:29:52.91	-13.600	8.890	0.002	2.380	0.038	5.77027225
out02588	22:14:48.302 +56:29:47.40	-11.270	12.186	0.011	2.570	0.048	4.10397867
out02679	22:13:57.688 +56:29:07.35	-11.861	11.350	0.002	5.510	0.014	4.83101756
out02849	22:14:54.307 +56:28:25.16	-11.300	12.144	0.010	1.290	0.047	4.08820093

Chapter 7

Results

The initial purpose of this study was to show the connection between exoplanet incidence and galactocentric distance. Since the southern field contains more stars at a smaller galactocentric distance in comparison to the northern field, it was expected that more exoplanets would be found in the southern field. The southern field only contained three statistically significant candidates, while the northern field contained twenty-eight statistically significant candidates. Of all of these potential candidates, only five from the northern field had transit depths of less than 0.05 magnitudes. These candidates can be found in the northern exoplanet catalog (Table 6.2) under the following identification names: out02220 with a transit depth of 0.049 magnitudes, out02530 with a transit depth of 0.038 magnitudes, out02588 with a transit depth of 0.048 magnitudes, out02679 with a transit depth of 0.014 magnitudes, and out02849 with a transit depth of 0.047 magnitudes. Due to the depth of the transits and multiple transit detections, these five candidates are our highest quality exoplanet candidates. The other twenty-three candidates from the northern field and the three candidates from the southern field are more than likely eclipsing binaries due to their large transit depths.

One of the potential reasons why there were fewer exoplanet candidates in the southern field was that the number of images used for photometry was smaller than the number used for the northern field. The amount of time observing each field was evenly split. Unfortunately, the southern field had around ninety images that were streaked due to either wind moving the telescope during exposures or telescope tracking issues. Because of this, those images were removed. This set the number of images used by VaST for the southern field to 1627 compared to the 1711 images used for the northern field. While this is only a five percent difference, VaST

automatically excludes images that are not good enough for photometry. This created a larger difference in the number of images actually used in the final analysis, 1281 for the southern field and 1608 for the northern field. This corresponds to a twenty two percent difference in the number of images used. Therefore, the average number of data points in each field's light curves are significantly different. The mean measurements per object for the southern field was 86.7 while the northern value was 115.1.

While this numerical measurement discrepancy does alter the statistical expectation of exoplanet detection, there is more than likely another reason for the lower result. The number of stars in the southern field is 1.37 times more than the northern field. The southern field images contained an average of 6268.53 matching variable stars while the northern field images contained an average of 4456.23 matching variable stars. This shows that the southern field is more crowded, which is to be expected. Using PSF photometry should allow for crowded fields to be analyzed, but the method does have limitations. The main limitation is excessive crowding, but since PSF photometry has been successfully used on globular clusters, so it is expected that it would be successful in this study (Heasley 1999).

The absence of exoplanet candidate detections in the southern field could also be due to observational noise from sky background, light pollution, or non-resolved stars. The mean number of counts per pixel of thirty images used for photometry were compared; fifteen from each field. The median count for the northern field was 288.4 counts per pixel, while the southern median count was 476.5. These values correspond to the sky background for each field. Due to the significantly larger sky background for the southern field, the error in the southern data was considerably higher. If a star in the southern field had a transit depth that was less than 0.05 magnitudes and was dimmer than 13 magnitude, the signal would be statistically

insignificant. Another possible reason for the large amount of noise in the southern field could be due to the variable transparency of the atmosphere. The opacity of the Earth's atmosphere varies at different locations at different times. This should be mostly accounted for by the algorithm used within VaST for differential photometry, since VaST uses stars that are close to the target star for comparison.

Since there were no exoplanets detected in the southern field, a statistical comparison relating exoplanet incidence and the metallicity gradient of the galaxy in not possible for this study. The data pipeline did prove to be effective for discovering new short period variable stars and exoplanet candidates, which shows that further implementations of this pipeline would be useful for future surveys.

A potential way to improve the chances of success of this project, or other projects like it in the future, would be to alter the data acquisition process. The 20-inch telescope could potentially need a tracking improvement. The light pollution from the city of Muncie could also be removed from the equation if the observatory was not on campus. One of the darkest skies in Indiana is approximately thirty miles east of Muncie near New Pittsburg according to the Dark Site Finder website. If moving a telescope to a new location is not possible, Ball State University has access to off-campus telescopes managed by the Southeastern Association for Research and Astronomy (SARA). The usage of the SARA telescopes would increase the quality of the data, but there may be limitations on the quantity of data obtainable due to scheduling. The SARA telescopes available also have much smaller fields of view, which decreases their usefulness for surveys.

Chapter 8

Conclusion

The data acquisition process described in Chapter 2 provided several nights of data that should have allowed for the comparison of two different fields that contained stars at different galactocentric distances. All of the acquired data were reduced and analyzed used the software and methods described in Chapters 3 and 4.

Several new variable stars were discovered through the usage of UPSILON. None of these stars were previously cataloged on SIMBAD. Multiple variable candidates were confirmed using the *Peranso* period analysis software. These new variable stars are cataloged at the end of Chapter 5.

Five new exoplanet candidates were also discovered. The usage of VARTOOLS and the BLS method provided a total of thirty-one potential exoplanet candidates, five of which have transit depths that pertain to the transit of an exoplanet. All of these are cataloged at the end of Chapter 6. The other twenty-six candidates were determined to not be exoplanets due to the size of their transit depths. No conclusions can be made about the comparison of exoplanet incidence and galactocentric distance, since exoplanets candidates were only detected in one field. The data analysis pipeline used was determined to be effective in detecting variable stars and exoplanets and would be useful for future surveys at Ball State.

References

Duffett-Smith, P. (1992). Galactic Coordinates, Equatorial to Galactic Coordinate Conversion, and Galactic to Equatorial Coordinate Conversion. §20, 29, and 30 in Practical Astronomy with Your Calculator, 3rd ed. Cambridge, England: Cambridge University Press, 32, 43, and 44.

Birney, D. S., Gonzalez, G., & Oesper, D. (2006). Observational Astronomy. New York, N. Y.: Cambridge University Press.

Burandov et al. (2016), First results of the Kourovka Planet Search: Discovery of Transiting Exoplanet Candidates in the First Three Target Fields. MNRAS 461(4), 3854-3863

Cameron, A. (2016), Extrasolar Planetary Transits. Methods of Detecting Exoplanets, Astrophysics and Space Science Library, Volume 428. ISBN 978-3-319-27456-0. Springer International Publishing Switzerland, 2016, p. 89

Cheng, J., Rockosi, C., Morrison, H., Schönrich, R., Lee, Y., Beers, T., … Schneider, D. (2012). Metallicity Gradients In The Milky Way Disk As Observed By The Segue Survey. The Astrophysical Journal, 746, 149.

Fischer, D. & Valenti, J. (2005). The planet-metallicity correlation. ApJ, 622(2), 1102-1117.

Frinchaboy, P. M., Thompson, B., Jackson, K. M., O'Connell, J., Meyer, B., Zasowski, G., … Wilson, J. C. (2013). The open cluster chemical analysis and mapping survey: local galactic metallicity gradient with apogee. sdss dr10. ApJ, 777, 7.

G 232-63. (n.d.). SIMBAD. Centre de données astronomiques de Strasbourg.

Gonzalez, G. (1997). The stellar metallicity-giant planet connection. MNRAS, 285(2), 403-412.

Gonzalez, G. (2014). The metallicity dependence of giant planet incidence. MNRAS, 443(1), 393-397.

Hartman, J. & Bakos, G. (2016) VARTOOLS: A Program for Analyzing Astronomical Time-Series Data. Astronomy and Computing 17 (2016) 1–72.

Heasley. (1999). Point-Spread Function Fitting Photometry. Precision CCD Photometry, ASP Conference Series, Vol. 189.

Kim, D. & Bailer-Jones, C. (2015). A Package for the Automated Classification of Periodic Variable Stars. A&A Volume 587, A18.

Kindt. (2015). Harvesting Planets in the Inner and Outer Galaxy (Master's thesis). Ball State University. (Publication No. catkey/1808718).

Kochanek et al. (2017). The All-Sky Automated Survey for Supernovae (ASAS-SN) Light Curve Server v1.0. Publications of the Astronomical Society of the Pacific. 129, 980.

Kovács, G., Zucker, S., & Mazeh, T. (2002) A Box-fitting Algorithm in the Search for Periodic Transits. Astronomy and Astrophysics, v.391, p.369-377.

Li, A. (2006, October 21). Dust in Active Galactic Nuclei. Retrieved August 17, 2016, from https://ned.ipac.caltech.edu/level5/Sept07/Li2/Li2.html Nardiello 2016.

LSPM J 1926+ 2726 . (n.d.). SIMBAD. Centre de données astronomiques de Strasbourg.

Roman, N. G. (1987). Identification of a Constellation from a Position. Astron. Soc. Pac. 99, 695.

Sokolovsky, K. & Lebedev A. (2017) VaST: a variability search toolkit. eprint arXiv:1702.07715.

Tody, D. & Fitzpatrick, M. (1995). Linux/IRAF Installation Guide. Retrieved from ftp://iraf.noao.edu/iraf/web/docs/src/linux/linuxiraf-N-3.html.

VARTOOLS. (2015). The VARTOOLS Light Curve Analysis Program. Retrieved from http://www.astro.princeton.edu/~jhartman/vartools.html.

VaST developers team. (2015). VaST [Variability Search Toolkit]. Retrieved from http://scan.sai.msu.ru/vast/

Wenger M. et al. (1999). The SIMBAD astronomical database. A&A Volume 143, Number 1, April I 2000.

Appendix A (data acquisition script)

```
; This plan was generated by ACP Planner 4.2.6
; -----------------------------------------
;
; For:          User
; Targets:      1
;
; NOTE:         Timing features are disabled
;
; Autofocus at start of run.
;
; -----------------------------------------------
;
#dir C:\Gonzalez    ; Images forced to go into this folder
#duskflats GG_init-flats.txt  ; Acquire flat fields at dusk
;
;
; === Target Dark (10x180sec@bin2) ===
;
#repeat 1
#count 10
#interval 180
#binning 1
#dark
;
; === Target Bias (10@bin1) ===
;
#repeat 1
#count 10
#interval 0
#binning 1
#bias
;
;
#autofocus
;
; === Target Cyg_S1a ===
;
#repeat 10
#count 1
#filter NIR/Empty
#interval 180
#binning 1
Cyg_S1a             19:26:40.00         27° 11' 15.0"
;
;
; === Target Cyg_S1b ===
;
#repeat 10
#count 1
#filter NIR/Empty
#interval 180
#binning 1
Cyg_S1b             19:26:40.00         27° 11' 15.1"
;
```

```
;
; === Target Cyg_S1c ===
;
#repeat 10
#count 1
#filter NIR/Empty
#interval 180
#binning 1
Cyg_S1c             19:26:40.00         27° 11' 15.2"
;
;
;
#shutdown ; Set to UT of sunrise
; -----------
; END OF PLAN
; -----------
;
```

Appendix B (flat script)

```
;
; -----------------------------------------------
; ACP Auto-Flat Plan - Generated by ACP Planner
; -----------------------------------------------
;
; For:      User
; At:       20:26:49
; From:     GG_Cyg.txt
; Flats:    10
;
; Lines are count,filter,binning (comma-separated)
; Empty filter uses ACP-configured clear filter
; -----------------------------------------------------
;
10,NIR/Empty,1
;
; ----------------
; END OF FLAT PLAN
; ----------------
;
```

Appendix C (pixel mask example)

1075 1075 2927 2924

2076 2076 2855 2855

3974 3974 3803 3805

4029 4030 3915 3916

1106 1107 2912 2917

3223 3224 3677 3678

4006 4007 3792 3793

4061 4061 3904 3904

131 132 1476 1477

382 383 670 671

Appendix D (ccdrpoc example)

```
                                IRAF
                  Image Reduction and Analysis Facility
PACKAGE = ccdred
   TASK = ccdproc

images  =         @imglist.txt  List of CCD images to correct
(output =                      ) List of output CCD images
(ccdtype=                      ) CCD image type to correct
(max_cac=                    0) Maximum image caching memory (in Mbytes)
(noproc =                   no) List processing steps only?

(fixpix =                  yes) Fix bad CCD lines and columns?
(oversca=                  yes) Apply overscan strip correction?
(trim   =                  yes) Trim the image?
(zerocor=                  yes) Apply zero level correction?
(darkcor=                  yes) Apply dark count correction?
(flatcor=                  yes) Apply flat field correction?
(illumco=                   no) Apply illumination correction?
(fringec=                   no) Apply fringe correction?
(readcor=                   no) Convert zero level image to readout correction?
(scancor=                   no) Convert flat field image to scan correction?

(readaxi=                 line) Read out axis (column|line)
(fixfile=        pixelmask.txt) File describing the bad lines and columns
(biassec=  [4150:4232,52:4117]) Overscan strip image section
(trimsec=    [60:4125,52:4117]) Trim data section
(zero   =         Zero1_17.fts) Zero level calibration image
(dark   =         Dark1_17.fts) Dark count calibration image
(flat   =         Flat2_17.fts) Flat field images
(illum  =                      ) Illumination correction images
(fringe =                      ) Fringe correction images
(minrepl=                  1.) Minimum flat field value
(scantyp=           shortscan) Scan type (shortscan|longscan)
(nscan  =                   1) Number of short scan lines

(interac=                  no) Fit overscan interactively?
(functio=            legendre) Fitting function
(order  =                   6) Number of polynomial terms or spline pieces
(sample =                   *) Sample points to fit
(naverag=                   1) Number of sample points to combine
(niterat=                   1) Number of rejection iterations
(low_rej=                  3.) Low sigma rejection factor
(high_re=                  3.) High sigma rejection factor
(grow   =                  0.) Rejection growing radius
(mode   =                  ql)
```

Appendix E (zerocombine example)

```
                                  I R A F
                     Image Reduction and Analysis Facility
PACKAGE = ccdred
   TASK = zerocombine

input   =        @biaslist.txt  List of zero level images to combine
(output =            Zero1.fts) Output zero level name
(combine=               median) Type of combine operation
(reject =               minmax) Type of rejection
(ccdtype=                     ) CCD image type to combine
(process=                  yes) Process images before combining?
(delete =                   no) Delete input images after combining?
(clobber=                   no) Clobber existing output image?
(scale  =                 none) Image scaling
(statsec=                     ) Image section for computing statistics
(nlow   =                    0) minmax: Number of low pixels to reject
(nhigh  =                    1) minmax: Number of high pixels to reject
(nkeep  =                    1) Minimum to keep (pos) or maximum to reject (neg)
(mclip  =                  yes) Use median in sigma clipping algorithms?
(lsigma =                   3.) Lower sigma clipping factor
(hsigma =                   3.) Upper sigma clipping factor
(rdnoise=                   0.) ccdclip: CCD readout noise (electrons)
(gain   =                   1.) ccdclip: CCD gain (electrons/DN)
(snoise =                   0.) ccdclip: Sensitivity noise (fraction)
(pclip  =                 -0.5) pclip: Percentile clipping parameter
(blank  =                   0.) Value if there are no pixels
(mode   =                   ql)
```

Appendix F (darkcombine example)

```
                                  I R A F
                     Image Reduction and Analysis Facility
PACKAGE = ccdred
   TASK = darkcombine

input   =        @darklist.txt  List of dark images to combine
(output =            Dark1.fts) Output dark image root name
(combine=              average) Type of combine operation
(reject =               minmax) Type of rejection
(ccdtype=                     ) CCD image type to combine
(process=                  yes) Process images before combining?
(delete =                   no) Delete input images after combining?
(clobber=                   no) Clobber existing output image?
(scale  =             exposure) Image scaling
(statsec=                     ) Image section for computing statistics
(nlow   =                    0) minmax: Number of low pixels to reject
(nhigh  =                    1) minmax: Number of high pixels to reject
(nkeep  =                    1) Minimum to keep (pos) or maximum to reject (neg)
(mclip  =                  yes) Use median in sigma clipping algorithms?
(lsigma =                   3.) Lower sigma clipping factor
(hsigma =                   3.) Upper sigma clipping factor
(rdnoise=                   0.) ccdclip: CCD readout noise (electrons)
(gain   =                   1.) ccdclip: CCD gain (electrons/DN)
(snoise =                   0.) ccdclip: Sensitivity noise (fraction)
(pclip  =                 -0.5) pclip: Percentile clipping parameter
(blank  =                   0.) Value if there are no pixels
(mode   =                   ql)
```

Appendix G (flatcombine example)

```
                                  IRAF
                  Image Reduction and Analysis Facility
PACKAGE = ccdred
   TASK = flatcombine

input   =       @flatlist.txt  List of flat field images to combine
(output =           Flat1.fts) Output flat field root name
(combine=             average) Type of combine operation
(reject =           avsigclip) Type of rejection
(ccdtype=                    ) CCD image type to combine
(process=                 yes) Process images before combining?
(subsets=                 yes) Combine images by subset parameter?
(delete =                  no) Delete input images after combining?
(clobber=                  no) Clobber existing output image?
(scale  =                mode) Image scaling
(statsec=                    ) Image section for computing statistics
(nlow   =                   1) minmax: Number of low pixels to reject
(nhigh  =                   1) minmax: Number of high pixels to reject
(nkeep  =                   1) Minimum to keep (pos) or maximum to reject (neg)
(mclip  =                 yes) Use median in sigma clipping algorithms?
(lsigma =                  3.) Lower sigma clipping factor
(hsigma =                  3.) Upper sigma clipping factor
(rdnoise=                  0.) ccdclip: CCD readout noise (electrons)
(gain   =                  1.) ccdclip: CCD gain (electrons/DN)
(snoise =                  0.) ccdclip: Sensitivity noise (fraction)
(pclip  =                -0.5) pclip: Percentile clipping parameter
(blank  =                  1.) Value if there are no pixels
(mode   =                  ql)
```

Appendix H (VARTOOLS BLS sample output)

```
Name                          = out02849.dat
BLS_Period_1_0                =     1.28737480
BLS_Tc_1_0                    = 2457304.0882009361
BLS_SN_1_0                    =   4.00164
BLS_SR_1_0                    =   0.00785
BLS_SDE_1_0                   =   3.98231
BLS_Depth_1_0                 =   0.04656
BLS_Qtran_1_0                 =   0.05200
BLS_i1_1_0                    =   0.28600
BLS_i2_1_0                    =   0.33600
BLS_deltaChi2_1_0             = -874.17631
BLS_fraconenight_1_0          =   0.44840
BLS_Npointsintransit_1_0      =    44
BLS_Ntransits_1_0             =     4
BLS_Npointsbeforetransit_1_0 =    69
BLS_Npointsaftertransit_1_0  =    64
BLS_Rednoise_1_0              =   0.00385
BLS_Whitenoise_1_0            =   0.01974
BLS_SignaltoPinknoise_1_0     =  13.13879
BLS_Period_2_0                =     2.57491401
BLS_Tc_2_0                    = 2457304.0727771018
BLS_SN_2_0                    =   3.98169
BLS_SR_2_0                    =   0.00783
BLS_SDE_2_0                   =   3.96239
BLS_Depth_2_0                 =   0.03971
BLS_Qtran_2_0                 =   0.03200
BLS_i1_2_0                    =   0.13400
BLS_i2_2_0                    =   0.16400
BLS_deltaChi2_2_0             = -869.38919
BLS_fraconenight_2_0          =   0.44193
BLS_Npointsintransit_2_0      =    59
BLS_Ntransits_2_0             =     4
BLS_Npointsbeforetransit_2_0 =    51
BLS_Npointsaftertransit_2_0  =    58
BLS_Rednoise_2_0              =   0.00373
BLS_Whitenoise_2_0            =   0.01976
BLS_SignaltoPinknoise_2_0     =  12.49658
BLS_Period_3_0                =     1.81663106
BLS_Tc_3_0                    = 2457304.8382840925
BLS_SN_3_0                    =   3.97457
BLS_SR_3_0                    =   0.00783
BLS_SDE_3_0                   =   3.95527
BLS_Depth_3_0                 =   0.04648
BLS_Qtran_3_0                 =   0.04400
BLS_i1_3_0                    =   0.61200
BLS_i2_3_0                    =   0.65400
BLS_deltaChi2_3_0             = -867.68228
BLS_fraconenight_3_0          =   0.47892
BLS_Npointsintransit_3_0      =    44
BLS_Ntransits_3_0             =     3
BLS_Npointsbeforetransit_3_0 =    43
BLS_Npointsaftertransit_3_0  =    78
BLS_Rednoise_3_0              =   0.00392
BLS_Whitenoise_3_0            =   0.01977
```

```
BLS_SignaltoPinknoise_3_0    =  12.41750
BLS_Period_4_0               =     2.57478207
BLS_Tc_4_0                   = 2457304.0882060039
BLS_SN_4_0                   =   3.95996
BLS_SR_4_0                   =   0.00781
BLS_SDE_4_0                  =   3.94069
BLS_Depth_4_0                =   0.04425
BLS_Qtran_4_0                =   0.02800
BLS_i1_4_0                   =   0.14200
BLS_i2_4_0                   =   0.16800
BLS_deltaChi2_4_0            = -864.18939
BLS_fraconenight_4_0         =   0.45200
BLS_Npointsintransit_4_0     =    48
BLS_Ntransits_4_0            =     4
BLS_Npointsbeforetransit_4_0 =    52
BLS_Npointsaftertransit_4_0  =    53
BLS_Rednoise_4_0             =   0.00371
BLS_Whitenoise_4_0           =   0.01977
BLS_SignaltoPinknoise_4_0    =  13.00178
BLS_Period_5_0               =     2.37698900
BLS_Tc_5_0                   = 2457305.6380479652
BLS_SN_5_0                   =   3.63715
BLS_SR_5_0                   =   0.00746
BLS_SDE_5_0                  =   3.61821
BLS_Depth_5_0                =   0.04206
BLS_Qtran_5_0                =   0.03400
BLS_i1_5_0                   =   0.80400
BLS_i2_5_0                   =   0.83600
BLS_deltaChi2_5_0            = -788.76509
BLS_fraconenight_5_0         =   0.60618
BLS_Npointsintransit_5_0     =    50
BLS_Ntransits_5_0            =     2
BLS_Npointsbeforetransit_5_0 =    30
BLS_Npointsaftertransit_5_0  =    65
BLS_Rednoise_5_0             =   0.00408
BLS_Whitenoise_5_0           =   0.01981
BLS_SignaltoPinknoise_5_0    =  10.46384
BLS_Period_invtransit_0      =     0.83209689
BLS_deltaChi2_invtransit_0   = -211.98413
BLS_MeanMag_0                = -11.28536
```

Appendix I (Star finding images for all variable stars)

North is upwards, East is to the left, images are approximately 3 arcminutes by 3 arcminutes

Northern Variables

out01114

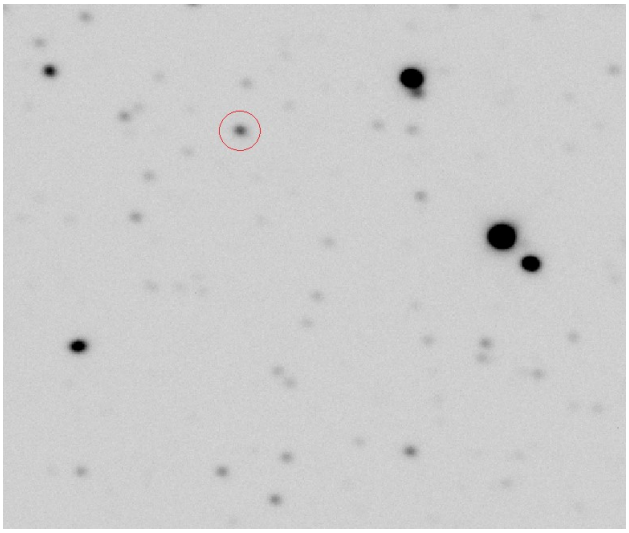

out01576

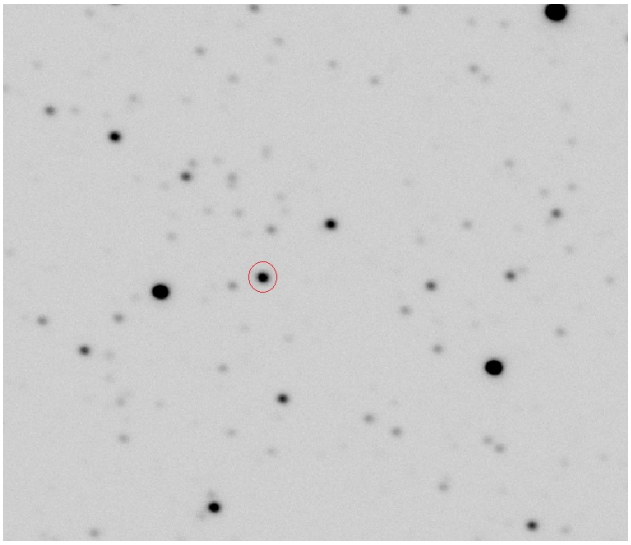

out03145

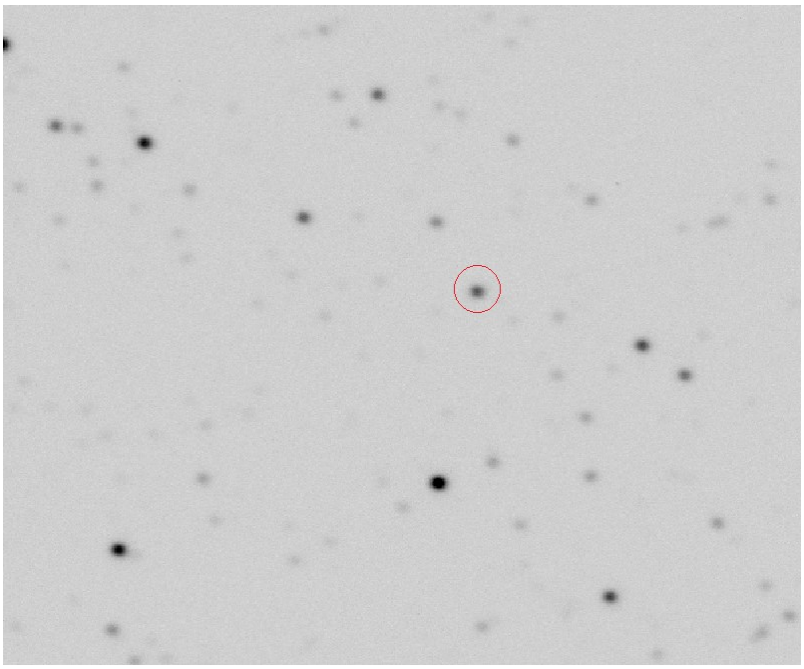

out 03038

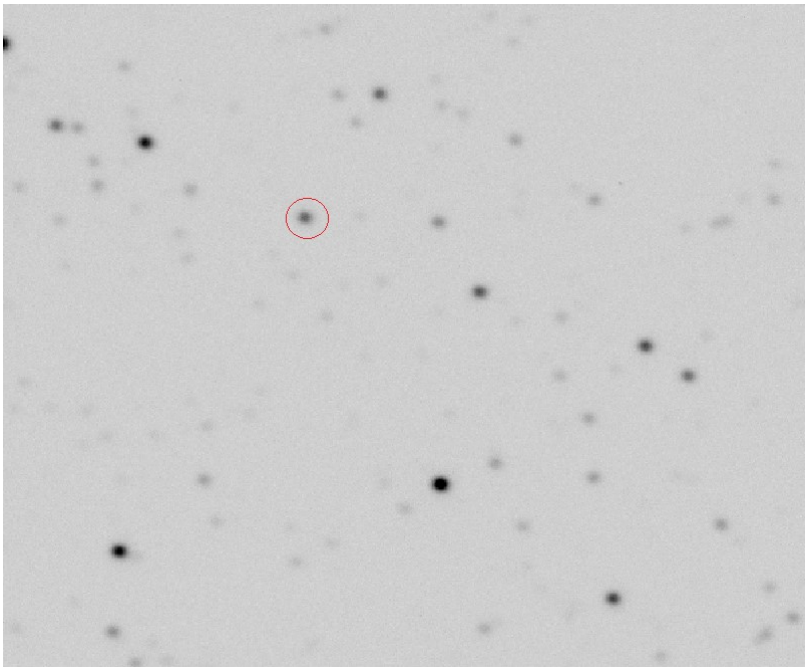

out03120

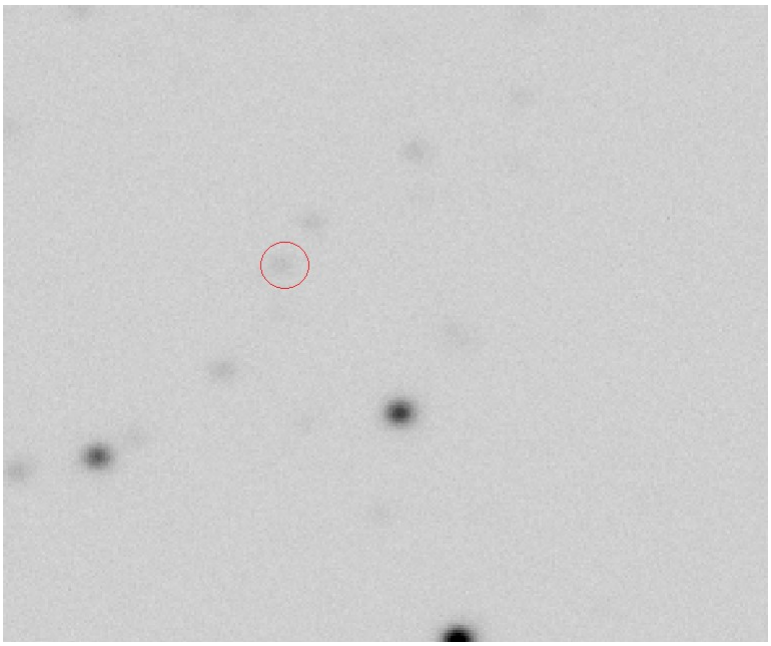

out03038

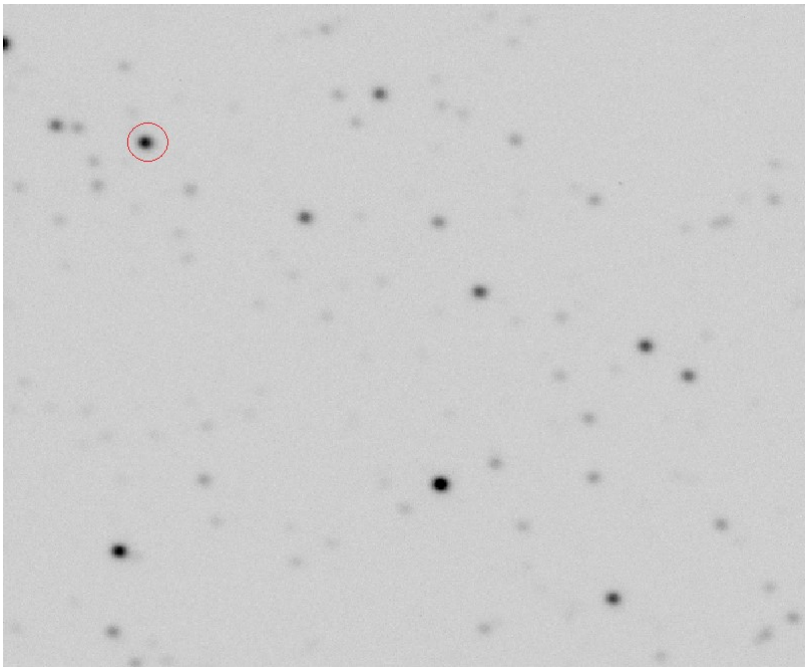

out03005

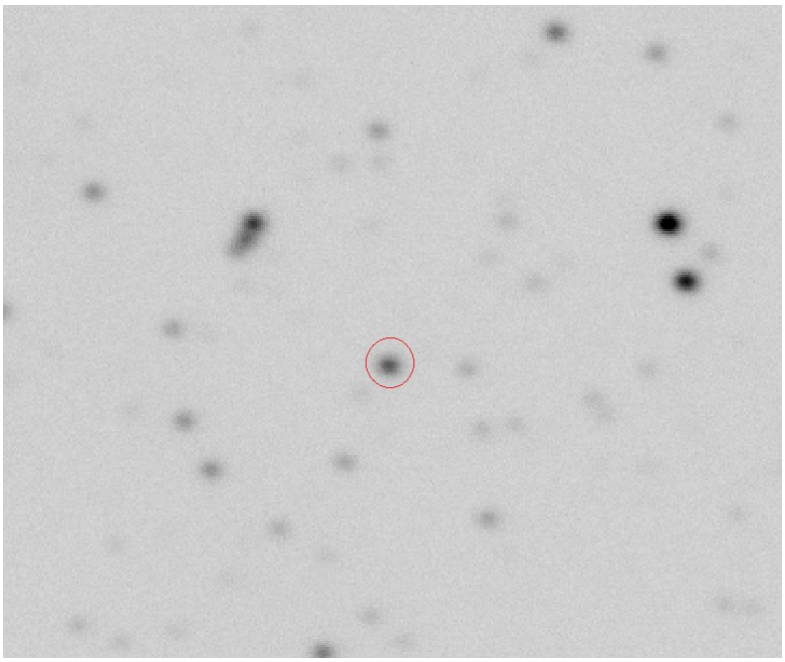

out02849

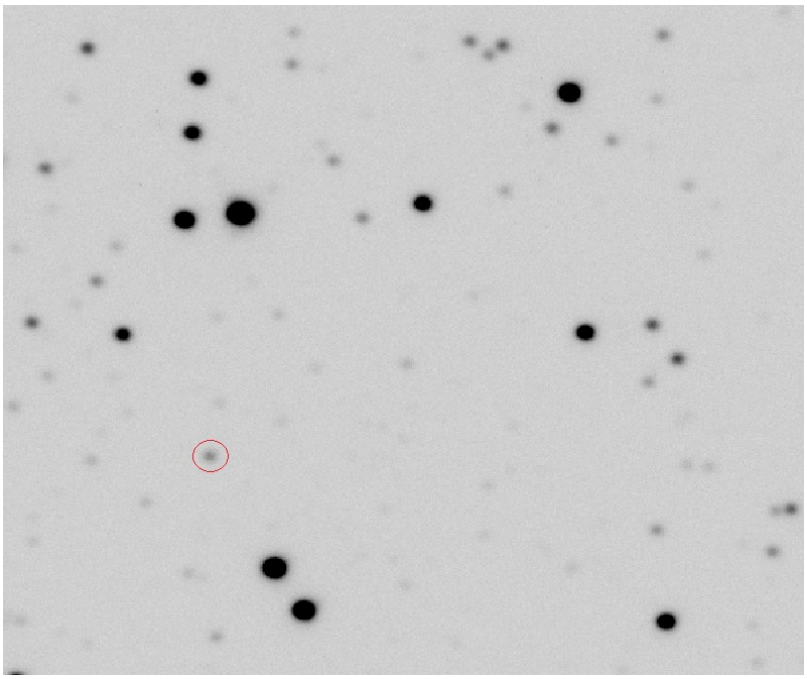

out02697

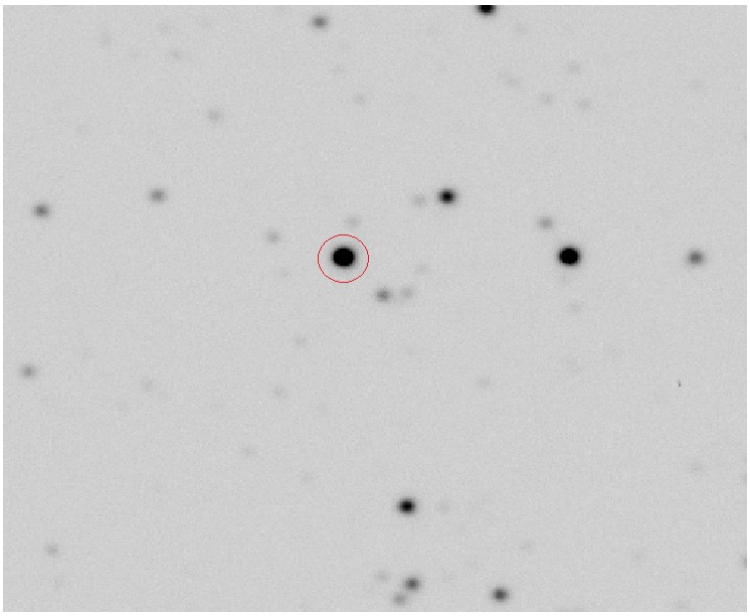

out02588

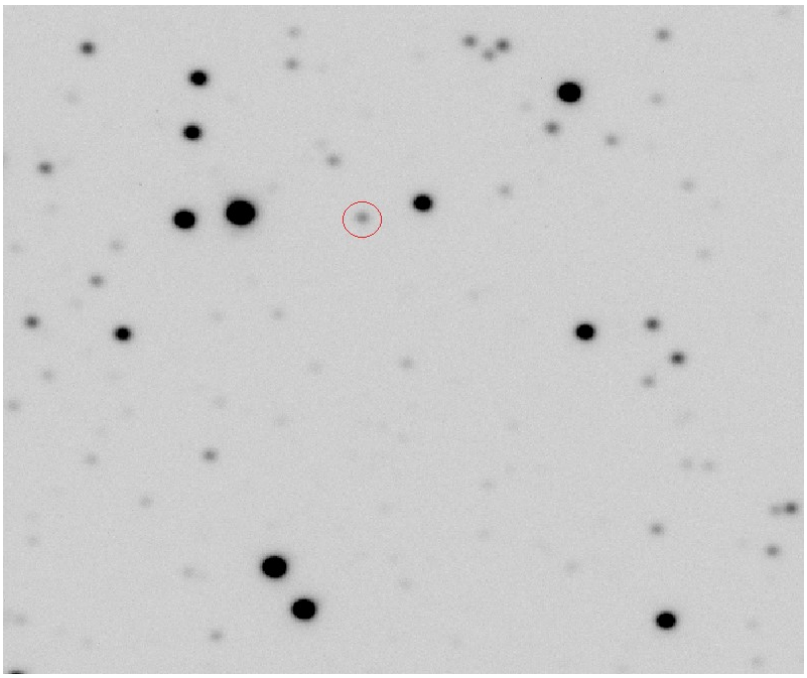

out02530

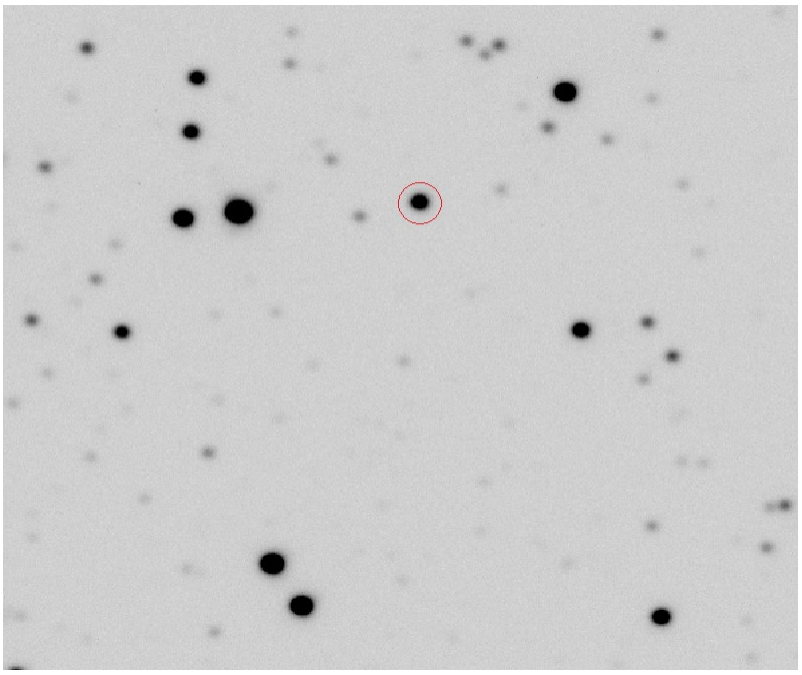

out02400

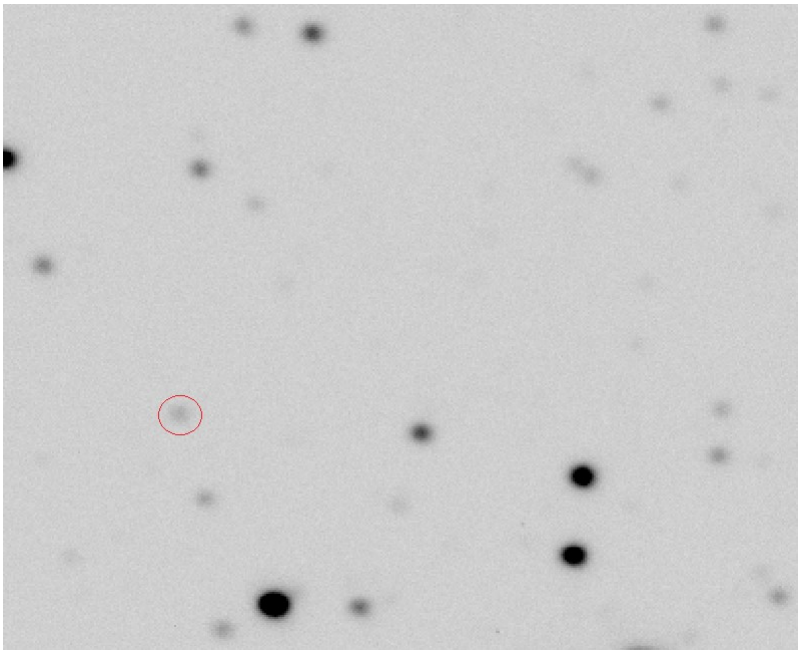

out02368

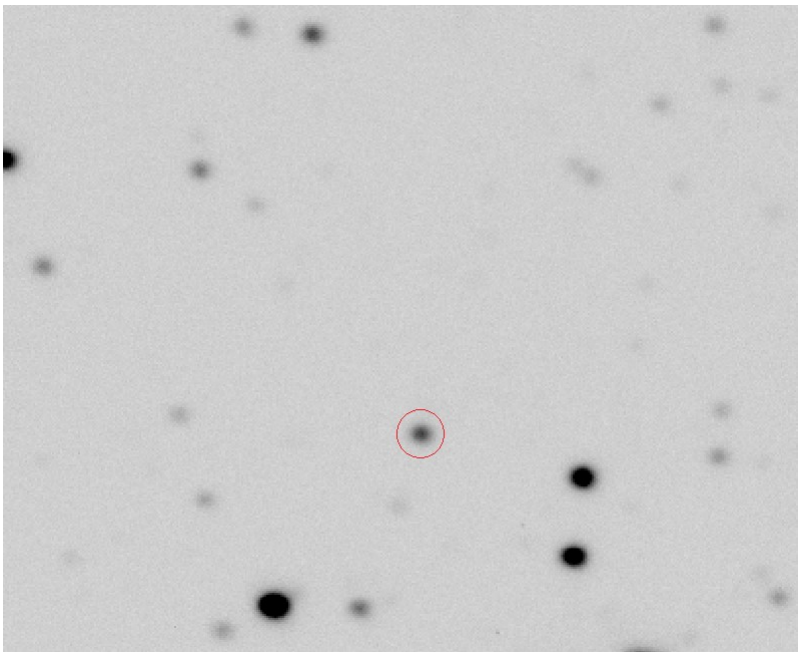

out02365

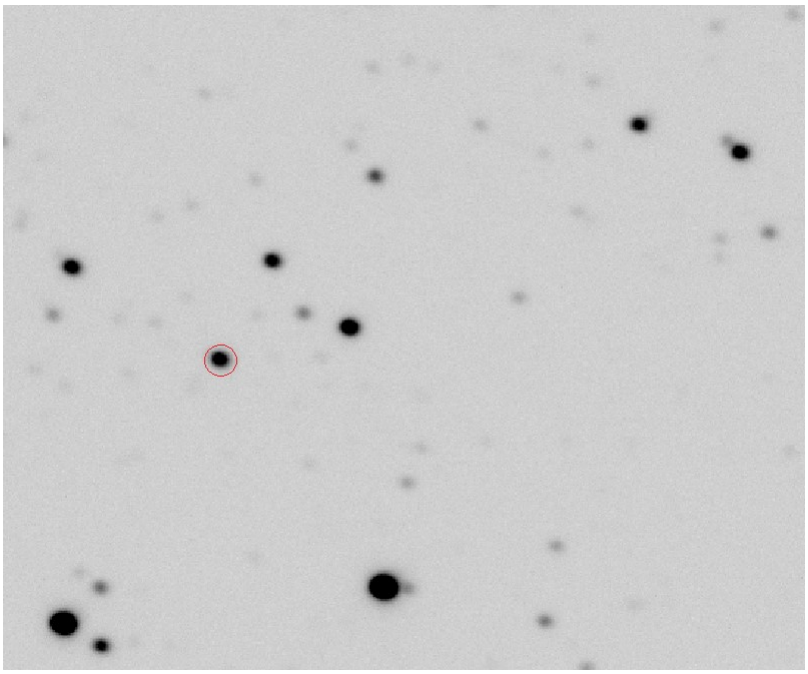

out02336

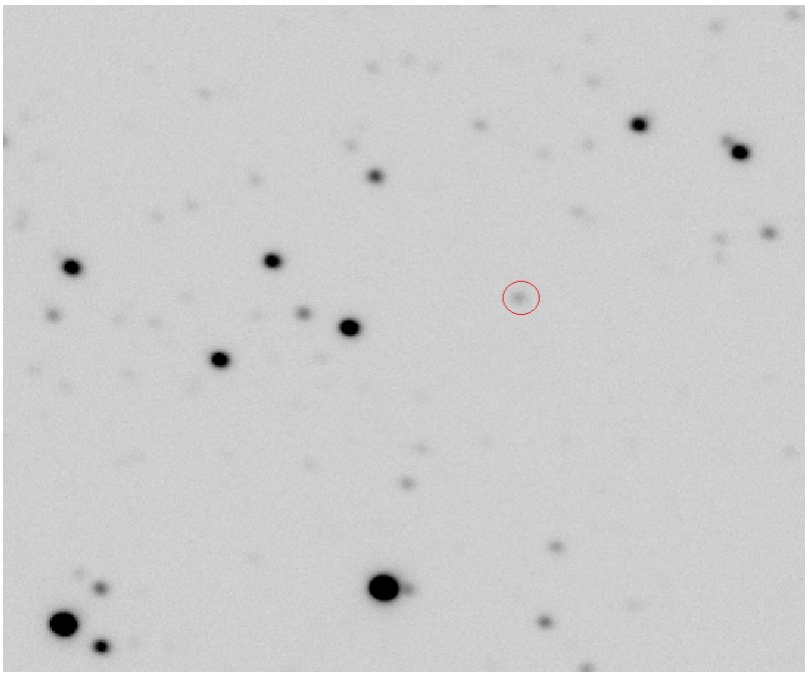

out02335

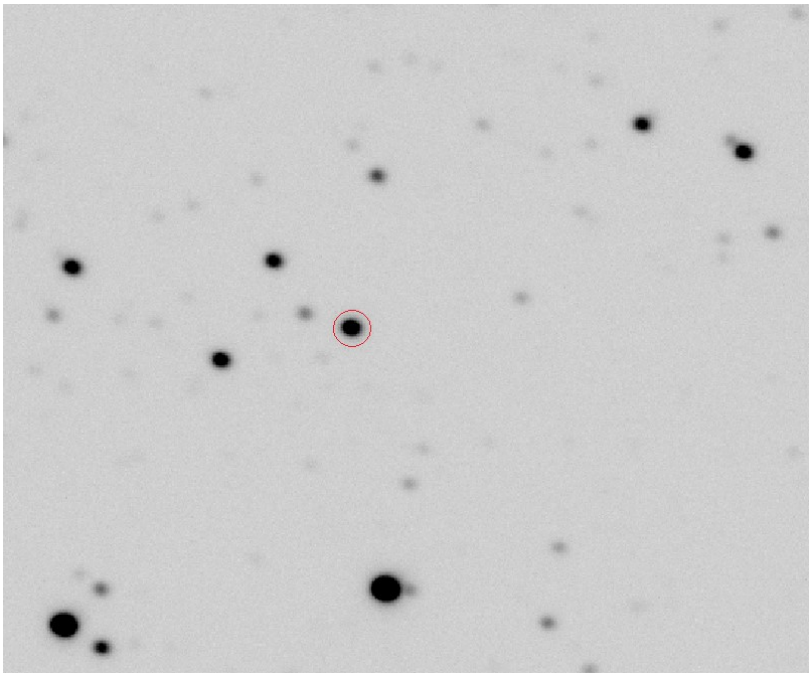

out02220

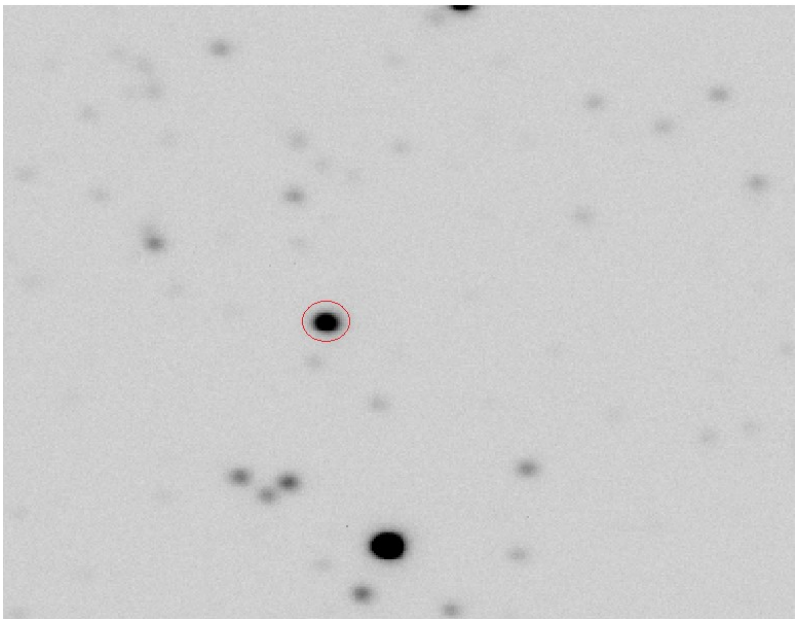

out02210

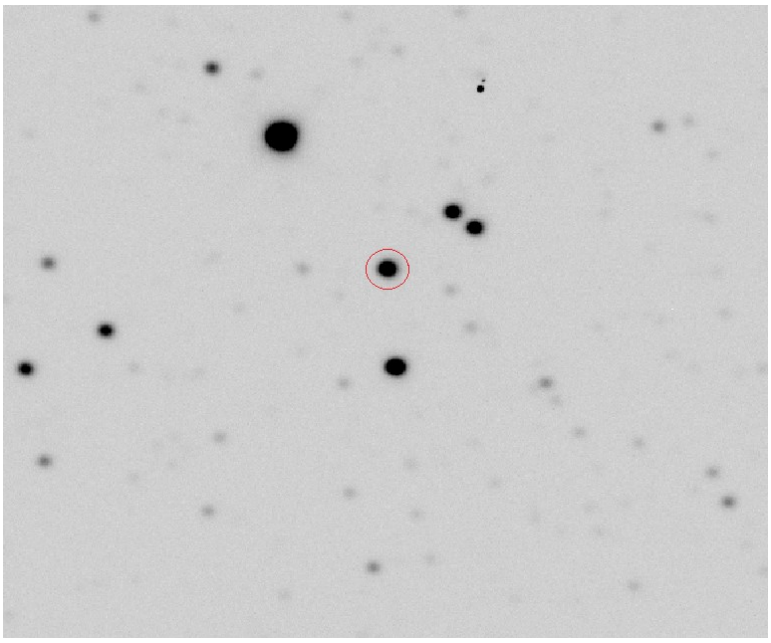

out02188

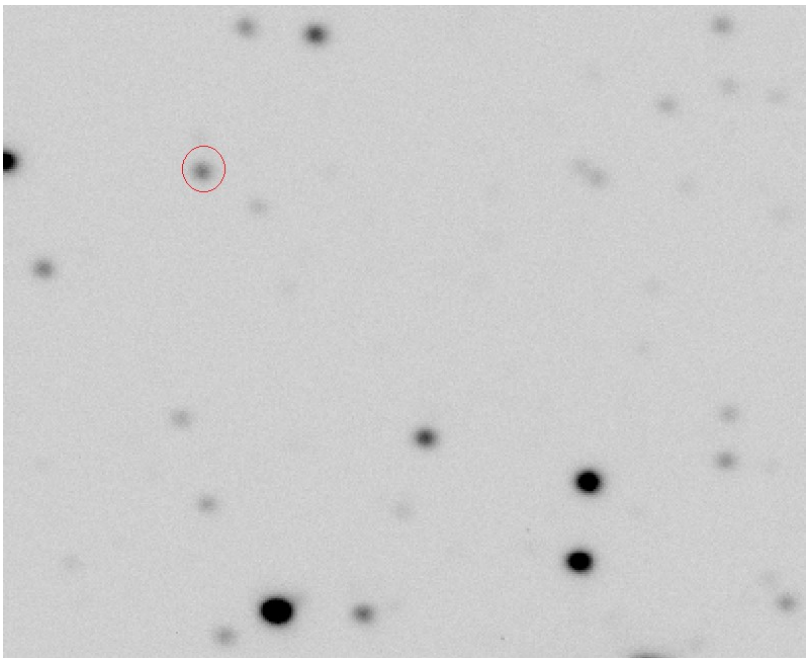

out02184

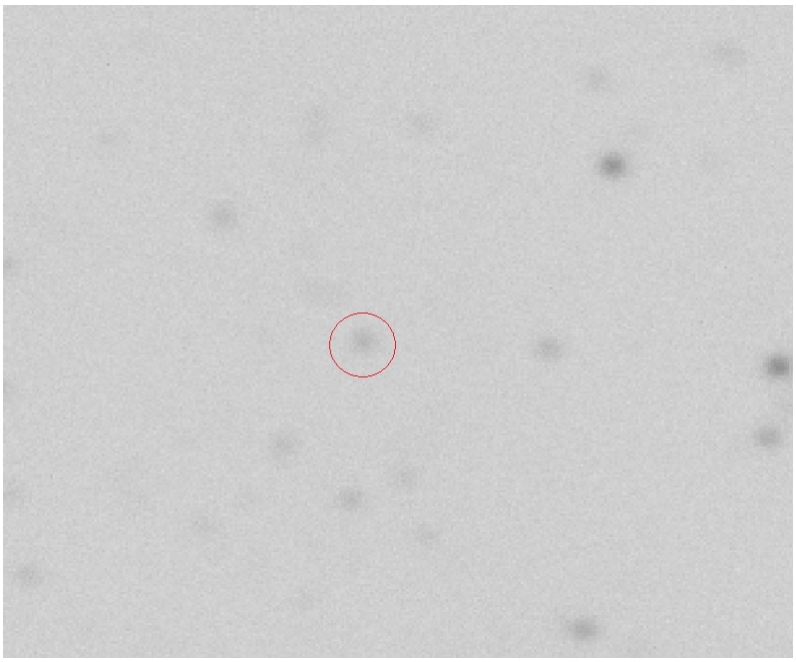

out01737

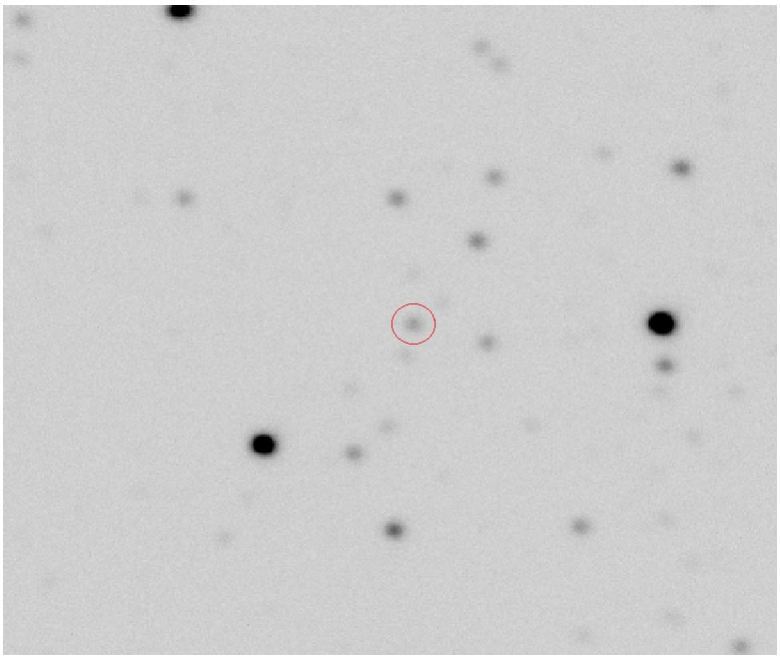

out22093

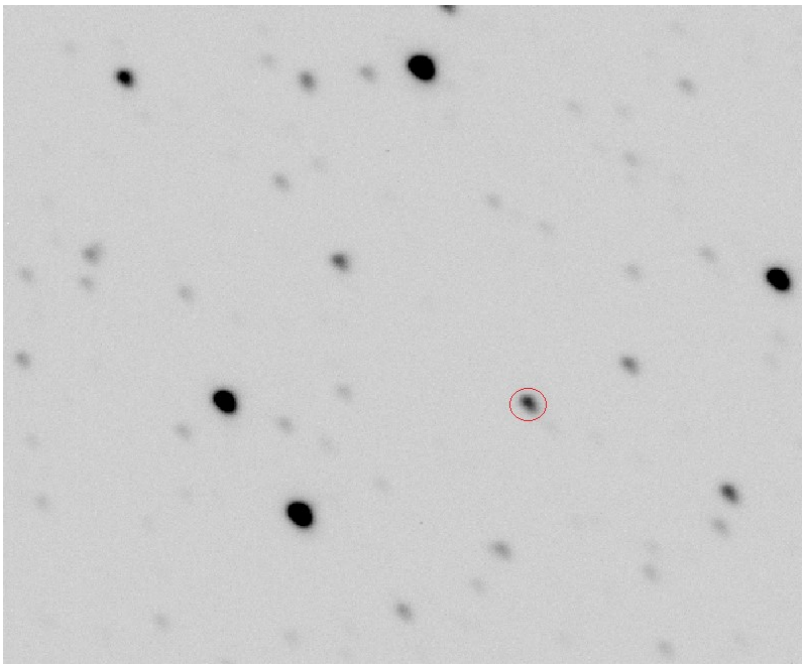

out20142

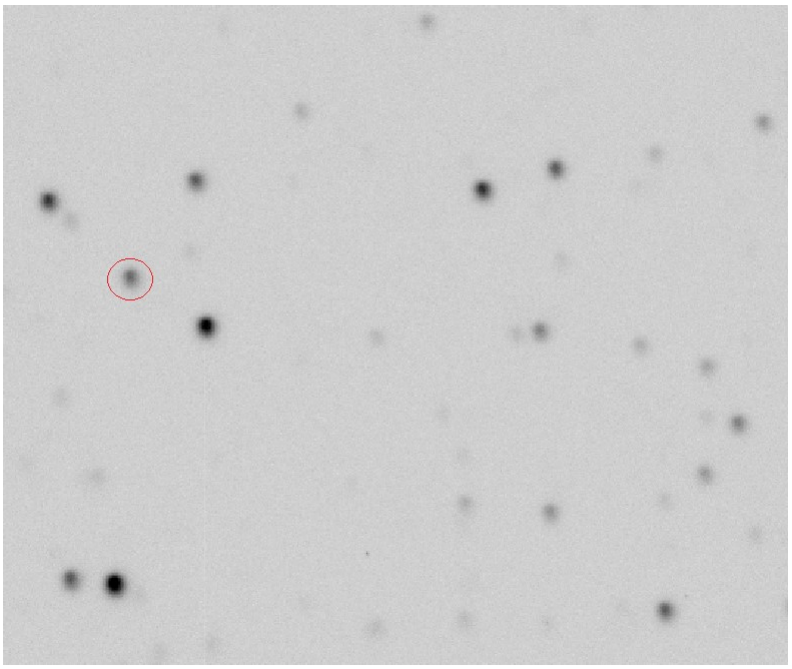

out06023

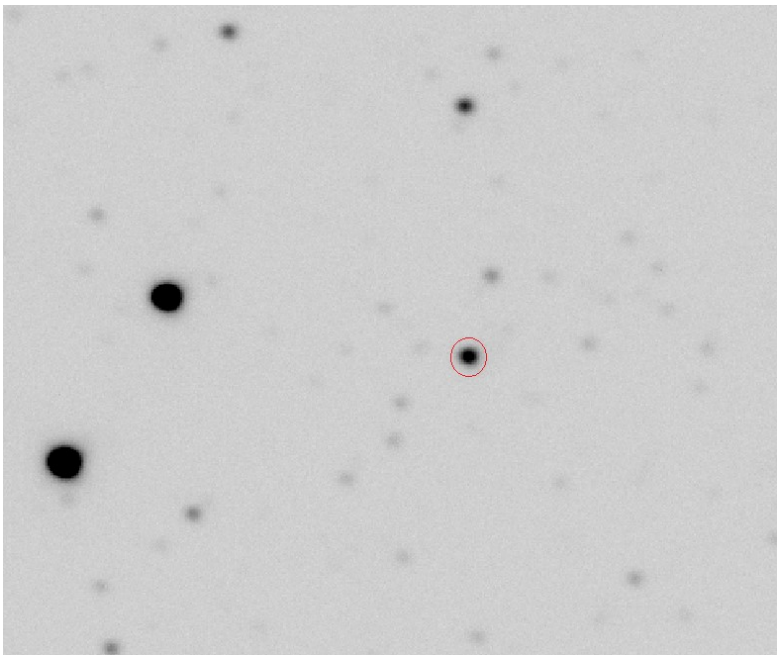

out05030

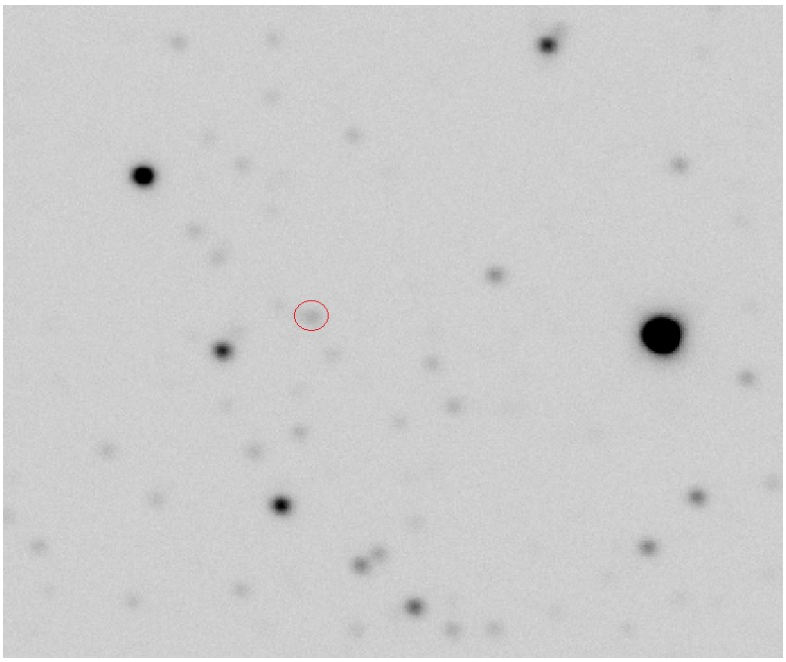

out04749

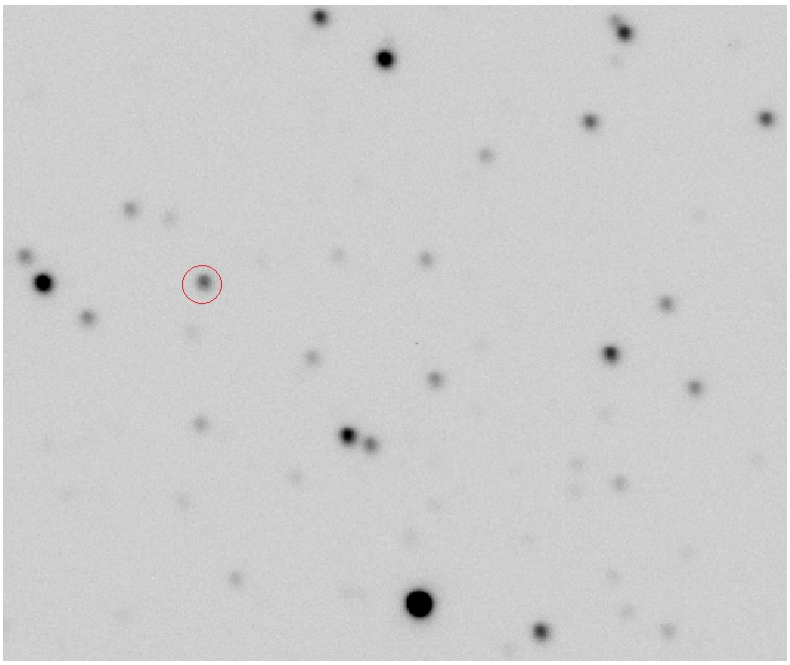

out04706

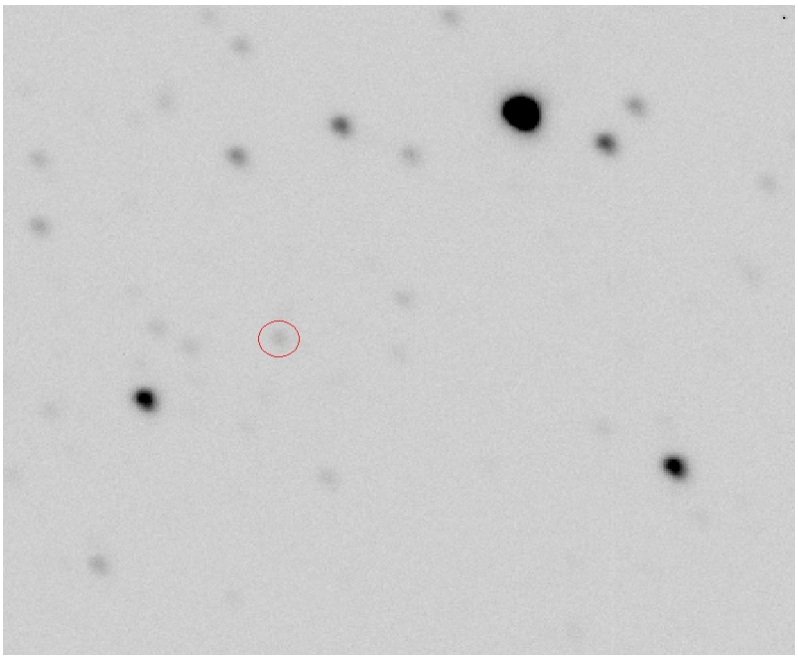

out04692

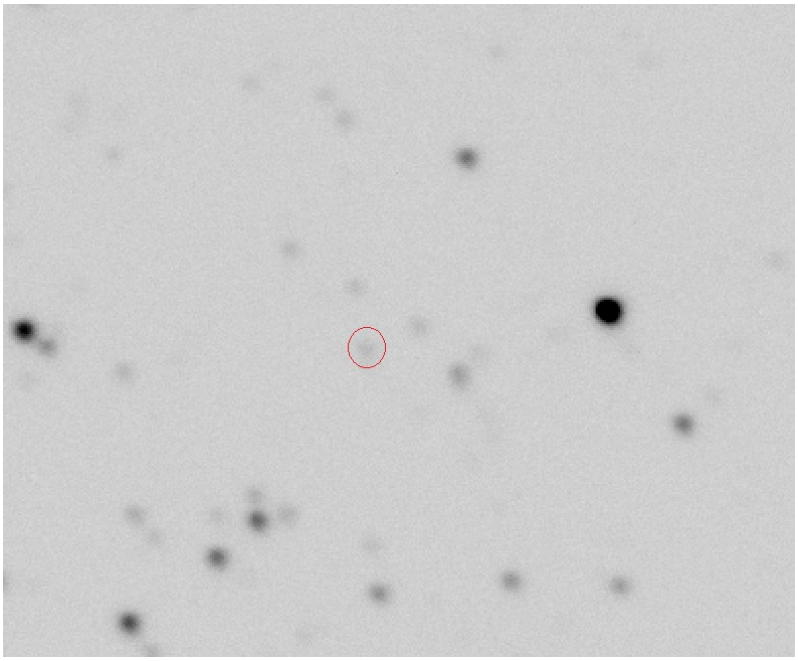

out04273

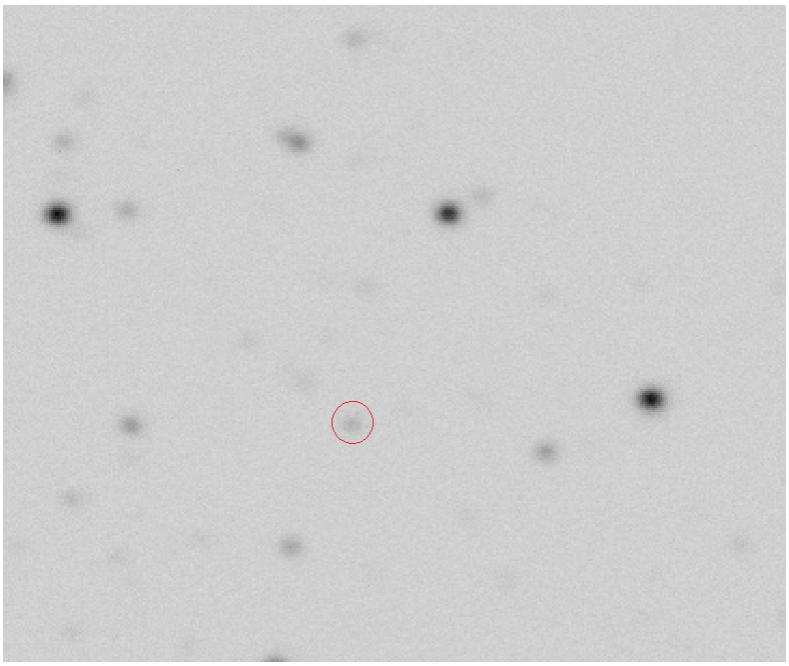

out04255

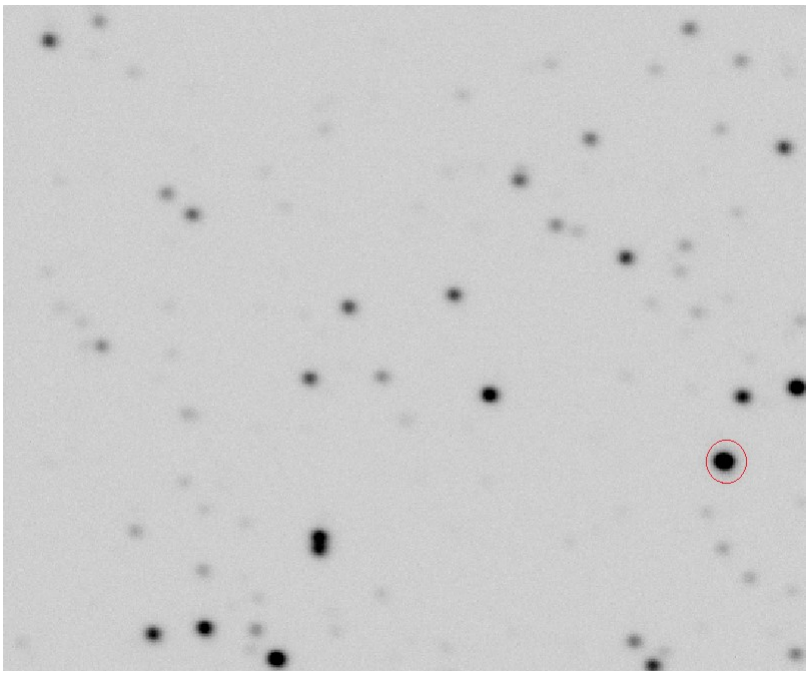

out04182

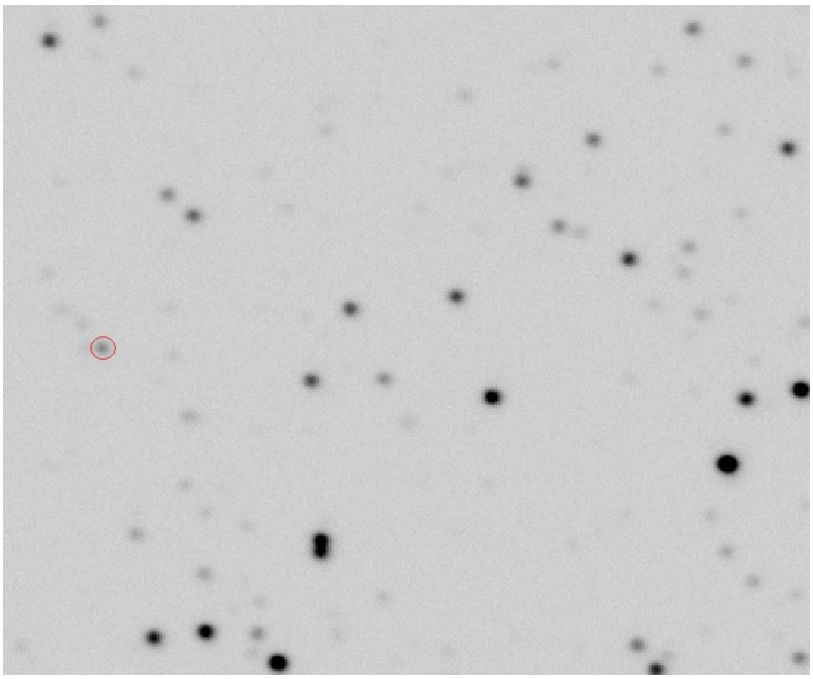

out04181

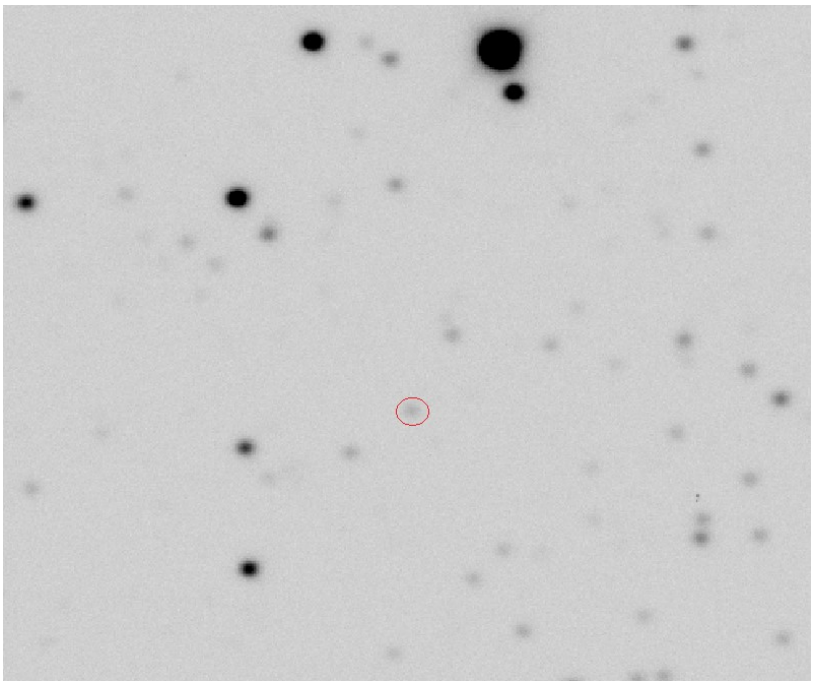

out04128

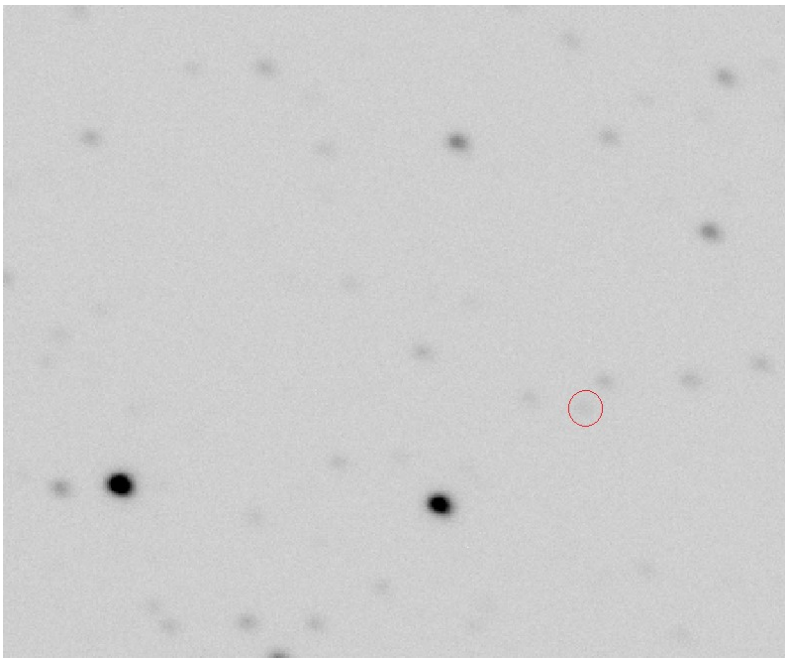

out04066

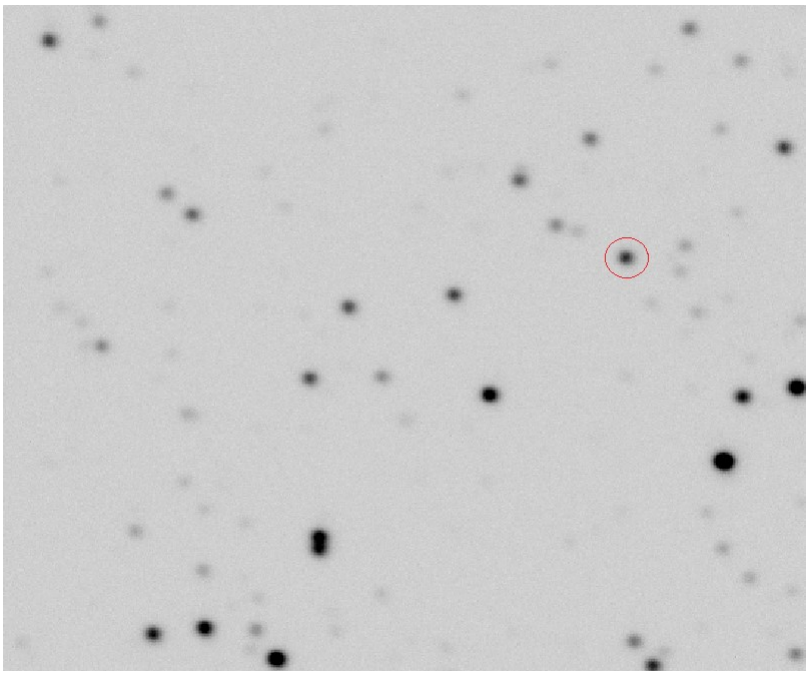

out03651

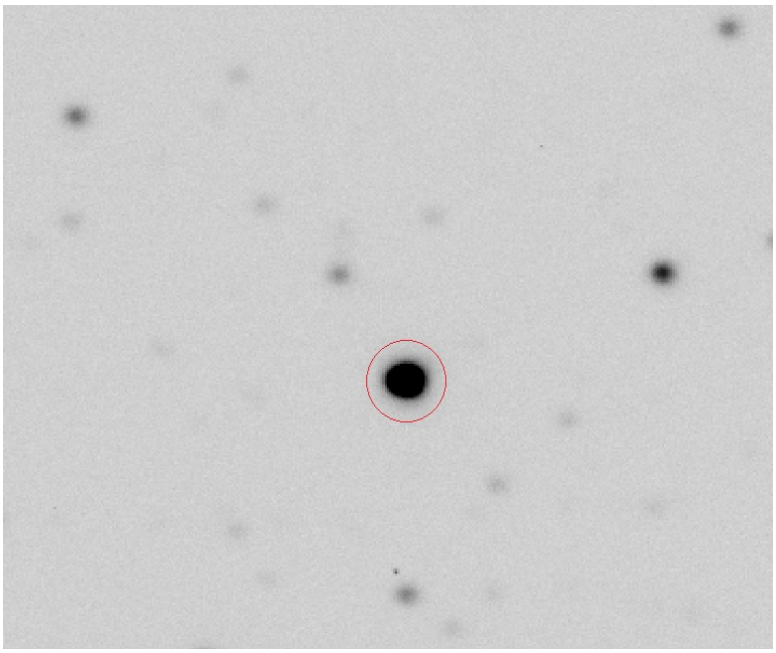

out03433

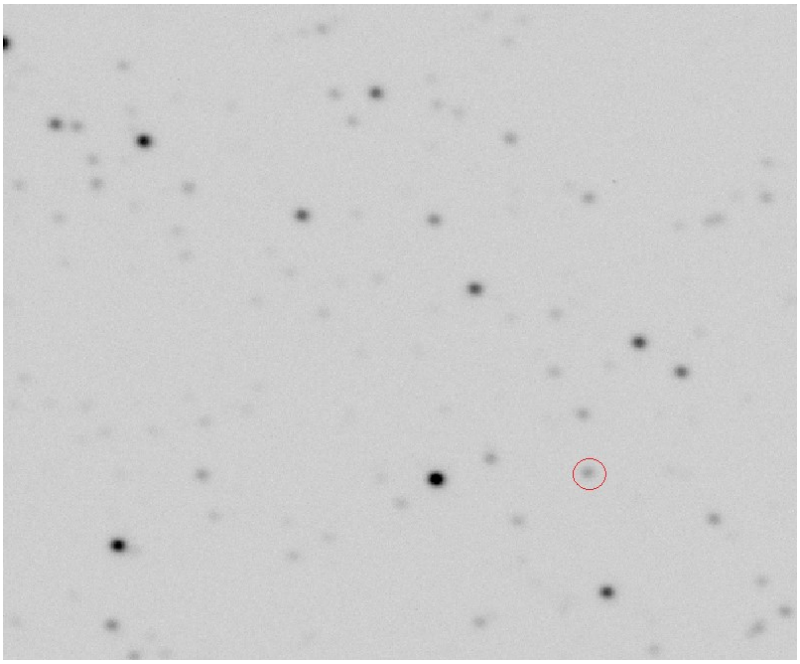

out03365

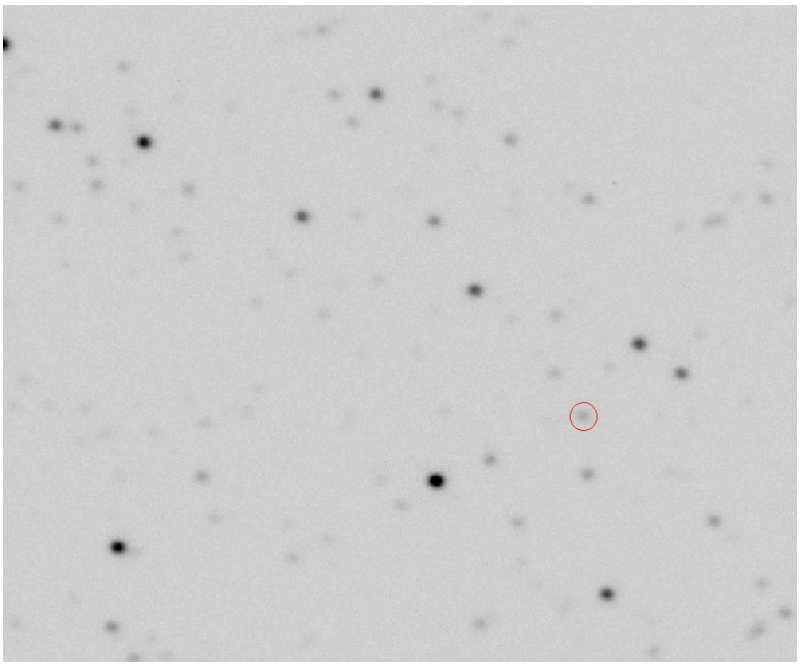

out03342

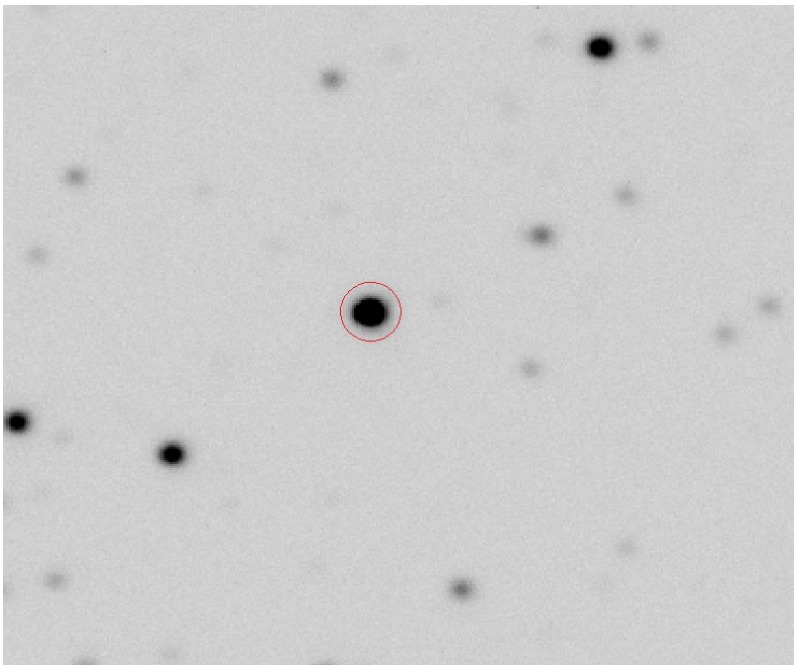

out03277

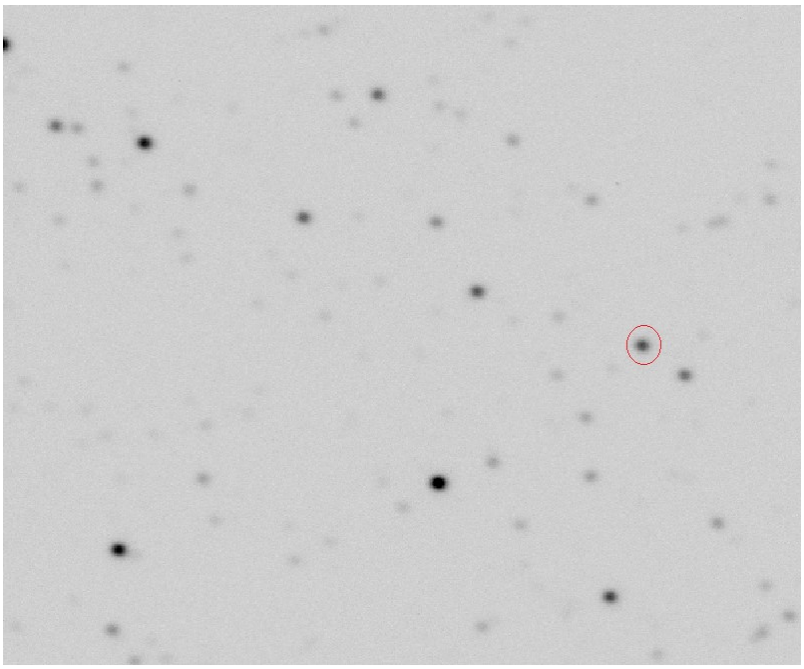

Southern Variables

out00223

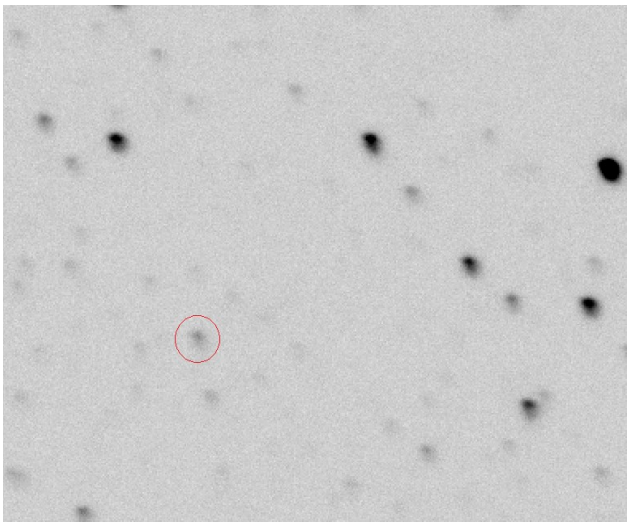

out00282

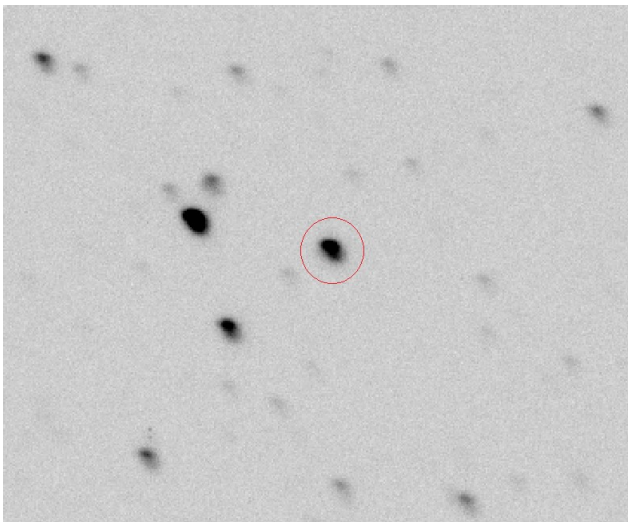

out00419

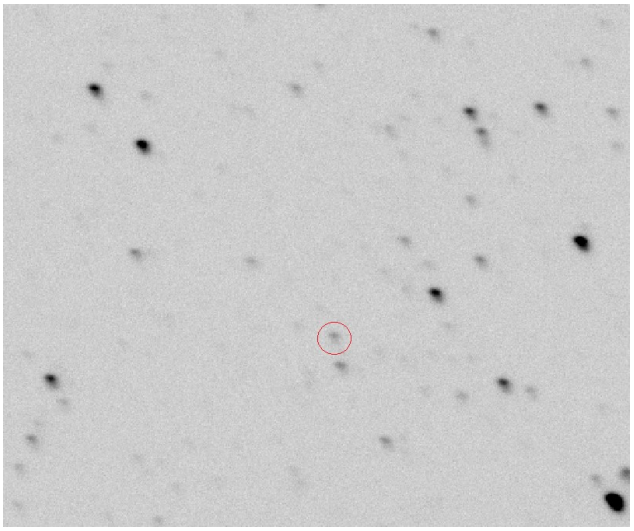

out00628

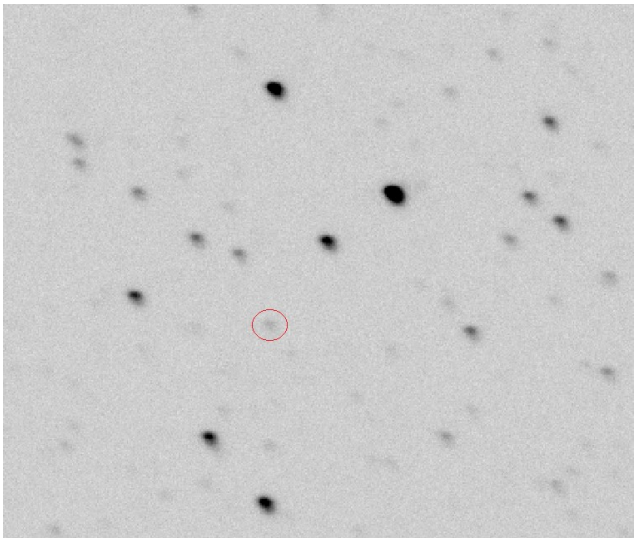

out01013

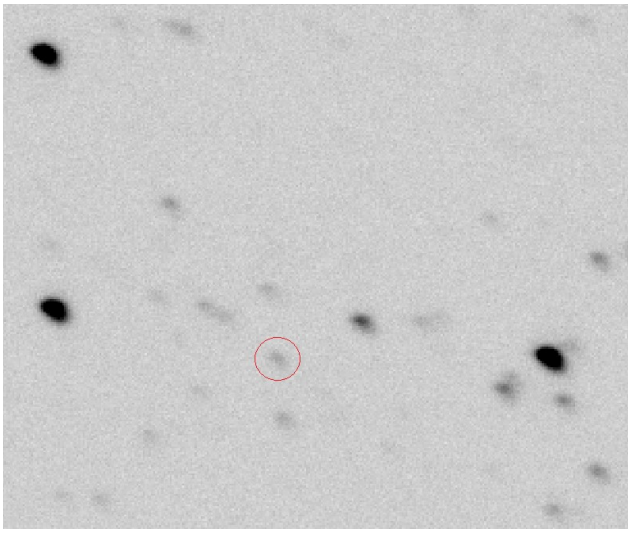

out01666

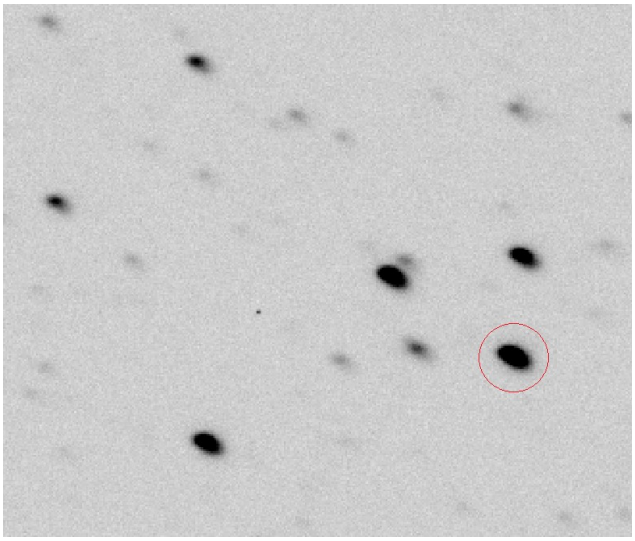

out01706

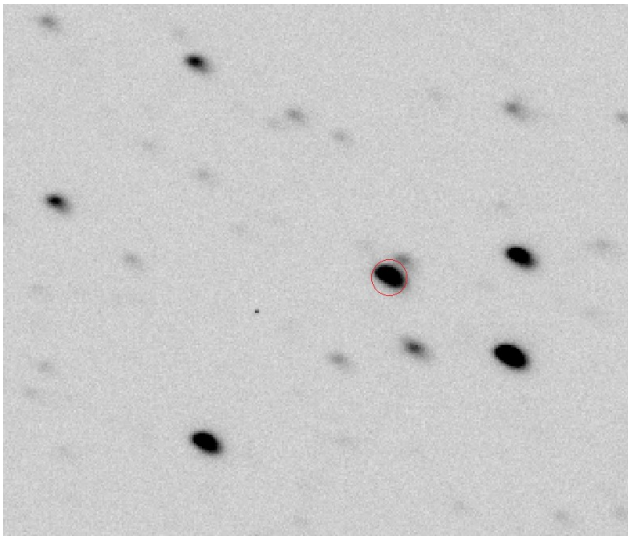

out02175

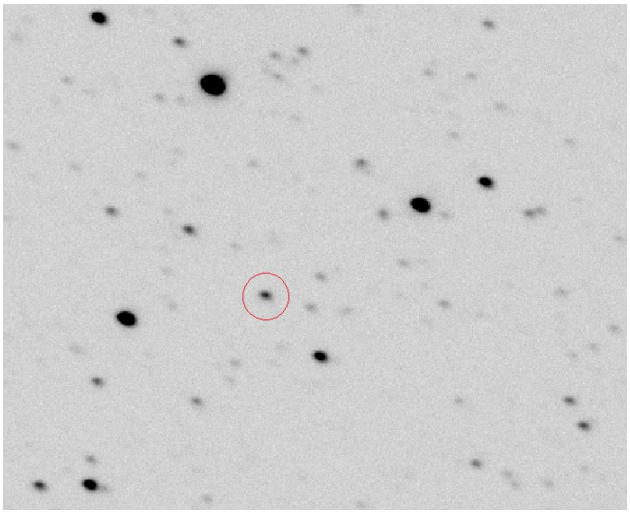

out02399

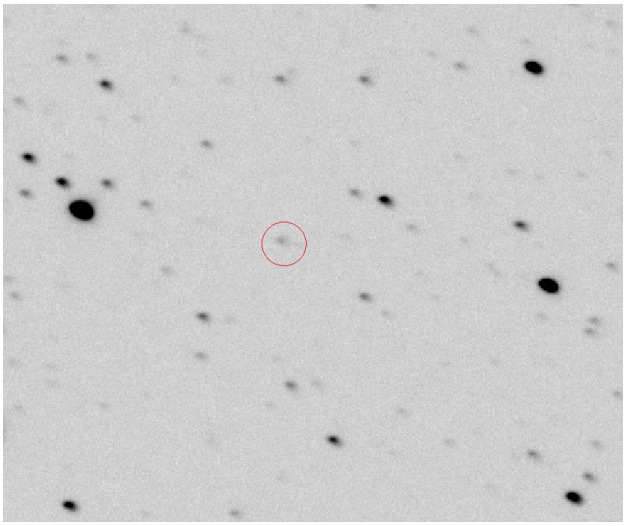

out02668

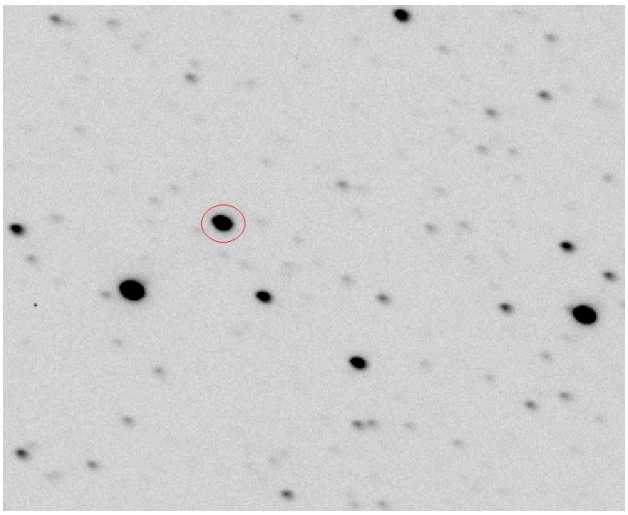

out02873

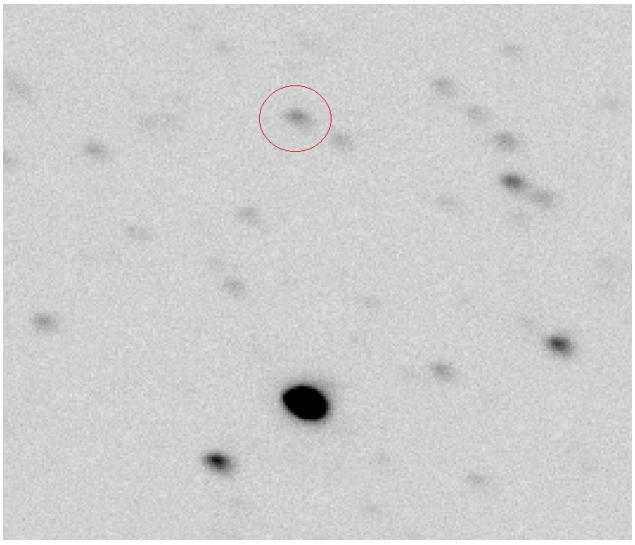

out03077

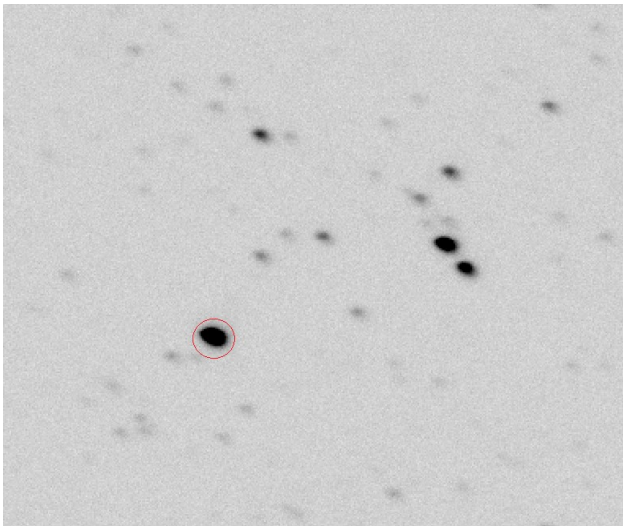

out20167

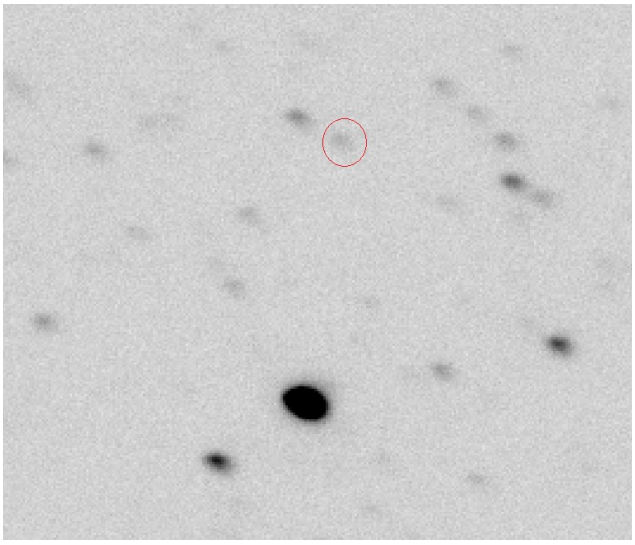

out20496